Doctoral Thesis

Hybrid Orientation of LiDAR Point Clouds and Aerial Images

submitted in satisfaction of the requirements for the degree of
"Doktor der Technischen Wissenschaften (Dr. techn.)"
of the TU Wien,
Department of Geodesy and Geoinformation,
Research Group Photogrammetry

Dissertation

Hybride Orientierung von Laserscanning-Punktwolken und Luftbildern

ausgeführt zum Zwecke der Erlangung des akademischen Grades eines
Doktor der Technischen Wissenschaften (Dr. techn.)
eingereicht an der Technischen Universität Wien,
Department für Geodäsie und Geoinformation,
Forschungsgruppe Photogrammetrie

von

Dipl.-Ing. **Philipp Glira**

Leitung:	Univ.Prof. Dipl.-Ing. Dr.techn. **Norbert Pfeifer** Department für Geodäsie und Geoinformation Technische Universität Wien
Gutachter:	apl. Prof. Dr.-Ing. **Norbert Haala** Institut für Photogrammetrie Universität Stuttgart
Gutachter:	apl. Prof. Dr. techn. **Franz Rottensteiner** Institit für Photogrammetrie und GeoInformation Leibniz Universität Hannover

Wien, im Dezember 2018

Author's Statement / Erklärung zur Verfassung der Arbeit

I hereby declare, that I independently drafted this manuscript, that all sources and references used are correctly cited and that the respective parts of this manuscript including tables, maps and figures – which were included from other manuscripts or the internet, either semantically or syntactically –, are made clearly evident in the text and all respective sources are correctly cited.

Hiermit erkläre ich, dass ich diese Arbeit selbstständig verfasst habe, dass ich die verwendeten Quellen und Hilfsmittel vollständig angegeben habe und dass ich die Stellen der Arbeit – einschließlich Tabellen, Karten und Abbildungen –, die anderen Werken oder dem Internet im Wortlaut oder dem Sinn nach entnommen sind, auf jeden Fall unter Angabe der Quelle als Entlehnung kenntlich gemacht habe.

Philipp Glira

Bauernfeldgasse 3/5
2230 Gänserndorf
Österreich

Abstract

Airborne LiDAR (Light Detection And Ranging) and airborne photogrammetry are both proven and widely used techniques for the 3D topographic mapping of extended areas. Although both techniques are based on different reconstruction principles (polar measurement vs. ray triangulation), they ultimately serve the same purpose, the 3D reconstruction of the Earth's surface. It is therefore obvious for many applications to integrate the data from both techniques to generate more accurate and complete results. Many works have been published on this topic of data fusion. However, no integrated solution existed prior to this work for the first steps that need to be carried out after data acquisition, namely (a) the lidar strip adjustment and (b) the aerial triangulation. A consequence of solving these two optimization problems independently can be large discrepancies (of up to several decimeters) between the lidar block and the image block. This is especially the case in challenging situations, e.g. corridor mapping with one strip only or in case few or no ground truth data is available. To avoid this problem and thereby profit from many other advantages, a first rigorous integration of these two tasks, the *hybrid orientation of lidar point clouds and aerial images*, is presented in this thesis.

The main purpose of the presented method is to simultaneously optimize the relative orientation and absolute orientation (georeference) of the lidar and image data. This data can be used afterwards to generate accurate and consistent 3D or 2D mapping products. The orientation of the lidar and image data is optimized by minimizing the discrepancies (a) within the overlap area of this data and (b) with respect to ground truth data, if available. The measurement process is thereby rigorously modelled using the original measurements of the sensors (e.g. the polar measurements of the scanner) and the flight trajectory of the aircraft. This way, systematic measurement errors can be corrected where they originally occur. Both, lidar scanners and cameras, can be fully re-calibrated by estimating their interior calibration and mounting calibration. Systematic measurement errors of the flight trajectory can be corrected individually for each flight strip. For highest accuracy demands, time-dependent errors can be modelled by natural cubic splines.

The methodological framework of the hybrid adjustment was adapted from the ICP algorithm. Consequently, correspondences are established iteratively and on a point basis to maintain the highest possible resolution level of the data. Four different strategies are presented for the selection of correspondences within the overlap area of point clouds. Thereby, the *Maximum Leverage Sampling* strategy is newly introduced. It automatically selects those correspondences that are best suited for the estimation of the transformation parameters.

The various aspects of the hybrid adjustment are discussed on the basis of four examples. It is demonstrated, that the integration of the lidar strip adjustment and aerial triangulation leads to many synergetic effects. Two of the major advantages are an increased block stability (avoiding block deformations, e.g. bending) and an improved determinability of the parameters.

Kurzfassung

Airborne Laserscanning (auch LiDAR, Light Detection And Ranging) und Luftbildphotogrammetrie sind zwei bewährte und weit verbreitete Technologien um dreidimensionale topographische Daten zu erfassen. Obwohl beide Technologien auf unterschiedlichen Rekonstruktionsprizipien basieren (Polarmessung bzw. Triangulierung von Sehstrahlen), dienen beide im Endeffekt dem gleichen Zweck, der dreidimensionalen Rekonstruktion der Erdoberfläche. Es ist daher naheliegend die Daten dieser beiden Technologien zu kombinieren um genauere und vollständigere Endprodukte zu erzeugen. Zu diesem Thema der Datenfusion wurden in der Vergangenheit bereits viele Arbeiten publiziert. Dies gilt jedoch nicht für eine integrierte Lösung der ersten beiden Schritte die unmittelbar nach der Datenerfassung durchzuführen sind, nämlich (a) die Streifenausgleichung der Laserscanning-Daten und (b) die Aerotriangulation der Luftbilder. Eine mögliche Folge der getrennten Handhabung dieser beiden Probleme sind große Abweichungen (von bis zu mehreren Dezimetern) zwischen dem ausgeglichenen Laser- und Bildblock. Diese Gefahr besteht vor allem in verhältnismäßig schwierigen Situationen wie z.B. Korridorflügen mit nur einem Streifen oder falls wenige oder gar keine Bodenreferenzdaten zur Verfügung stehen. Um derartige Probleme zu vermeiden, und dabei noch von vielen anderen Vorteilen zu profitieren, wurden diese beiden Schritte in der vorliegenden Arbeit in einer gemeinsamen hybriden Orientierung von Laserscanning-Punktwolken und Luftbildern zusammengeführt.

Das vordergründige Ziel der vorgestellten Methode ist die gleichzeitige relative und absolute Orientierung (Georeferenzierung) der Laser- und Bilddaten. Diese Daten können in der Folge für die Erstellung von sehr genauen und in sich konsistenten zwei- oder dreidimensionalen topographischen Produkten verwendet werden. Die Orientierungen der Laserscanning-Daten und Luftbilder wird durch die Minimierung der Abstände (a) innerhalb der Überlappungsbereiche der Daten und (b) gegenüber etwaig vorhandenen Bodenreferenzdaten optimiert. Der Messprozess wird dabei möglichst akkurat modelliert indem die Originalmessungen der Sensoren (z.B. die Polarmessungen des Scanners) und die Trajektorie der Flugplattform berücksichtigt werden. Sowohl Laserscanner, als auch die Kameras, können durch die Schätzung interner Kalibriergrößen und der Montageparameter vollständig neu kalibriert werden. Systematische Fehler der Flugtrajektorie können individuell für jeden einzelnen Streifen korrigiert werden. Bei sehr hohen Genauigkeitsansprüchen können sogar zeitvariierende Trajektorienfehler durch deren Modellierung in Form von natürlichen kubischen Splines kompensiert werden.

Das methodische Rahmenwerk für die hybride Ausgleichung wurde vom ICP-Algorithmus übernommen. Daher werden Korrespondenzen iterativ und auf Punktbasis hergestellt. Letzteres ermöglicht die Nutzung der höchstmöglichen Auflösung der Daten. Für die Selektion der Korrespondenzen in den Überlappungsbereichen der Punktwolken, stehen vier Strategien zur Auswahl. Neu eingeführt wurde dabei die *Maximum Leverage Sampling* Methode. Mit dieser können automatisch jene Korrespondenzen gewählt werden, die sich für die Schätzung der Transformationspa-

rameter am besten eignen.

Die verschiedenen Aspekte der hybriden Ausgleichung werden in vier Beispielen beleuchtet. Dabei wird gezeigt, dass die Integration der Streifenausgleichung und Aerotriangulation zu vielen Synergien führt. Hervorzuheben sind dabei eine erhöhte Blockstabilität (wobei Blockdeformation, z.B. eine Durchbiegung, besser vermieden werden können) und eine genauere Schätzung der Parameter.

Contents

1 Introduction

1.1 Motivation

Airborne LiDAR (Light Detection And Ranging), also referred to as Airborne Laser Scanning (ALS), and airborne photogrammetry are both proven and widely used techniques for the 3D topographic mapping of extended areas. Although both techniques are based on different principles (polar measurement vs. ray triangulation), they ultimately serve the same purpose, the 3D reconstruction of the Earth's surface. It is therefore obvious for many applications to integrate both techniques to generate more accurate and complete results (Baltsavias, 1999). Thus, many works have been published on the integration of lidar and photogrammetry, e.g. for the generation of true orthophotos (Habib, 2018) or the modeling of buildings (Brenner, 2005). However, this is not the case for the first steps that need to be carried out after data acquisition, namely the calibration and orientation of the sensors and their data. These are (a) the strip adjustment of lidar point clouds and (b) the triangulation of aerial images. This work aims to provide a first rigorous integration of these two tasks, the *hybrid adjustment of lidar point clouds and aerial images*. Thereby the orientation of lidar point clouds and aerial images is simultaneously optimized. This is achieved by correcting the aircraft's flight trajectory (which is shared by the lidar point clouds and aerial images), by fully re-calibrating the lidar scanner(s) and camera(s), and by considering ground truth data if available, e.g. ground control points, cf. Figure 1.1.

Up to approximately 15 years ago, image-based methods were predominately used for 3D topographic modeling. This rapidly changed with the advent of the lidar technology, mainly due to its ability to penetrate vegetation through small gaps in the foliage and thereby measure the underlying ground. However, over the last 10 years, advanced Dense Image Matching (DIM) methods have been developed (Hirschmuller (2008), Rothermel et al. (2012), Remondino et al. (2014)), which can generate automatically dense and colorized 3D point clouds from overlapping images. A comparison between lidar and DIM point cloud is shown in Figure 1.2. In Mandlburger et al. (2017) a comprehensive description of the main characteristics of lidar and DIM point clouds is given. The two main advantages of DIM point clouds in comparison to lidar point clouds are (a) the typically higher point density, as a 3D point can be reconstructed for each image pixel, and (b) the color information for each point. On the other side, lidar point clouds are typically more accurate, especially in vegetated areas, at edges (e.g. of buildings), in case of occlusions and other areas of abrupt changes. In the past often either a lidar scanner *or* an aerial camera was used on an airborne platform for topographic modeling. The trend now goes clearly towards multi-sensor systems, i.e. the integration of laser scanner(s) *and* aerial camera(s) on a single sensor platform. Even on UAVs, despite the limited payload, the integration becomes increasingly common, mainly due to the miniaturization of the sensors. Such multi-sensor systems enable the fusion of lidar and

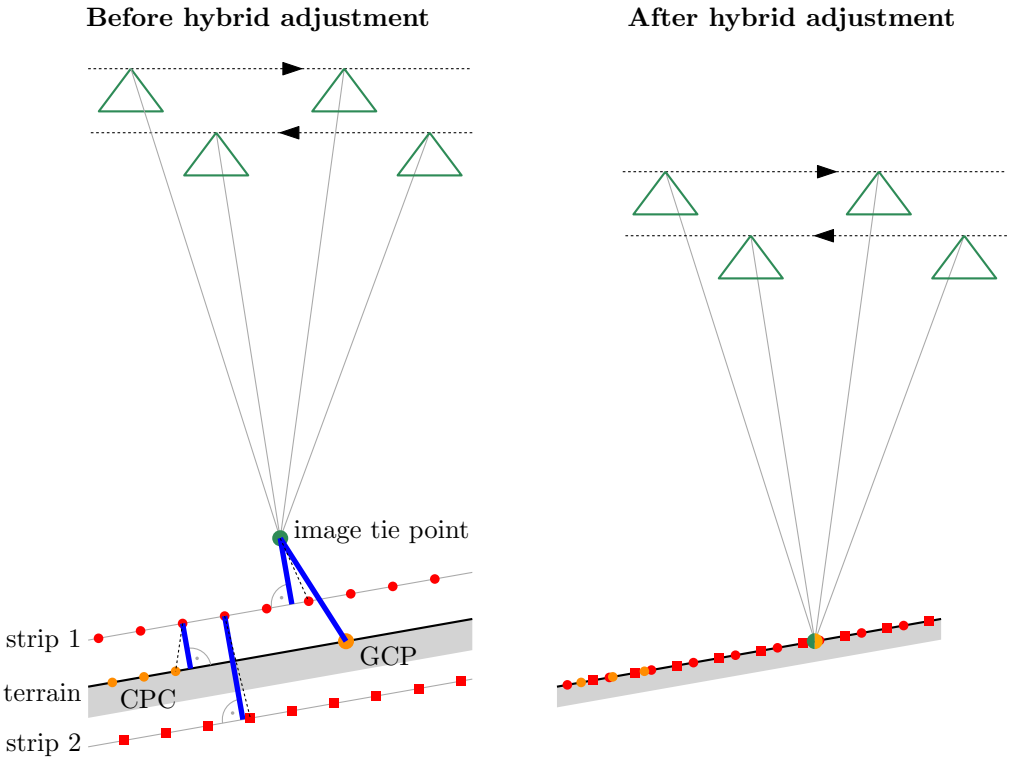

Figure 1.1: The aim of the hybrid adjustment is to simultaneously optimize the orientation of lidar point clouds and aerial images considering ground-truth-data, e.g. control point clouds (CPCs) or ground control points (GCPs). This is achieved by correcting the aircraft's flight trajectory and by fully re-calibrating the laser scanner(s) and camera(s). The minimized distances are shown in blue.

image-based data, e.g. lidar and DIM point clouds, whereby the advantages of both technologies can be exploited to generate optimized products (Mandlburger et al., 2017). However, a basic prerequisite for the fusion of lidar and image-based data is an accurate relative and absolute orientation (*georeference*). This can be achieved through the hybrid adjustment presented in this thesis.

A comparison between airborne lidar and airborne photogrammetry is given in Table 1.1. Lidar is an active polar measurement system. The range is thereby measured by the time-of-flight principle: a laser pulse is emitted and scattered on one or more objects along its path producing echoes which are then registered by the scanner's detector. Consequently, a single sight is sufficient to determine the 3D coordinates of an object point. The main components of a lidar system are a laser scanner and a GNSS/INS navigation system. The GNSS and INS measurements are integrated with a Kalman filter (Kalman, 1960) or a variant thereof to produce an accurate estimate of the platform's trajectory, i.e. its position (three coordinates: x, y, z) and orientation (three angles: roll, pitch, yaw) as a function of time. The so-obtained trajectory is combined with the mounting calibration parameters (which describe the positional and rotational offsets between the scanner and the GNSS/INS system) to determine the orientation of the laser scanner (*direct*

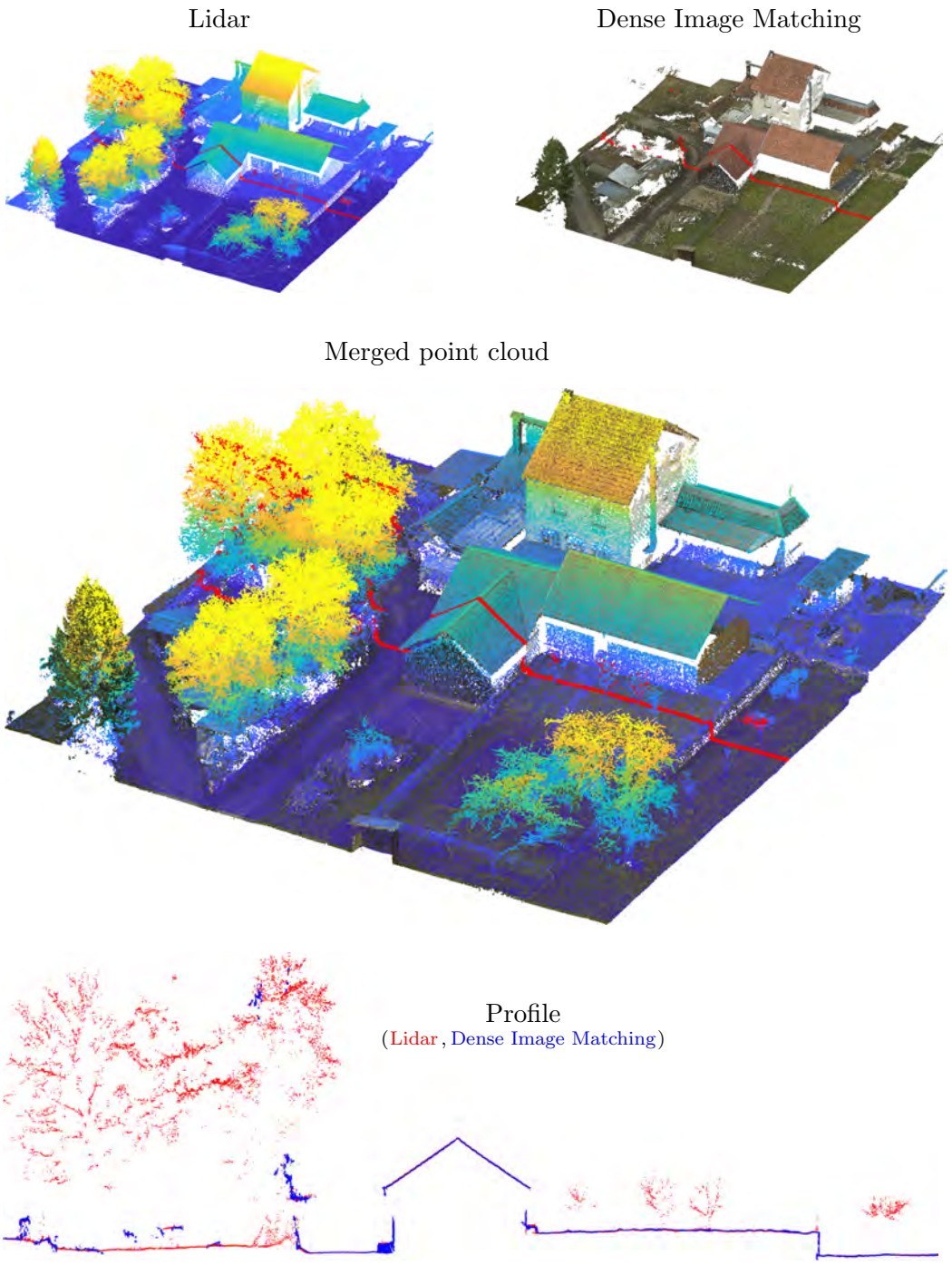

Figure 1.2: Top: Lidar (z-colored) and Dense Image Matching (rgb-colored) point clouds. Middle: Merged point clouds. Botton: Profile through merged point clouds. These point clouds are taken from the example in section 4.4.

		Airborne lidar	Airborne photogrammetry
data acquisition	• sensors	scanner(s) + GNSS/INS	camera(s) (+ optional GNSS/INS)
	• light source	active (laser)	passive (solar radiation)
	• measurement principle	time-of-flight	capturing of visible light
	• measurement rays per point	1 (polar system)	≥ 2 (multi-view stereo)
	• radiometry	mono-spectral (laser-wavelength)	multi-spectral (R-G-B)
	• preconditions	(diffuse) object reflectance	texture (image contrast)
	• geodata recording	continuous	at exposure times of images
	• in-strip redundancy	no	yes
adjustment	• method	strip adjustment of lidar strips	aerial triangulation of aerial images
	• typical ground-truth-data	surfaces	points (GCPs)
	• estimated parameters	scanner calibration mounting calibration trajectory correction	interior orientation (mounting calibration) trajectory correction
	• typical correspondences	homologous planes	homologous points

Table 1.1: Comparison between airborne lidar and photogrammetric triangulation (adapted partly from Mandlburger et al. (2017)).

sensor orientation). Finally, the polar measurements of the laser scanner (range and angle(s)) are added to the orientation of the laser scanner to obtain the final product, the georeferenced 3D point cloud (*direct georeferencing*). Generally, the so-generated point clouds contain systematic georeferencing errors. These errors can be recognized as discrepancies between overlapping strips and as discrepancies between strips and ground-truth data, e.g. ground control points (GCPs) or reference planes. Experience shows that the major parts of these discrepancies stem from the GNSS/INS navigation system and the rotational part of the mounting calibration (*boresight misalignment*). To re-calibrate the entire lidar system and correct the trajectory errors, strip adjustment (also known as *integrated sensor orientation*) can be performed. This is done by refining the point cloud generation process *after* the trajectory estimation by additional (calibration and correction) parameters. These parameters are estimated by exploiting the redundancy contained in the overlapping areas of the strips and by considering the ground-truth data. The estimated parameters can be divided into three categories: (a) the scanner calibration parameters (e.g. range finder offset), (b) the mounting calibration parameters (lever-arm and misalignment), and (c) the trajectory correction parameters.

In aerial photogrammetry the 3D reconstruction is based on the spatial intersec-

tion of rays. Consequently, the reconstruction of a single object point needs at least two intersecting rays, i.e. two aerial images taken from different positions showing the same object point. Consequently, the triangulation of ground points through dense vegetation is very unlikely. A single ray is thereby defined by the exterior orientation of an image (three coordinates, three angles describing its position and rotation) and the interior orientation of a camera (principal distance, principal point, distortion parameters). In contrast to a lidar system, a GNSS/INS navigation system is not strictly mandatory, but highly recommended for the direct measurement of the six elements of the exterior orientation. However, especially if imagery is captured from UAVs, often only the onboard low-cost GNSS/INS systems are available, giving relatively inaccurate estimates of the aircraft's trajectory (Colomina (2015), Cucci et al. (2017)). An aerial triangulation (bundle block adjustment of aerial images) has much in common with the strip adjustment of lidar strip described above. The parameters of the exterior and interior orientation of the aerial images are estimated by exploiting the redundancy contained in the image overlap and by considering ground-truth-data, e.g. ground control points. If a GNSS/INS trajectory is given, the similarities get even more obvious. The parameter of the exterior orientation can then be obtained by combining the flight trajectory and the mounting calibration of the cameras (*direct sensor orientation* or *direct georeferencing*). In this (standard) case, the parameters estimated in the aerial triangulation can be divided into the same three categories: (a) the parameters of the interior orientation (camera calibration parameters), (b) the mounting calibration parameters (lever-arm and misalignment), and (c) the trajectory correction parameters.

Despite all these similarities, strip adjustment of lidar point clouds and aerial triangulation of aerial images are carried out independently in practice. Both optimization problems on their own have been thoroughly studied over the last decades and sophisticated methods exist for the lidar strip adjustment (Toth and Koppanyi, 2018) and the aerial triangulation (Förstner and Wrobel (2016), Kraus (1997)). It is important to stress that the separation of these two orientation problems is not a problem per se. If proven flight configurations with longitudinal and cross strips are used and sufficient ground-truth-data is available, a very accurate relative and absolute orientation of lidar and image block can be achieved. However, many situations exist, where an isolated orientation of lidar and images is very challenging, e.g. corridor mapping with one lidar or image strip only, areas with unfavorable distribution of homologous image points, large non-textured areas, structureless areas, dynamic areas (e.g. water), in case of low lidar strip and/or image overlap, or if insufficient ground-truth-data is available. Many problems can arise in such situations, stemming primarily from a low redundancy and weak geometrical constraints. One of the best-known problems is – despite the direct observation of the flight trajectory by GNSS/INS – an inaccurate absolute orientation of the entire lidar/image block (e.g. bending), mostly due to the accumulation of non-modeled systematic measurement errors. We show that the integration of lidar, image, and GNSS/INS observations into a common adjustment can mitigate such problems, as both data types benefit from each other. This benefit stems primarily from the incorporation of additional geometric constraints. One example is the correction of the aircraft's trajectory: to minimize the discrepancies between overlapping lidar point clouds, a very flexible correction model is needed for the GNSS/INS trajectory (we will propose a correction model based on cubic splines for this, cf. section

3.1.4.1). However, the flexibility of such a model involves many risks. In case of wrong stochastic modeling (weighting), or in case overfitting occurs, the whole lidar block may get deformed. We show, that when lidar and images are combined, this problem is strongly mitigated, as the lidar measurements are subject to geometric constraints formulated through the image measurements and vice versa. Thus, the symbiotic relationship between these two techniques enhances each other to provide a better solution.

1.2 Contributions

In this thesis a new method for the rigorous integration of (a) the strip adjustment of lidar strips and (b) the triangulation of aerial images into a single hybrid adjustment is presented. However, the hybrid adjustment marks only the end of a long journey, in which practical solutions have been found for many subproblems. These solutions might be useful also in a different context. Therefore, the three main contributions can be summarized as follows:

1. **Correspondence framework** We present a framework, inspired by the well-known ICP algorithm, for the selection of correspondences within the overlap area of point clouds. Thereby, correspondences are established iteratively and on a point basis. Four different strategies are presented for the selection of correspondences: *Random Sampling*, *Uniform Sampling*, *Normal Space Sampling*, and *Maximum Leverage Sampling*. The latter is based on the theory of least squares adjustment and selects correspondences automatically in areas that are best suited for the estimation of transformation parameters.

2. **Comprehensive parameter model** A comprehensive parameter model is presented for the adjustment of lidar strips and aerial cameras. This includes parameters for the calibration of these sensors, parameters for the orientation of their data, and four different parameter models for the correction of the flight trajectory: *Bias Trajectory Correction model*, *Linear Trajectory Correction model*, *Quadratic Trajectory Correction model*, and *Spline Trajectory Correction model*. With the latter, strong varying time-dependent systematic trajectory errors can be corrected significantly.

3. **Integration of lidar strip adjustment and aerial triangulation of aerial images** We show that joint processing of lidar and image data offers many advantages, especially for high accuracy applications and other challenging situations, e.g. corridor mapping. The main advantages are:

   a) **Inherent optimization of the relative orientation between lidar point clouds and images** The discrepancies between the lidar point clouds and the image tie points are inherently minimized in the hybrid adjustment. This leads to an optimal relative orientation between the lidar block and the image block. This can be of great advantage if products are derived from both data types, e.g. a merged lidar/DIM point cloud or true orthophotos.

   b) **More precise and reliable parameter estimation due to higher redundancy** As both, lidar and images, jointly observe the Earth's surface, a higher redundancy for the parameter estimation is given. This, in

turn, improves the a posteriori precision of the estimated parameters and increases the potential to identify gross errors in the observation data.

c) **More reliable absolute orientation of lidar and image block** We show that due to the integration of lidar and image observations in a single adjustment, block deformations become more unlikely. The main reason for this is the incorporation of additional geometric constraints that lead to an increased overall block stability.

d) **Need of fewer ground-truth-data (points or surfaces)** Ground-truth-data can be introduced into the adjustment in two forms: as control point clouds (CPCs) and as ground control points (GCPs). As both of these types can be used to define the datum of the lidar and image block simultaneously, fewer ground-truth-data is needed in total. For instance, in the presence of CPCs no GCPs need to be measured, as the CPCs are solely defining the datum of the lidar *and* the image data.

1.3 Related work

Literature on the integration of lidar and photogrammetry A general comparison between photogrammetry and lidar is given in Baltsavias (1999). Despite the age of this paper, most of the discussed aspects are still relevant. The author stresses that the two techniques are fairly complimentary and their integration can lead to more accurate and complete final products. On the topic of lidar strip adjustment, the lack of standards or commonly accepted guidelines on how to perform calibration is criticized, a point which is still valid today. In Ressl et al. (2016) a comparison between lidar and DIM point clouds is presented, especially concerning the capability of retrieving terrain data. It is also shown that one must be very cautious when matching lidar and image data in object space, as the height of the lidar point cloud can be systematically lower with respect to the triangulated image points due to the capability of the laser to penetrate objects through small openings, e.g. in case of low vegetation.

Many publications prove the potential of an integrated processing of lidar and image data for the derivation of final products, e.g. Habib (2018) demonstrates the advantages of an integrated approach for the generation of true orthophotos, Brenner (2005) combine lidar and image data for the modeling of buildings, Beger et al. (2011) combine lidar and high-resolution image data for the automatic railroad centerline reconstruction, Bork and Su (2007) integrate lidar data and multi-spectral images to improve the classification of rangeland vegetation, and Mandlburger et al. (2017) use lidar and image data for point cloud fusion and digital surface model derivation.

Literature on co-registration of lidar point cloud and images Many papers have also been published on the topic of co-registration of lidar and image data. However, none of these works addresses the rigorous integration – i.e. considering the flight trajectory, the mounting calibration parameters, and sensor calibration parameters – of lidar strip adjustment and aerial triangulation. Instead, most studies start from an adjusted lidar block and provide solutions to optimize the co-registration of the images only. Yang and Chen (2015) present a multi-step approach to minimize sig-

nificant discrepancies between aerial images and lidar data. The method is based on the matching of building outlines and therefore limited to urban areas. In contrast to our approach, no rigorous modeling of the measurement process is conducted. Instead, the lidar and image block are matched applying a rigid body transformation only, leading to a comparatively moderate georeference accuracy. Similarly, Abayowa et al. (2015) present a framework for the registration of lidar and image data. Thereby, the ICP algorithm is used to minimize the discrepancies between two DSMs, one derived from the lidar point cloud, the other derived from a DIM point cloud. The main contribution is the ability to find an initial relative orientation between the lidar and image block by matching salient, invariant features derived from the two DSMs. However, in aerial lidar and aerial photogrammetry, an approximative relative orientation is generally known due to the usage of GNSS/INS. In Parmehr et al. (2014) an approach for the registration of lidar and image data based on mutual information is presented. Thereby, the matching between lidar and image data does not rely on the presence of physical correspondences (e.g. edges, corner), but exploits the statistical dependencies between the two datasets, e.g. between the aerial images, the lidar point cloud, and the lidar intensity data.

Literature on lidar strip adjustment A rigorous error analysis of kinematic scanning systems is presented in Glennie (2007). This includes a discussion of the magnitudes of the major error sources and their effect on the horizontal and vertical precision of the ground points. The publication demonstrates how difficult it is to find reliable error estimates, since they are either based on the manufacturer's technical specifications, on a previously performed least squares adjustment, or on relatively arbitrary empirical values. The overall precision of the ground points, as well as the contribution of the single error sources, are examined for three different measurement scenarios. It is demonstrated that for a fixed-wing aircraft at high altitudes ($> 500\,\mathrm{m}$), the horizontal precision of the ground points is at least three times worse than the vertical precision. More specifically, the horizontal precision primarily depends (60% to 75%) on the precision of the rotation measurements, i.e. the INS and misalignment values, whereas the influence of these measurements on the vertical precision is decisively smaller (25% to 50%). The error model presented in this publication was validated with ground truth data. Possible sources for random and systematic errors and their effect on ground points are also discussed extensively in Habib and Rens (2007). Additionally, a review of the existing strip adjustment methods at that time is given.

In Skaloud et al. (2010) a method for the *real-time* registration of lidar data is presented. This includes not only the direct georeferencing of the data, but also a slightly time-delayed estimation of the precision of each point. In a mathematically rigorous way, the direct georeferencing process considers the random errors of all involved measurements: the time-dependent precisions of the position and rotation measurements are obtained from a loosely-coupled Extended Kalman Filter (EKF), the lever-arm and misalignment precisions come from a previous calibration, and the manufacturer provides the scanner precisions. As the final point precision is also affected by the incidence angle, the terrain normals are estimated at the end of each flight line. Afterwards, the effect of the incidence angle is added to the point precisions obtained previously by error propagation within the direct georeferencing process. The publication proves that the so obtained point coordinates have an

accuracy better than 1 dm, which is sufficient for many applications. However, for high accuracy demands, a lidar strip adjustment is still necessary to eliminate these systematic errors.

Basically, two types of lidar strip adjustment methods exist: (a) approximate solutions, which can be described as rubber-sheeting co-registration methods that use the 3D terrain points as input only, and (b) rigorous solutions that start from the original scanner and trajectory observations. The main drawback of approximative solutions in comparison to rigorous solutions is depicted in Figure 1.3. Here, the lidar strips are bent across the flight direction before the adjustment. Such a strip deformation, sometimes also denoted as the smiley effect, stems from a constant range measurement error of the scanner, cf. Figure 3.4. This type of error can only be corrected by adjustment if the 3D coordinates of the ground points are formulated through the original scanner measurements and the flight trajectory (*direct georeferencing*). Consequently, with the rigorous approach, the error can be corrected and – most important – no absolute deformation of the lidar block occurs. However, approximative solutions use a rather simple transformation model to minimize discrepancies within the overlap area of lidar strips, e.g. a rigid body or affine transformation. The constant range offset cannot be corrected with these models, instead, the block is deformed due to the uncorrected systematic range errors. Of course, such an effect can be mitigated through the usage of ground-truth-data or by introducing fictional observations into the adjustment. However, for high accuracy applications, a rigorous approach is highly recommended, as errors can be corrected where they originally occur.

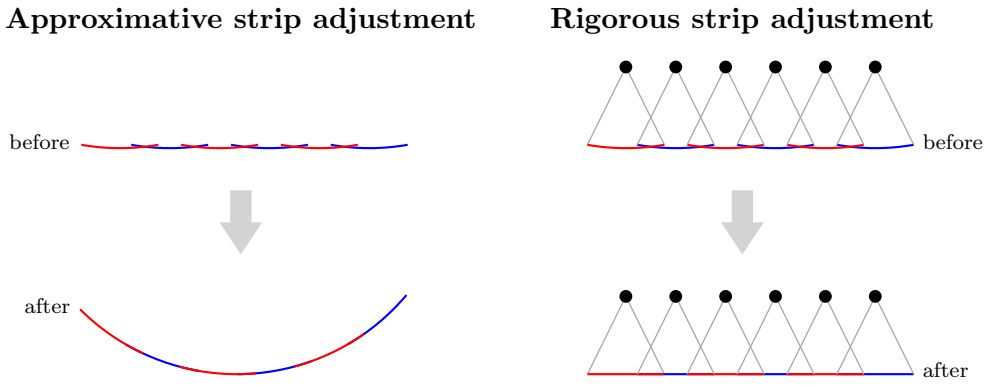

Figure 1.3: Comparison between strip adjustment methods using the 3D points only as input (left) and methods using the flight trajectory and the original scanner measurements as input (right).

An approximative approach was presented by Kraus et al. (2006). It suggests a robust Least Squares Matching (LSM) method to minimize height differences between overlapping strips. The focus lies on the estimation of the 3D translation vector of one strip, i.e. no other transformation parameters are considered in this approach. Since the LSM method originates from photogrammetry, where it is used for matching the intensities of aerial images, the strips have to be rasterized before. It is proposed to derive three raster models from each strip: a Digital Surface Model (DSM), a Digital Terrain Model (DTM), and a Digital Intensity Model. The DSM and DTM are used to estimate the horizontal *and* vertical components of the trans-

lation vector, whereas the DIM only contributes on the horizontal components. The latter is especially useful in flat areas with less height variation but a high contrast in the laser intensity. As raster models are not well suited to represent vertical objects such as vegetation or vertical walls, the disturbing influence of these raster cells is eliminated using a robust least squares adjustment method.

Rigorous solutions, like the one presented in this thesis, differ mainly regarding the estimated parameters and the used correspondences. Many methods concentrate on the estimation of the misalignment between the scanner and the Inertial Navigation System (INS) (Hebel and Stilla, 2012; Toth, 2002). The most extensive parameter models are presented in Kager (2004) and Friess (2006). Correspondences are either generated from the original point cloud or a derivate of it (e.g. interpolated grids or triangulations). Most approaches use planes as corresponding geometric elements. They can be of fixed size or variable size found by segmentation (e.g. rooftops). Kersting et al. (2012) use higher order primitives as correspondences. An overview of strip adjustment methods is presented in Toth (2009) and Habib and Rens (2007).

In the following, a description of some rigorous strip adjustment methods is given. Toth (2002) concentrates on the estimation of the three misalignment angles. The motivation behind this is that the effect of angular errors is proportional to the object distance, while the effect of positional errors does not depend on it, i.e. it is constant. Suitable regions for correspondences are found by a (not further specified) segmentation process. Following the Gruber point distribution in stereo models, these regions are predominantly selected near the borders of the overlapping area of two strips, where differences are more noticeable. For each pair of corresponding segments, a 3D difference vector is determined by correlation matching. These 3D differences are minimized within a Least Squares Adjustment (LSA). Since the vertical coordinate of ground points is usually more reliable than the horizontal ones, a higher weight is assigned to the vertical differences than to the horizontal ones. Similar to the ICP algorithm, the misalignment angles are refined iteratively.

Skaloud and Lichti (2006) present a semi-automatic method for the estimation of the three misalignment angles and the range offset. The aim of this method is not necessarily an area-wide minimization of discrepancies, but rather the estimation of these four calibration parameters with a minimal correlation between them. As further calibration parameters (e.g. lever-arm) are *not* estimated, the authors recommend to optimize the flight conditions and to choose the calibration area in such a way that the systematic influence of these parameters is minimal. A pre-requisite of the method is the manual identification of a sufficient number of suitable planes within the overlap area of the strips. The calibration parameters are then estimated by conditioning the points from overlapping strips to lie in these planes. The adjustment (Gauß-Helmert model) is formulated rigorously, i.e. the functional model includes the scanner, Global Navigation Satellite System (GNSS), and INS measurements as observations, the stochastic model considers their precision (but neglecting correlations), and the plane parameters are estimated together with the calibration parameters. It is demonstrated that the range offset parameter is highly correlated with the misalignment angles and that the planes should vary in slope and orientation to achieve a sufficient de-correlation between the calibration parameters and the plane parameters.

In Habib et al. (2010) two strip adjustment methods are presented: an approximative and a quasi-rigorous method. The approximate method is based on some

restrictive assumptions (such as nearly flat terrain, parallel flight lines, roll and pitch angles equal to zero, profile scanners), which strongly restrict the universality of the method. Some of these restrictions are omitted in the quasi-rigorous method where parts of the flight trajectory are used. However, variations of the pitch and roll angles are not considered, i.e. they are assumed to be zero. Furthermore, the misalignment is formulated through a rotation matrix for small angles, and thus only small misalignment angles can be handled. Both strip adjustment methods minimize the orthogonal distances between points and triangles, whereby the triangles are derived from a Triangular Irregular Network (TIN). Appropriate correspondence areas have to be selected manually. The parameters are estimated by a LSA. Parameters are refined iteratively.

Hebel and Stilla (2012) states that erroneous misalignment angles have the highest impact on the overall accuracy of ground points. Thus, a strip adjustment method which is limited to the estimation of the three misalignment angles is presented. Only flat areas are considered for the minimization of discrepancies between overlapping strips. Within these smooth areas, building facades and roofs are extracted by a RANSAC based segmentation process, whereas ground points are omitted to reduce the overall runtime of the strip adjustment. Corresponding segments are found by comparing their centroids, eigenvalues and normals. Possibly remaining false correspondences are eliminated by a RANSAC approach. In the LSA the point-to-plane distances between corresponding planes are minimized. Although the initial discrepancies between strips are in the range of several meters, parameters are not refined iteratively.

Literature on aerial triangulation Recently, Cucci et al. (2017) proposed to include the raw inertial observations directly into the aerial triangulation instead of using the flight trajectory from a separate GNSS/INS filtering step. It is shown that this is of particular advantage if cheap and lightweight inertial sensors are employed, e.g. on UAVs, and in challenging situations such as mapping in corridors and areas with no GNSS signal reception. We have to acknowledge that this seems to be a valid and useful extension for the hybrid adjustment too. However, this might be very difficult in case of lidar, mainly due to the facts that it is – in contrast to photogrammetry – a continuous measurement system with no redundancy *within* a single strip.

1.4 Resulting publications

The following publications resulted from the work presented in this thesis:

- **First-authorship, peer-reviewed papers:**
  1. Glira et al. (2015a): **Glira, P.**, Pfeifer, N., Briese, C., Ressl, C., 2015. *A correspondence framework for ALS strip adjustments based on variants of the ICP algorithm.* PFG Photogrammetrie, Fernerkundung, Geoinformation 2015, 275–289.
     → awarded with the "Hansa-Luftbild-Preis 2016"
  2. Glira et al. (2015b): **Glira, P.**, Pfeifer, N., Briese, C., Ressl, C., 2015. *Rigorous strip adjustment of airborne laserscanning data based on the ICP algorithm.* ISPRS Annals of Photogrammetry, Remote Sensing and Spatial Information Sciences II-3/W5, 73–80.

3. Glira et al. (2016): **Glira, P.**, Pfeifer, N., Mandlburger, G., 2016. *Rigorous strip adjustment of UAV-based laserscanning data including time-dependent correction of trajectory errors.* Photogrammetric Engineering & Remote Sensing 82, 945–954.

- **Co-authorship, peer-reviewed papers:**

4. Milenković et al. (2015): Milenkovic, M., Pfeifer, N., **Glira, P.**, 2015. *Applying terrestrial laser scanning for soil surface roughness assessment.* Remote Sensing 7, 2007–2045.
5. Wieser et al. (2017): Wieser, M., Mandlburger, G., Hollaus, M., Otepka, J., **Glira, P.**, Pfeifer, N., 2017. *A case study of UAS-borne laser scanning for measurement of tree stem diameter.* Remote Sensing 9, 1154.
6. Vehling et al. (2017): Vehling, L., Baewert, H., **Glira, P.**, Moser, M., Rohn, J., Morche, D., 2017. *Quantification of sediment transport by rockfall and rockslide processes on a proglacial rock slope (Kaunertal, Austria).* Geomorphology 287, 46–57.
7. Zlinszky et al. (2017): Zlinszky, A., Boergens, E., **Glira, P.**, Pfeifer, N., 2017. *Airborne laser scanning for calibration and validation of inshore satellite altimetry: A proof of concept.* Remote Sensing of Environment 197, 35–42.

- **Co-authorship papers:**

8. Mandlburger et al. (2015b): Mandlburger, G., **Glira, P.**, Pfeifer, N., 2015. *UAS-borne lidar for mapping complex terrain and vegetation structure.* GIM International - the Worldwide Magazine For Geomatics 29, 30–33.
9. Mandlburger et al. (2015c): Mandlburger, G., Hollaus, M., **Glira, P.**, Wieser, M., Milenkovic, M., Riegl, U., Pfennigbauer, M., 2015. *First examples from the RIEGL VUX-SYS for forestry applications.* In: Proc. SilviLaser 2015; 28–30 Sep. 2015, La Grande Motte, France.
10. Mandlburger et al. (2015a): Mandlburger, G., Pfennigbauer, M., Riegl, U., Haring, A., Wieser, M., **Glira, P.**, Winiwarter, L., 2015. *Complementing airborne laser bathymetry with UAV-based lidar for capturing alluvial landscapes.* In: Remote Sensing for Agriculture, Ecosystems, and Hydrology XVII, International Society for Optics and Photonics. p. 96370A.
11. Pfeifer et al. (2015): Pfeifer, N., Mandlburger, G., **Glira, P.**, Roncat, A., Mücke, W., Zlinszky, A., 2015. *Lidar: Exploiting the versatility of a measurement principle in photogrammetry.* 55th photogrammetric week , 105–118.
12. Wieser et al. (2016): Wieser, M., Hollaus, M., Mandlburger, G., **Glira, P.**, Pfeifer, N., 2016. *ULS lidar supported analyses of laser beam penetration from different ALS systems into vegetation.* ISPRS Annals of Photogrammetry, Remote Sensing & Spatial Information Sciences 3.
13. Mandlburger et al. (2017): Mandlburger, G., Wenzel, K., Spitzer, A., Haala, N., **Glira, P.**, Pfeifer, N., 2017. *Improved topographic models via*

concurrent airborne lidar and dense image matching. ISPRS Annals of Photogrammetry, Remote Sensing & Spatial Information Sciences 4.

- **Co-authorship, peer-reviewed book contributions:**
  14. Pfeifer et al. (2016): Pfeifer, N., Mandlburger, G., **Glira, P.**, 2016. Laserscanning. Springer Berlin Heidelberg, Berlin, Heidelberg. pp. 1–51.
  15. Hilger et al. (2019) Hilger, L., Dusik, J., Heckmann, T., Haas, F., **Glira, P.**, Pfeifer, N., Vehling, L., Rohn, J., Morche, D., Baewert, H., et al., 2019. *A Sediment Budget of the Upper Kaunertal.* Springer Nature Switzerland. pp. 289–312.

- **First-authorship poster presentations**:
  16. Glira et al. (2013): **Glira, P.**, Briese, C., Kamp, N., Pfeifer, N., 2013. *Simultaneous relative and absolute orientation of point clouds with TLS radomes.* In: EGU General Assembly Conference Abstracts, p. 13116.
  17. Glira et al. (2014): **Glira, P.**, Briese, C., Pfeifer, N., Dusik, J., Hilger, L., Neugirg, F., Baewert, H., 2014. *Accuracy analysis of height difference models derived from terrestrial laser scanning point clouds.* In: EGU General Assembly Conference Abstracts.
  → awarded with the "EGU Poster Award 2015"

- **Co-authorship poster presentations**:
  18. Briese et al. (2013) Briese, C., **Glira, P.**, Pfeifer, N., 2013. *Integration of multi-temporal airborne and terrestrial laser scanning data for the analysis and modelling of proglacial geomorphodynamic processes.* In: EGU General Assembly Conference Abstracts.
  19. Zlinszky et al. (2015) Zlinszky, A., **Glira, P.**, Boergens, E., Pfeifer, N., 2015. *Comparing airborne lidar water surface heights with synchronous envisat altimetry over lake Balaton, Hungary.* In: EGU General Assembly Conference Abstracts.

Note on authorship It is noted, that the sections 2.1, 3.1.1, 3.1.4, 3.2.1, 3.2.2, 4.1, 4.2, and 4.3 are taken largely from the papers Glira et al. (2015a), Glira et al. (2015b), and Glira et al. (2016).

1.5 Thesis organization

The remainder of this thesis is organized in the manner outlined below:

- **Section 2**: The methodological framework of the hybrid adjustment is based on the ICP algorithm. Thus, a brief introduction of the algorithm, including a solution for a simplified version of the algorithm, is presented first.

- **Section 3**: This section summarizes all aspects of the hybrid adjustment. Particular emphasis was laid on providing all the information needed for an own implementation of the proposed method. The section is divided into:

  - **Section 3.1**: This section first describes the geometric relations between the sensor measurements and the object points, namely the direct georeferencing equations for lidar and images, as well as the collinearity equations. These equations are extended by sensor calibration parameters, e.g. for the correction of the polar measurements of the scanner. Then, four models for the correction of the GNSS/INS trajectory are presented. Finally, a summary and categorization of the previously introduced parameters is given.
  - **Section 3.2**: This section is dedicated to the correspondence selection problem. This includes the selection, the matching, and the rejection of correspondences. For the selection step, four different strategies are presented. Finally, the correspondences between the different data types, e.g. between lidar strips and aerial images, are described including the respective objective functions.

- **Section 4**: The various aspects of the hybrid adjustment are demonstrated on the basis of four examples.
- **Section 5**: Summary of the proposed method and conclusions that are drawn from its application.

1.6 Notation

To facilitate the following considerations, some notation is introduced here.

Coordinate systems

s	scanner coordinate system
c	camera coordinate system
i	INS coordinate system
n	navigation coordinate system
e	ECEF coordinate system
m	mapping coordinate system, e.g. UTM

Vectors and matrices

$\mathbf{v}^a$	vector $\mathbf{v}$ expressed in coordinate system with index a
R_a^b	rotation matrix from coordinate system a to coordinate system b
$\mathbf{x}'$	reduced coordinates, e.g. image coordinates reduced to the principal point of a camera

Sets

$\mathcal{N}$	set of points, i.e. a point cloud, $\mathcal{N} = \{1, \dots, n, \dots, N\}$
$\mathcal{S}$	set of lidar/image strips, $\mathcal{S} = \{1, \dots, s, \dots, S\}$
$\mathcal{K}$	set of overlapping lidar strip pairs, $\mathcal{K} = \{1, \dots, k, \dots, K\}$
$\mathcal{L}$	set of laser/lidar scanner, $\mathcal{L} = \{1, \dots, l, \dots, L\}$
$\mathcal{C}$	set of cameras, $\mathcal{C} = \{1, \dots, c, \dots, C\}$
$\mathcal{I}$	set of aerial images, $\mathcal{I} = \{1, \dots, i, \dots, I\}$
$\mathcal{T}$	set of object points, $\mathcal{T} = \{1, \dots, t, \dots, T\}$

$\mathcal{P}$	set of STR-to-STR correspondences, $\mathcal{P} = \{1, \ldots, p, \ldots, P\}$
$\mathcal{Q}$	set of CPC-to-STR correspondences, $\mathcal{Q} = \{1, \ldots, q, \ldots, Q\}$
$\mathcal{V}$	set of IMG-to-STR correspondences, $\mathcal{V} = \{1, \ldots, v, \ldots, V\}$
$\mathcal{R}$	set of IMG-to-IMG correspondences, $\mathcal{R} = \{1, \ldots, r, \ldots, R\}$
$\mathcal{U}$	set of IMG-to-GCP correspondences, $\mathcal{U} = \{1, \ldots, u, \ldots, U\}$

In the hybrid adjustment many different data types are used. To better differentiate between coordinate system indices and objects belonging to one of the sets above, the index of a specific object is surrounded by square brackets. For instance, the transformation of the t-th object point from the n-system to the e-system is denoted by:

$$\mathbf{x}^e_{[t]} = R^e_n \mathbf{x}^n_{[t]}$$

Another example are the image observations of the t-th object point in the i-th image, given in the coordinate system of the camera, which are denoted by:

$$\bar{x}^c_{[i][t]}, \bar{y}^c_{[i][t]}$$

2 The ICP algorithm as methodological framework

2.1 The ICP algorithm

The methodological framework of the hybrid adjustment presented herein is formed by the Iterative Closest Point (ICP) algorithm (Besl and McKay (1992), Chen and Medioni (1992)). This algorithm is used to improve the alignment of two (or more) point clouds (Figure 2.1). Nowadays the term ICP does not necessarily refer to the algorithm presented in the original publications, but rather to a group of surface matching algorithms which have in common the following aspects:

I : correspondences are established *iteratively*
C : as correspondence the closest point, or more generally, the *corresponding* point, is used
P : correspondences are established on a *point basis*.

The hybrid adjustment of lidar point clouds and aerial images presented in this work is methodologically built upon these three basic aspects.

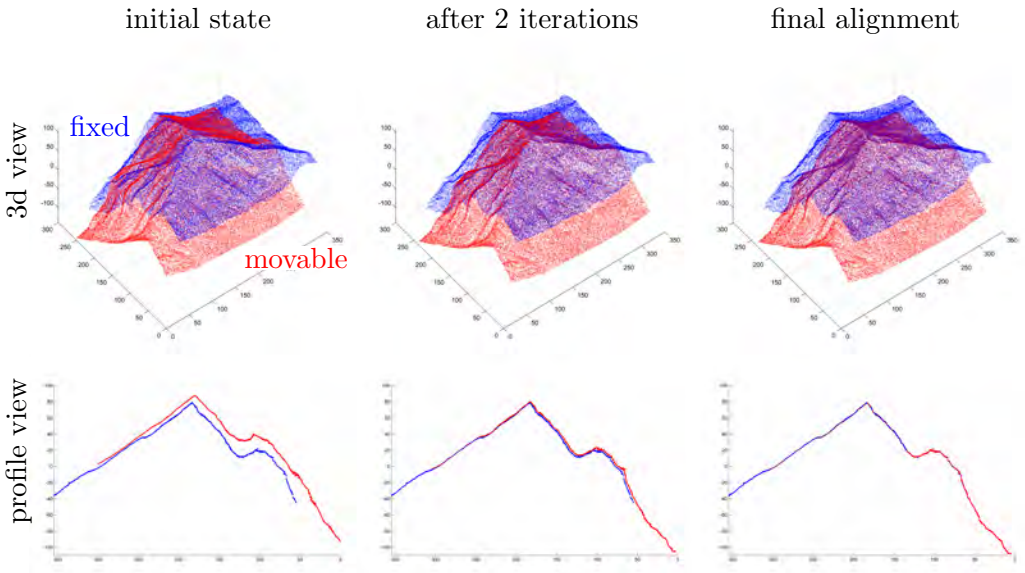

Figure 2.1: Matching of two overlapping lidar point clouds with the ICP algorithm.

The basic version of the ICP algorithm is applicable to two point clouds only. As can be seen in Figure 2.2, these point clouds initially don't match very well, i.e. there are discrepancies within the overlapping area of the point clouds. The goal

of the ICP algorithm is to minimize these discrepancies. This can be achieved by transforming *iteratively* the so called movable point cloud, whereas the position of the other point cloud remains fixed. It is noted that to apply the algorithm, a good estimate of the initial relative orientation of the point clouds is necessary. This main requirement is typically fulfilled in airborne lidar, especially if priors for the mounting calibration of the laser scanners are known.

The framework of the ICP algorithm can be broken down into five main steps (see Figure 2.2):

1. **Selection**: A subset of points is selected within the overlap area in one point cloud.
2. **Matching**: Find the corresponding points of the selected subset in the other point cloud.
3. **Rejection**: False correspondences (outliers) are rejected on the basis of the compatibility of points.
4. **Minimization**: Estimation of transformation parameters (for the movable point cloud) by minimizing the distances between corresponding points.
5. **Transformation**: Transformation of the movable point cloud with the estimated parameters.

Finally, a suitable convergence criterion is tested. If it is not met, the process restarts from step 1 (or step 2 if point selection is not repeated iteratively).

2.2 A basic implementation of the ICP algorithm

In this section the solution for a simplified[1] version of the ICP algorithm is described. This serves as a basis for section 3, where the modifications and extensions that have been made to the ICP framework will be presented.

Let $\mathbf{p}_{[n]}$ and $\mathbf{q}_{[n]}$, $n \in \mathcal{N} = \{1, \ldots, n, \ldots, N\}$, be two point clouds with the same number of points N (Figure 2.3). In its initial state the point clouds are already roughly aligned, i.e. the discrepancies within the overlap area of the two point clouds are small in relation to their object size. The point cloud $\mathbf{p}_{[n]}$ is defined as *fixed* in object space. The aim of the ICP algorithm is to find a transformation T for the *movable* point cloud $\mathbf{q}_{[n]}$ such that the discrepancies between the two point clouds are minimized. In this basic implementation, a rigid body transformation is used to transform the movable point cloud $\mathbf{q}_{[n]}$. Thus, the transformation T is defined by

$$T(\mathbf{q}_{[n]}) = R\,\mathbf{q}_{[n]} + \mathbf{t} \tag{2.1}$$

where $\mathbf{t}$ denotes a 3-by-1 translation vector and R denotes a 3-by-3 orthogonal rotation matrix.

The correspondences between the two point clouds are established by pairing *each* point in $\mathbf{p}_{[n]}$ to the nearest neighbour (nn) in $\mathbf{q}_{[n]}$; this gives a set $\mathcal{P}$ of N correspondences, $p \in \mathcal{P} = \{1, \ldots, p, \ldots, N\}$.

[1] It is noted that the *selection* and *rejection* steps described above are skipped in this example.

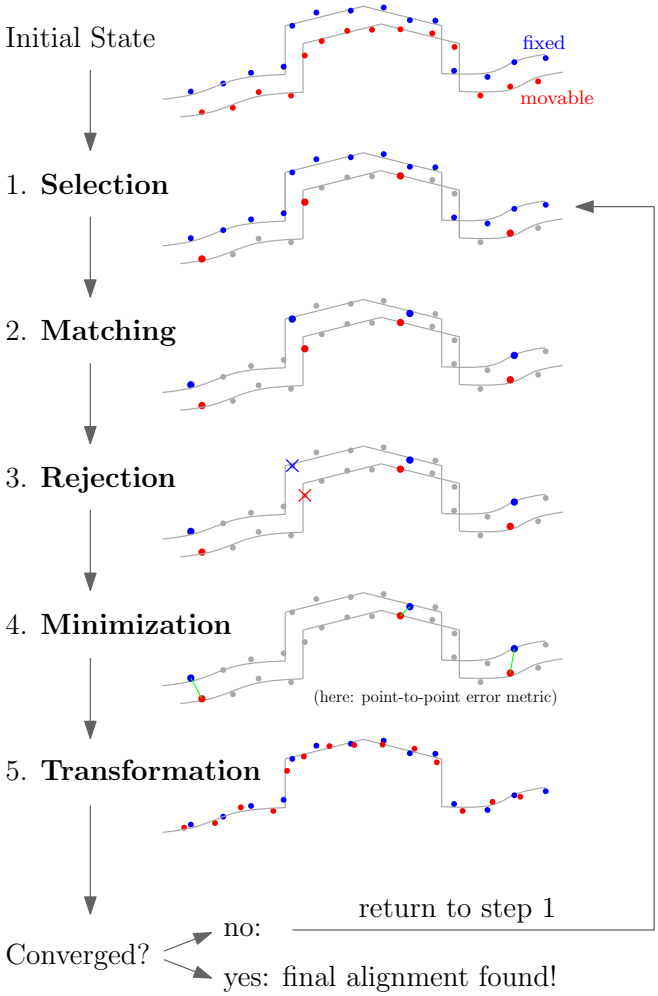

Figure 2.2: Visualization of the five basic ICP steps for two overlapping point clouds (blue = fixed, red = movable, green = correspondence).

To describe the discrepancies between these corresponding points different *error metrics* can be chosen. Often the *euclidean distance*, also denoted as *point-to-point distance*, is used for this purpose:

$$d_{[p]} = ||\mathbf{p}_{[p]} - \mathbf{q}_{[p]}|| \tag{2.2}$$

Now the objective of the ICP optimization problem can be formulated as

$$\Omega = \underset{R,\mathbf{t}}{\operatorname{argmin}} \left\{ \sum_{[p]=1}^{N} d_{[p]}^2 \right\} \tag{2.3}$$

As the sum of squared point-to-point distances is minimized here, this corresponds to a *least squares problem*. A closed form solution for this problem – i.e. a solution without iterations and no need for initial parameter values – has been proposed by Horn (1987). We will use this solution to directly estimate the rotation matrix R and the translation vector $\mathbf{t}$ for the movable point cloud from our set of correspondences.

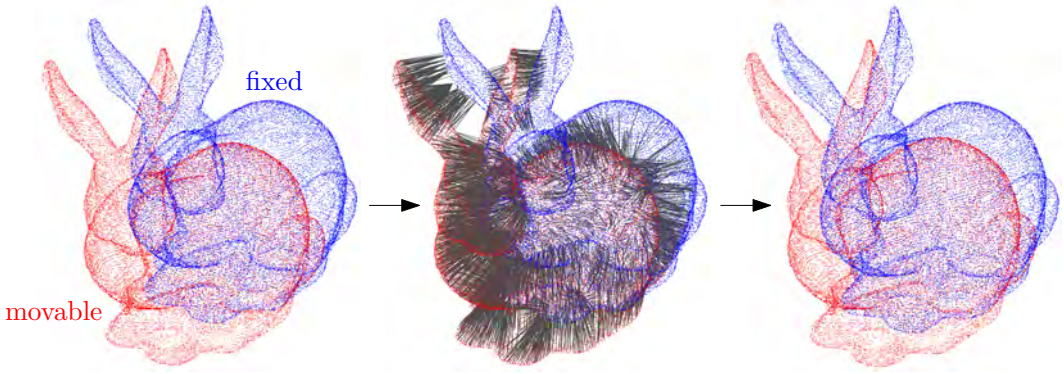

Figure 2.3: A single iteration of the ICP algorithm: Initial state of the point clouds (left), established correspondences (center), and point clouds after transformation (right). A video of the ICP alignment process can be found at https://youtu.be/uzOCS_gdZuM.

We start by computing the centroids of both point clouds by

$$\mathbf{p}_c = \frac{\sum_{n=1}^{N} \mathbf{p}_{[n]}}{N} \qquad \mathbf{q}_c = \frac{\sum_{n=1}^{N} \mathbf{q}_{[n]}}{N} \tag{2.4}$$

Now the reduced coordinates are given by

$$\mathbf{p}'_{[p]} = \mathbf{p}_{[p]} - \mathbf{p}_c \qquad \mathbf{q}'_{[p]} = \mathbf{q}_{[p]} - \mathbf{q}_c \qquad p \in \mathcal{P} = \{1, \ldots, p, \ldots, N\} \tag{2.5}$$

where the points are ordered in both point clouds according to the previously established correspondences. Now the covariance matrix can be computed by

$$S = PQ^\top \tag{2.6}$$

where P and Q are 3-by-N matrices that have $\mathbf{p}'_{[p]}$ and $\mathbf{q}'_{[p]}$ as columns, respectively. From the singular value decomposition of the covariance matrix

$$S = U\Sigma V^\top \tag{2.7}$$

the rotation matrix R and the translation vector $\mathbf{t}$ can now be directly computed by

$$R = V \begin{bmatrix} 1 & & \\ & 1 & \\ & & \frac{1}{\det(UV^\top)} \end{bmatrix} U^\top \tag{2.8}$$

$$\mathbf{t} = \mathbf{q}_c - R\,\mathbf{p}_c \tag{2.9}$$

It should be noted, that the ICP algorithm presented in this section has several limitations and is therefore limited in practice to a few special applications. Most importantly the point clouds need to have the same number of points and need to be fully overlapping, i.e. they must describe the same object. Due to these limitations, a huge number of modifications were derived from the original works of Besl and McKay (1992) and Chen and Medioni (1992). They refer to the selection of points, the weighting of correspondences, the metric for measuring the distance between

corresponding points (*error metric*), and other aspects. A summary has been given by Rusinkiewicz and Levoy (2001), who suggest that a better expansion of the acronym ICP would be iterative *corresponding* point instead of the original iterative *closest* point. Planitz et al. (2005) summarize methods based on intrinsic surface parameters for solving the correspondence problem.

3 Hybrid adjustment

The hybrid adjustment simultaneously optimizes the orientation of lidar strips (STR) and aerial images (IMG) considering ground truth data in the form of control point clouds (CPC) and ground control points (GCP). Different types of correspondences are thereby used as links between these data types (Figure 3.1).

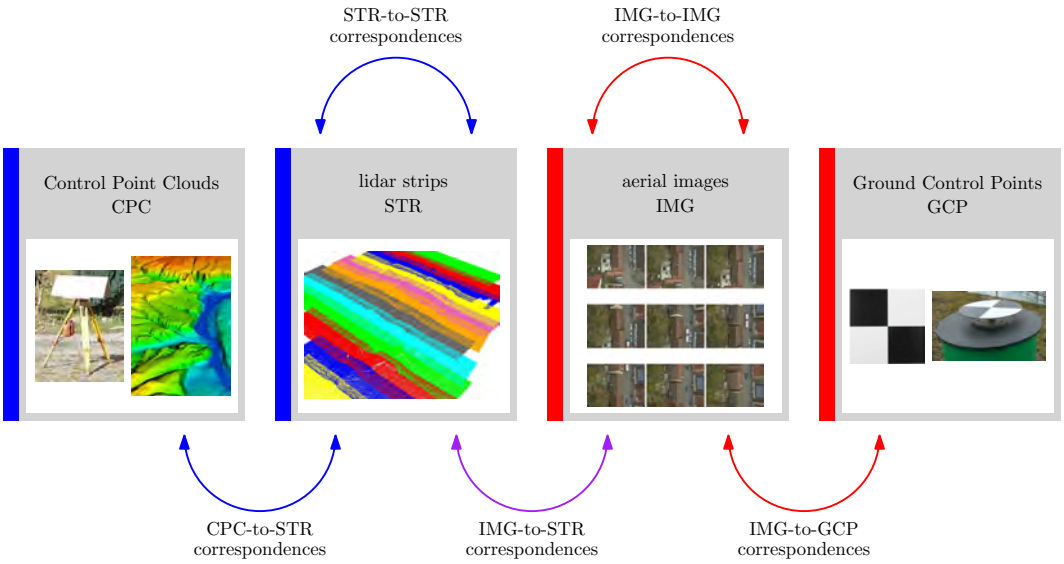

Figure 3.1: Input data and correspondences used in the hybrid adjustment.

The methodological basis of the hybrid adjustment is formed by the correspondence framework of the ICP algorithm described in the previous chapter. On this basis, several extensions have been made:

- While the original ICP algorithm is restricted to two point clouds only, the method presented in this work can handle an **arbitrary number of point clouds**. These point clouds are either lidar strips, point clouds derived from image observations (image tie points), or point clouds that are fixed in object space (ground truth data). The alignment of all point clouds is optimized simultaneously in a single least squares adjustment (opposed to e.g. a sequential alignment of overlapping point clouds pairs).
- Instead of using *each* point as correspondence, four different **correspondence selection strategies** have been developed. The main differences among these strategies are their computational complexity and their suitability for different terrain types. They are denoted as:
  - **Random Sampling (RS)**
  - **Uniform Sampling (US)**

  - **Normal Space Sampling (NSS)**
  - **Maximum Leverage Sampling (MLS)**

  These strategies are described in section 3.2.1. The thereby selected correspondences are restricted to the overlapping areas of the point clouds.

- As error metric the **point-to-plane distance** is used instead of the point-to-point distance (section 3.2.4). As a consequence, corresponding points do not need to be identical in object space, but they only need to belong to the same (tangent) plane (e.g. roof or street). Moreover, the point-to-plane distance can be better adapted to different point densities and fewer iterations need to be computed due to a faster convergence behavior.

- Several **correspondence rejection criteria** have been defined for the a priori detection and elimination of false correspondences (outliers) (section 3.2.3). As these rejection criteria do not guarantee that all outliers are removed, a robust adjustment method is used for the removal of the remaining ones.

- Instead of using a rather simple transformation model (e.g. a rigid body transformation), **point clouds are modelled in a rigorous way considering the original sensor measurements**, cf. section 3.1. For instance, the point cloud of a lidar strip is modelled by the original flight trajectory, the original polar measurements of the scanner and its mounting on the sensor platform.

- The integration of the **bundle adjustment of aerial images** (*aerial triangulation*) into the ICP framework allows the simultaneous orientation and calibration of lidar point clouds and aerial images. The images are thereby connected to the lidar point clouds by the sparse feature point cloud (image tie points) and by the common flight trajectory.

- The **calibration parameters** of the lidar scanner and the cameras can be estimated by adjustment, i.e. the systematic range and angle measurement errors of the scanners as well as the focal length, principal point, and distortion parameters of the cameras (*interior orientation*). Thereby an arbitrary number of different scanners and cameras can be handled.

- Depending on the systematic errors of the flight trajectory, four different models can be chosen for the **correction of the flight trajectory** (section 3.6):
  - **Bias Trajectory Correction Model (BTCM)**
  - **Linear Trajectory Correction Model (LTCM)**
  - **Quadratic Trajectory Correction Model (QTCM)**
  - **Spline Trajectory Correction Model (STCM)**

- **Ground truth data** is considered in the form of ground control points (GCP) for the imagery or control point clouds (CPC) for the lidar strips. The ground truth data is used to define the absolute orientation of the lidar and the image block.

- In contrast to the original ICP algorithm, observations are weighted in the adjustment according to their measurement precision.

The remainder of this chapter is organized as follows: basic equations and the parameter model of the adjustment is discussed in the following section 3.1. The various types of correspondences which define the adjustment's observations is described in section 3.2. Finally, the whole workflow and the solution of the hybrid adjustment are summarized in section 3.3.

3.1 Mathematical foundation and parameter model

We start in this section by describing the equations that form the core of the hybrid adjustment of lidar point clouds and aerial images. These are the equations that relate the measurements of the sensors on the aircraft (laser scanner(s), camera(s), GNSS, INS) to the observed object points on the ground (Figure 3.2). We will need these equations in section 3.2 to establish the correspondences and thereby formulate the adjustment's observations.

In the case of lidar point clouds, the relation between sensor measurements and ground points is given by the *direct georeferencing equation*, which we will describe together with its extension by additional sensor calibration parameters in section 3.1.1. In the case of aerial images the relation is given by the *direct georeferencing equation* (section 3.1.2) *and* the *collinearity equations* (section 3.1.3), extended by additional image distortion parameters. For the correction of the GNSS/INS flight trajectory – which is shared by lidar strips and aerial images through the respective direct georeferencing equations – four different models are described in section 3.1.4. Finally, a summary of the complete parameter model is given in section 3.1.5.

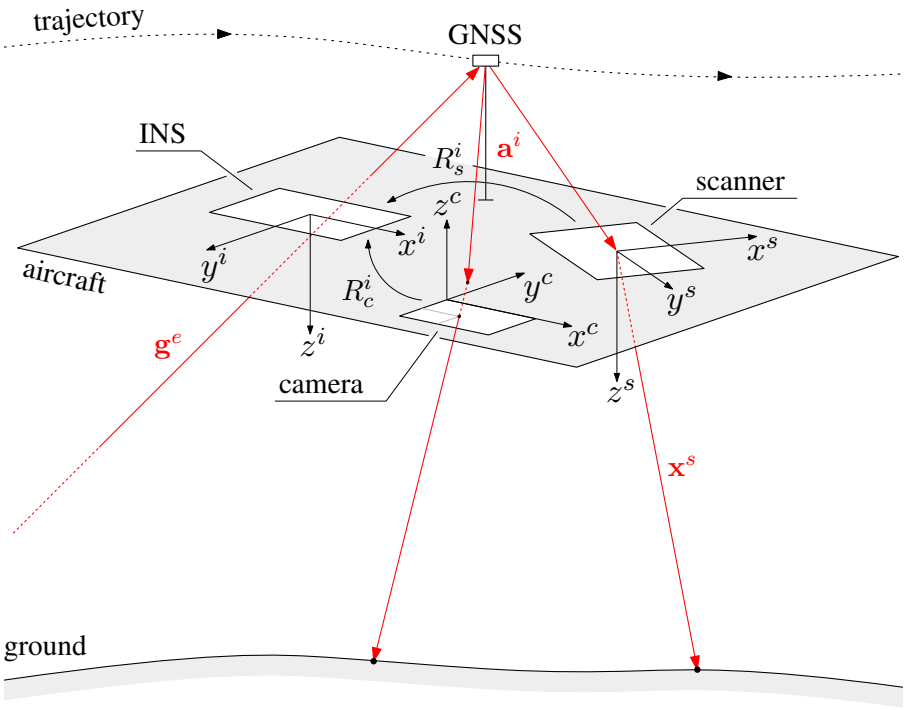

Figure 3.2: Schematic representation of a minimal set of sensors on an aircraft.

3.1.1 Direct georeferencing of lidar point clouds

The direct georeferencing equation is used to generate georeferenced point clouds from the measurements of a lidar multi-sensor system. This requires three types of input data (Hebel and Stilla, 2012; Skaloud and Lichti, 2006):

1. the **polar measurements of the scanner**,
2. the **flight trajectory of the aircraft** and
3. the **mounting calibration parameters**.

Combining all these measurements, the point coordinates of an object point $[t]$, measured by a laser scanner $[l]$ at time t are given by

$$\mathbf{x}^e_{[t]}(t) = \mathbf{g}^e(t) + R^e_n(t)\, R^n_i(t) \left(\mathbf{a}^i_{[l]} + R^i_{s[l]}\, \mathbf{x}^s_{[t]} \right) \tag{3.1}$$

whereby we assume to have in the hybrid adjustment later on a set $\mathcal{L}$ of L laser scanners and a set $\mathcal{T}$ of T object points:

$$l \in \mathcal{L} = \{1, \ldots, l, \ldots, L\}, t \in \mathcal{T} = \{1, \ldots, t, \ldots, T\}$$

In equation (3.1) the superscript of a vector denotes the coordinate system in which it is defined, whereas the notation $R^{\text{target}}_{\text{source}}$ is used to denote a transformation from a source coordinate system to a target coordinate system (cf. section 1.6). Consequently, four coordinate systems appear in equation (3.1):

s-system	scanner coordinate system
i-system	INS coordinate system, often also denoted as body coordinate system
n-system	navigation coordinate system, equal to a local-level coordinate system (x = north, y = east, z = nadir)
e-system	Earth-Centered, Earth-Fixed (ECEF) coordinate system

Definitions of these coordinate systems can be found in Bäumker and Heimes (2001). Furthermore, equation (3.1) includes:

$\mathbf{x}^s_{[t]}$ ... 3-by-1 vector with the coordinates of the laser point $[t]$ in the s-system. Generally, these coordinates can be expressed as a function of the range $\rho_{[t]}$ and two angles $\alpha_{[t]}$ and $\beta_{[t]}$:

$$\mathbf{x}^s_{[t]}(t) = \mathbf{x}^s_{[t]}(\rho_{[t]}, \alpha_{[t]}, \beta_{[t]}) \tag{3.2}$$

$R^i_{s[l]}$ ... 3-by-3 rotation matrix describing the rotation from the s-system to the i-system, i.e. from the coordinate system of the laser scanner $[l]$ to the INS. This rotation is usually denoted as *(boresight) misalignment* and is parametrized through three Euler angles:

$$R^i_{s[l]} = R^i_{s[l]}(\alpha_{1[l]}, \alpha_{2[l]}, \alpha_{3[l]}) \tag{3.3}$$

$\mathbf{a}^i_{[l]}$ ... 3-by-1 vector describing the positional offset between the GNSS antenna and the origin of the s-system. This vector is usually denoted as *lever-arm*:

$$\mathbf{a}^i_{[l]} = \begin{bmatrix} a^i_{x[l]} & a^i_{y[l]} & a^i_{z[l]} \end{bmatrix}^{\mathrm{T}} \tag{3.4}$$

$R^n_i(t)$ ... 3-by-3 rotation matrix describing the rotation from the i-system to the n-system as first part of the trajectory data. This rotation can be estimated from the GNSS/INS measurements and is parametrized through three Euler angles roll ϕ, pitch θ, and yaw ψ:

$$R^n_i(t) = R^n_i(\phi(t), \theta(t), \psi(t)) \tag{3.5}$$

$R^e_n(t)$ ... 3-by-3 rotation matrix describing the rotation from the n-system to the e-system. This rotation is not observed, but is a function of the longitude λ and latitude φ corresponding to the actual value of $\mathbf{g}^e(t)$:

$$R^e_n(t) = R^e_n(\lambda(t), \varphi(t)) \tag{3.6}$$

$\mathbf{g}^e(t)$ ... 3-by-1 vector describing the position of the GNSS antenna in the e-system as second part of the trajectory data:

$$\mathbf{g}^e(t) = \begin{bmatrix} g^e_x(t) & g^e_y(t) & g^e_z(t) \end{bmatrix}^{\mathrm{T}} \tag{3.7}$$

It should be noted at this point, that the hybrid adjustment method presented herein is fully performed in the e-system. Only afterwards, the points obtained by equation (3.1) are projected from the e-system to an arbitrary mapping coordinate system (m-system), e.g. UTM. This has the main advantage that the surface distortions applied in the m-system have not to be considered in the adjustment (Zhang and Shen, 2013).

Side note Often a provided flight trajectory already relates to the s-system (in contrast to the definition given above). In this case

- the angles roll ϕ, pitch θ, and yaw ψ directly describe the rotation from the s-system of the laser scanner $[l]$ to the n-system:

$$R^n_{s[l]}(t) = R^n_i(t)\, R^i_{s[l]} = R^n_{s[l]}(\phi(t), \theta(t), \psi(t)) \tag{3.8}$$

- $\mathbf{g}^e(t)$ relates to the origin of the s-system,
- and the lever-arm $\mathbf{a}^i_{[l]}$ can be omitted in equation (3.1).

As a result, equation (3.1) simplifies to:

$$\mathbf{x}^e_{[t]}(t) = \mathbf{g}^e(t) + R^e_n(t)\, R^n_{s[l]}(t)\, \mathbf{x}^s_{[t]} \tag{3.9}$$

It is emphasized that any measurement in equation (3.1) can be affected by systematic errors, which in turn cause a systematic (nonlinear) deformation of the lidar

strip (Glennie, 2007; Habib and Rens, 2007). To minimize these errors within the adjustment, additional calibration and correction parameters have to be introduced into the direct georeferencing equation (3.1).

Mounting calibration parameters The six mounting calibration parameters are represented in equation (3.1) by the rotation matrix $R^i_{s[l]}$, defined by the three misalignment angles $\alpha_{1[l]}$, $\alpha_{2[l]}$, $\alpha_{3[l]}$, and by the lever-arm $\mathbf{a}^i_{[l]}$, defined by the three components $a^i_{x[l]}$, $a^i_{y[l]}$, and $a^i_{z[l]}$. In most of the cases, the mounting calibration parameters are already known in advance, e.g. from a previously performed calibration or construction plans of the sensor platform. However, these values may be inaccurate or outdated. The effect of an erroneous mounting calibration is visualized in Figure 3.3. Especially an incorrect misalignment, which is difficult to determine by terrestrial measurements, can cause very large point displacements because the effect of angular errors is directly proportional to the object distance ρ. For this reason many strip adjustment methods concentrate on the estimation of $R^i_{s[l]}$, neglecting other parameters (e.g. Toth (2002), Hebel and Stilla (2012)). We recommend to fully re-estimate the mounting calibration parameters by adjustment. It is noted that due to correlations, especially to the trajectory correction parameters (cf. section 3.1.4), the estimated values are usually not transferable to other flight missions.

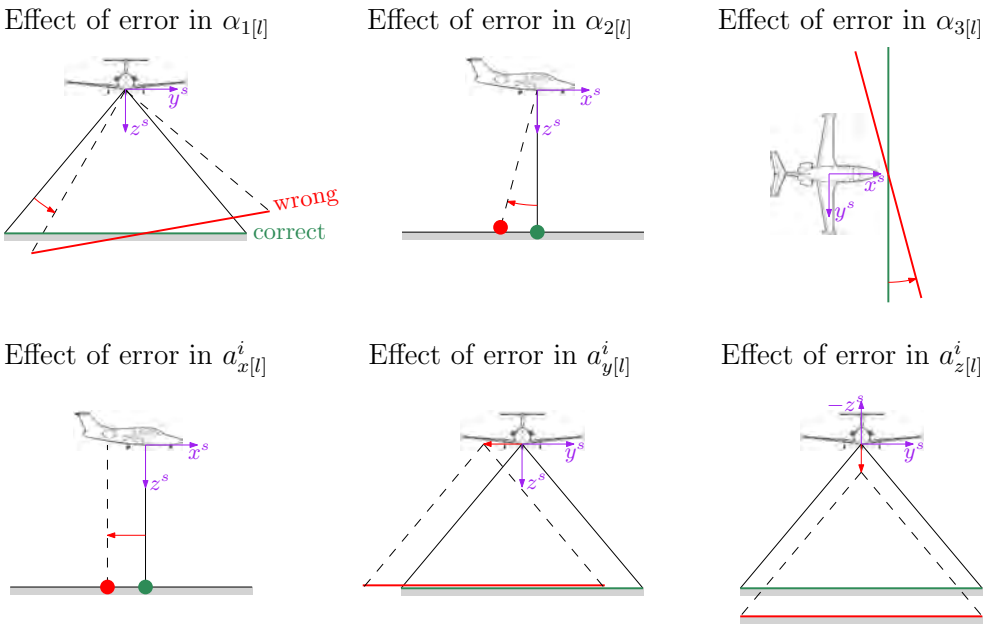

Figure 3.3: Effect of an erroneous mounting calibration (top: misalignment angles, bottom: lever-arm) on the georeference of lidar strips.

3.1.1.1 Extension by scanner calibration parameters

The scanner calibration parameters compensate for the systematic errors of the lidar scanner's measurements $\mathbf{x}^s_{[t]}$. A comprehensive analysis of scanner-related errors and their causes can be found in Katzenbeisser (2003). The specific choice of parameters primarily depends on the construction type of the scanner, especially on its beam

deflection mechanism. For example, the parameters required to appropriately model the errors of scanners that deflect the laser beam only in one direction (*linear scanners*), differ from those that deflect the laser beam in a circular pattern (*nutating scanners* or *Palmer scanner*). Hence, it is difficult to give a general recommendation. Instead, we propose a calibration model which is universally applicable, although it may not be the optimal choice in any case. Therefore we formulate $\mathbf{x}^s_{[t]}$, according to equation (3.2), for an object point $[t]$ as a function of the polar coordinates $\rho_{[t]}$, $\alpha_{[t]}$, and $\beta_{[t]}$:

$$\mathbf{x}^s_{[t]} = \begin{bmatrix} \rho_{[t]} \cos\alpha_{[t]} \sin\beta_{[t]} \\ \rho_{[t]} \sin\alpha_{[t]} \\ \rho_{[t]} \cos\alpha_{[t]} \cos\beta_{[t]} \end{bmatrix}^s \tag{3.10}$$

For each polar coordinate two calibration parameters are introduced, an offset (bias) and a scale parameter. This yields to three offset parameters ($\Delta\rho_{[l]}$, $\Delta\alpha_{[l]}$, $\Delta\beta_{[l]}$) and three scale parameters ($\varepsilon_{\rho[l]}$, $\varepsilon_{\alpha[l]}$, $\varepsilon_{\beta[l]}$) which are defined by

$$\rho_{[t]} = \Delta\rho_{[l]} + \rho_{0[t]} \cdot (1 + \varepsilon_{\rho[l]}) \tag{3.11}$$

$$\alpha_{[t]} = \Delta\alpha_{[l]} + \alpha_{0[t]} \cdot (1 + \varepsilon_{\alpha[l]}) \tag{3.12}$$

$$\beta_{[t]} = \Delta\beta_{[l]} + \beta_{0[t]} \cdot (1 + \varepsilon_{\beta[l]}) \tag{3.13}$$

where the original scanners's measurements are denoted by $\rho_{0[t]}$, $\alpha_{0[t]}$, and $\beta_{0[t]}$. The corrections of the scanner measurements are shown in Figure 3.4 exemplarily for a constant range offset $\Delta\rho_{[l]}$ and a constant scan angle offset $\Delta\alpha_{[l]}$.

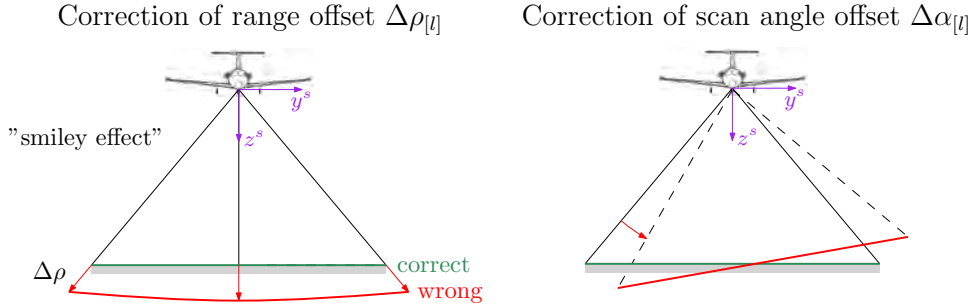

Figure 3.4: The scanner calibration parameters correct for systematic errors of range and angle measurements. This figure shows (on the left) the correction of a constant range offset, which leads to a bending of the lidar strip across the flight direction, and (on the right) the correction of a scan angle offset, e.g. due to a zero-point error of the angular encoder.

Example Linear scanners deflect the laser beam only in one direction (usually across the flight track). Thus, $\alpha_{[t]}$ can be interpreted as the beam deflection angle, whereas $\beta_{[t]}$ is equal to zero. The parameters associated with $\beta_{[t]}$, i.e. $\Delta\beta_{[l]}$ and $\varepsilon_{\beta[l]}$, can be omitted in this case. The remaining parameters compensate for a range finder offset error ($\Delta\rho_{[l]}$), a range finder scale error ($\varepsilon_{\rho[l]}$), a zero-point error of the angular encoder ($\Delta\alpha_{[l]}$), and a scale error of the angular encoder ($\varepsilon_{\alpha[l]}$). However,

these parameters may also compensate for other correlated (and possibly unknown) effects. For example, the parameter $\varepsilon_{\alpha[l]}$ not only serves to correct an angular scale error but also minimizes the influence of the atmospheric refraction. Similarly, the parameter $\varepsilon_{\rho[l]}$, which primarily corrects a range finder scale error, may also compensate range errors caused by the atmospheric propagation delay.

3.1.2 Direct georeferencing of aerial images

The exterior orientation of an image – also denoted as image *pose* in the field of computer vision – is defined by the position of the projection center of the camera and the rotation of the image with respect to the object coordinate system, often described in form of a rotation matrix. Under the assumption that the exposure time t of an image is known, the exterior orientation of an image can be directly derived from:

1. the **flight trajectory of the aircraft** and
2. the **mounting calibration parameters**

We denote this type of images as **coupled images**, as their exterior orientation is coupled to the flight trajectory. The projection center and the rotation matrix of these images are given for an image $[i]$ at time t by:

$$\mathbf{x}^e_{0[i]}(t) = \mathbf{g}^e(t) + R^e_n(t)\, R^n_i(t)\, \mathbf{a}^i_{[c]} \tag{3.14}$$

$$R^e_{c[i]}(t) = R^e_n(t)\, R^n_i(t)\, R^i_{c[c]} \tag{3.15}$$

whereby the camera coordinate system (c-system) is newly introduced here (cf. section 1.6). In addition to the entities already introduced in equation (3.1), we further specify:

$\mathbf{x}^e_{0[i]}(t)$ ... 3-by-1 vector with the coordinates of the projection center of the image $[i]$ in the e-system:

$$\mathbf{x}^e_{0[i]}(t) = \begin{bmatrix} X^e_{0[i]}(t) & Y^e_{0[i]}(t) & Z^e_{0[i]}(t) \end{bmatrix}^{\mathrm{T}} \tag{3.16}$$

$R^e_{c[i]}$ ... 3-by-3 rotation matrix describing the rotation from the c-system to the e-system. Thus, this rotation matrix describes the three-dimensional rotation, or attitude, of the camera with respect to the object coordinate system, defined as e-system in this work. It is parametrized through three Euler angles $\omega_{[i]}$, $\varphi_{[i]}$, $\kappa_{[i]}$:

$$R^e_{c[i]} = R^e_{c[i]}(\omega_{[i]}, \varphi_{[i]}, \kappa_{[i]}) \tag{3.17}$$

$R^i_{c[c]}$ ... 3-by-3 rotation matrix describing the rotation from the c-system to the i-system, i.e. from the camera to the INS. In analogy to the laser scanner case, this rotation is denoted as *(boresight) misalignment* and is parametrized through three Euler angles:

$$R^i_{c[c]} = R^i_{c[c]}(\beta_{1[c]}, \beta_{2[c]}, \beta_{3[c]}) \tag{3.18}$$

$\mathbf{a}^i_{[c]}$ ... 3-by-1 vector describing the positional offset between the GNSS antenna and the projection center of the camera. This vector is denoted as *lever-arm*:

$$\mathbf{a}^i_{[c]} = \begin{bmatrix} a^i_{x[c]} & a^i_{y[c]} & a^i_{z[c]} \end{bmatrix}^{\mathrm{T}} \tag{3.19}$$

In the hybrid adjustment the mounting calibration parameters of the camera $R^i_{c[c]}$ and $\mathbf{a}^i_{[c]}$ are estimated. However, if the residuals show systematic patterns, more flexibility for each image might be necessary. For this, additional correction parameters for the exterior orientation of an image are introduced, i.e. three correction parameters $\Delta X^e_{0[i]}, \Delta Y^e_{0[i]}, \Delta Z^e_{0[i]}$ for the position of the projection center and three correction parameters $\Delta\omega_{[i]}, \Delta\varphi_{[i]}, \Delta\kappa_{[i]}$ for the rotation of an image. These parameters must be observed through fictional observations (section 3.3) to honor their zero expectation and to keep the coupling to the trajectory intact.

Exception loose images In practice often the time stamps t of the images are unknown or no GNSS/INS trajectory is available, e.g. if the imagery was collected independently from the lidar point clouds. In such cases the direct georeferencing equation can not be used. Instead, the six elements of the exterior orientation of the images – that is $X^e_{0[i]}$, $Y^e_{0[i]}$, $Z^e_{0[i]}$, $\omega_{[i]}$, $\varphi_{[i]}$, $\kappa_{[i]}$ – can directly be estimated by adjustment (cf. Table 3.3). We denote these type of images in the following as **loose images**.

3.1.3 Collinearity equations

The collinearity equations relate the 2D image coordinates with the 3D object coordinates of a single point (Figure 3.5). They can be written for an object point $[t]$, which was observed in an image $[i]$ taken by a camera $[c]$ as:

$$\bar{x}^c_{[i][t]} = x^c_{0[c]} - c^c_{[c]} \frac{r_{11}(X^e_{[t]} - X^e_{0[i]}) + r_{21}(Y^e_{[t]} - Y^e_{0[i]}) + r_{31}(Z^e_{[t]} - Z^e_{0[i]})}{r_{13}(X^e_{[t]} - X^e_{0[i]}) + r_{23}(Y^e_{[t]} - Y^e_{0[i]}) + r_{33}(Z^e_{[t]} - Z^e_{0[i]})} \tag{3.20}$$

$$\bar{y}^c_{[i][t]} = y^c_{0[c]} - c^c_{[c]} \frac{r_{12}(X^e_{[t]} - X^e_{0[i]}) + r_{22}(Y^e_{[t]} - Y^e_{0[i]}) + r_{32}(Z^e_{[t]} - Z^e_{0[i]})}{r_{13}(X^e_{[t]} - X^e_{0[i]}) + r_{23}(Y^e_{[t]} - Y^e_{0[i]}) + r_{33}(Z^e_{[t]} - Z^e_{0[i]})} \tag{3.21}$$

whereby we assume to have in the hybrid adjustment later on a set $\mathcal{C}$ of C cameras, a set $\mathcal{I}$ of I images and a set $\mathcal{T}$ of T object points:

$$c \in \mathcal{C} = \{1, \ldots, c, \ldots, C\}, i \in \mathcal{I} = \{1, \ldots, i, \ldots, I\}, t \in \mathcal{T} = \{1, \ldots, t, \ldots, T\}$$

The superscript e denotes the ECEF coordinate system and the superscript c the camera coordinate system. Furthermore, the collinearity equations include:

$\bar{x}^c_{[i][t]}, \bar{y}^c_{[i][t]}$	...	undistorted image coordinates of object point $[t]$ in image $[i]$
$x^c_{0[c]}, y^c_{0[c]}$	...	coordinates of the principal point of camera $[c]$
$c^c_{[c]}$	...	principal distance of camera $[c]$
$X^e_{0[i]}, Y^e_{0[i]}, Z^e_{0[i]}$	...	coordinates of the projection center of image $[i]$
r_{ij}	...	the elements of the rotation matrix $R^e_{c[i]}$
$X^e_{[t]}, Y^e_{[t]}, Z^e_{[t]}$	...	coordinates of the object point $[t]$

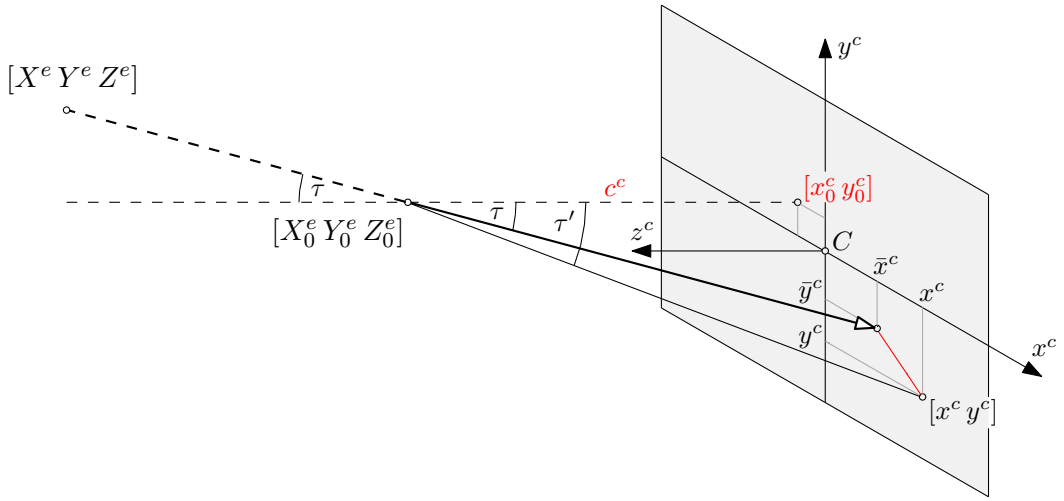

Figure 3.5: The collinearity equations describe the relation between image and object coordinates. The deviation from an ideal perspective is described by the image distortion parameters.

In most of the cases it is necessary to extend the collinearity equations with additional parameters, e.g. to deal with distorted imagery or to account for distortions due to cartographic projections (Kraus, 1997, p. 280). In this work, we exemplify in the next section the extension of the collinearity equations by introducing *image distortion parameters*.

3.1.3.1 Extension by image distortion parameters

The collinearity equations, as stated above, are valid for an ideal perspective camera only. The deviation from this ideal perspective is modeled by the image distortion coefficients. They form, together with the coordinates of the projection center and the principal distance, the *camera calibration parameters*.

The estimation of a proper camera calibration in a *self-calibrating bundle adjustment* is a main requirement for the accurate reconstruction of the Earth's surface, mainly because residual systematic camera calibration errors propagate onto the reconstructed earth surface. However, the choice of a specific image distortion model strongly depends on the deployed camera, but also on the purpose of the flight mission, e.g. parameters should be as distinct as possible if camera calibration is the main purpose. A very popular, *physically motivated* image distortion model was

introduced by Brown (1971). Following the definition given in Förstner and Wrobel (2016), the image distortion can thereby be modeled, by substituting the image coordinates $\bar{x}^c_{[i][t]}, \bar{y}^c_{[i][t]}$ in (3.20) and (3.21) according to

$$\begin{aligned}\bar{x}' = x' &+ x'(K'_{1[c]}r'^2 + K'_{2[c]}r'^4 + K'_{3[c]}r'^6 + \ldots) + \\ &+ (P'_{1[c]}(r'^2 + 2x'^2) + 2P'_{2[c]}x'y')(1 + P'_{3[c]}r'^2 + \ldots)\end{aligned} \tag{3.22}$$

$$\begin{aligned}\bar{y}' = y' &+ y'(K'_{1[c]}r'^2 + K'_{2[c]}r'^4 + K'_{3[c]}r'^6 + \ldots) + \\ &+ (2P'_{1[c]}x'y' + P'_{2[c]}(r'^2 + 2y'^2))(1 + P'_{3[c]}r'^2 + \ldots)\end{aligned} \tag{3.23}$$

with

$\bar{x}', \bar{y}'$ ... reduced undistorted image coordinates:

$$\bar{x}' = \bar{x}^c_{[i][t]} - x^c_{0[c]}, \qquad \bar{y}' = \bar{y}^c_{[i][t]} - y^c_{0[c]} \tag{3.24}$$

x', y' ... reduced distorted image coordinates:

$$x' = x^c_{[i][t]} - x^c_{0[c]}, \qquad y' = y^c_{[i][t]} - y^c_{0[c]} \tag{3.25}$$

r' ... radial distance defined as $r' = \sqrt{x'^2 + y'^2}$
$K'_{n[c]}$ ... n-th radial distortion coefficient of camera $[c]$
$P'_{n[c]}$ ... n-th tangential distortion coefficient of camera $[c]$

The most popular *phenomenological motivated* alternatives to the *Brown model* are the *Ebner model* (12 parameters) (Ebner, 1976) and the *Gruen model* (44 parameters) (Grün, 1986). More about the choice of an appropriate camera calibration model can be found in (Förstner and Wrobel, 2016, p. 684) and Blázquez and Colomina (2010).

3.1.4 Trajectory correction parameters

The trajectory of the aircraft is assumed to be estimated in advance by the integration of GNSS and INS measurements in a Kalman filter (Kalman, 1960). As a result, the original position and orientation estimates are given, together with their precisions, as a function of the flight time t:

Original position	Original orientation
$g^e_{x0}(t)$... x-coordinate	$\phi_0(t)$... roll angle
$g^e_{y0}(t)$... y-coordinate	$\theta_0(t)$... pitch angle
$g^e_{z0}(t)$... z-coordinate	$\psi_0(t)$... yaw angle

The original flight trajectory forms the basis for the direct georeference of lidar strips (section 3.1) and aerial images (section 3.14). However, Skaloud et al. (2010) pointed out that GNSS and INS measurements are strongly affected by external influences (e.g. satellite constellation, flight maneuvers) and consequently their accuracy can not be assumed to be constant in time. This in turn leads to *time-dependent errors* of the estimated trajectory, which should be corrected by adjustment. In this

work, it is proposed to correct each of the six trajectory elements, individually for each lidar/image strip $[s]$, by a correction function $\Delta(\cdot)_{[s]}(t)$. Additionally, three datum correction parameters Δg^e_x, Δg^e_y, Δg^e_z are applied to correct for a global shift of the whole block:

Corrected position	**Corrected orientation**
$g^e_x(t) = g^e_{x0}(t) + \Delta g^e_{x[s]}(t) + \Delta g^e_x$	$\phi(t) = \phi_0(t) + \Delta\phi_{[s]}(t)$
$g^e_y(t) = g^e_{y0}(t) + \Delta g^e_{y[s]}(t) + \Delta g^e_y$	$\theta(t) = \theta_0(t) + \Delta\theta_{[s]}(t)$
$g^e_z(t) = g^e_{z0}(t) + \Delta g^e_{z[s]}(t) + \Delta g^e_z$	$\psi(t) = \psi_0(t) + \Delta\psi_{[s]}(t)$

whereby we assume to have in the hybrid adjustment later on a set $\mathcal{S}$ of S strips:

$$s \in \mathcal{S} = \{1, \ldots, s, \ldots, S\}$$

Depending on the systematic errors of the original flight trajectory, four different correction models (cf. Figure 3.6) for the strip wise correction functions $\Delta(\cdot)_{[s]}(t)$ can be chosen:

- **Bias Trajectory Correction Model (BTCM)**
- **Linear Trajectory Correction Model (LTCM)**
- **Quadratic Trajectory Correction Model (QTCM)**
- **Spline Trajectory Correction Model (STCM)**

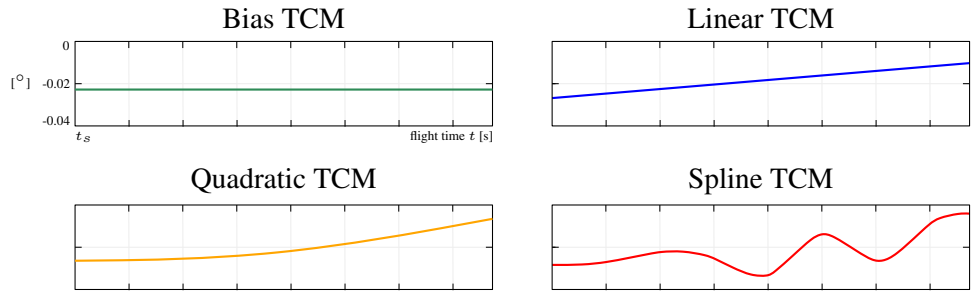

Figure 3.6: Schematic comparison of the different trajectory correction models for a single strip and a single trajectory element, e.g. the roll angle correction.

The simplest model is the BTCM. It corrects a bias (by 0-degree polynomials) for each of the six trajectory elements, individually for each strip. The LTCM and QTCM additionally can mitigate the effect of linear and quadratic INS drifts (by 1- or 2-degree polynomials), respectively. However, in practice such drifts are mostly already corrected to a large extent in the Kalman filter by other measurements, especially GNSS measurements (Colomina, 2015). The correction models for BTCM, LTCM and QTCM are for a single strip $[s]$, e.g. for the roll angle correction:

$$\text{BTCM}: \quad \Delta\phi_{[s]} = a_{0[s]} \tag{3.26}$$

$$\text{LTCM}: \quad \Delta\phi_{[s]}(t) = a_{0[s]} + a_{1[s]}(t - t_{s[s]}) \tag{3.27}$$

$$\text{QTCM}: \quad \Delta\phi_{[s]}(t) = a_{0[s]} + a_{1[s]}(t - t_{s[s]}) + a_{2[s]}(t - t_{s[s]})^2 \tag{3.28}$$

where $t_{s[s]}$ is the starting time of the strip $[s]$ and t is the time stamp of the trajectory estimate. The correction of the remaining five trajectory elements is carried out in the same way. The coefficients $a_{0[s]}$, $a_{1[s]}$, and $a_{2[s]}$ are estimated by adjustment. That gives for a total number of S strips, $6S$ coefficients for the BTCM, $12S$ coefficients for the LTCM, and $18S$ coefficients for the QTCM.

3.1.4.1 The spline trajectory correction model

Due to its simplicity, the correction models described in the previous section are often insufficient, especially if a very high georeferencing accuracy is demanded, e.g. for deformation monitoring or modelling of complex objects like buildings or trees. For such cases, we propose the usage of natural cubic splines with constant segment length Δt in time domain for modelling these correction functions (Figure 3.7). This model choice is inevitably somewhat arbitrary, as the true pattern of the residual trajectory errors is unknown. However, using cubic splines has some justifiable grounds:

- The residual trajectory errors are expected to be smoothed in forward and backward direction after Kalman filtering. Due to their smoothness and high flexibility, cubic splines are an appropriate counterpart to the long-term components of these residual errors.
- In comparison with higher-degree polynomials, the risk of overfitting is relatively small for cubic splines. However, if a too small segment length Δt (e.g. 0.5 s) is chosen, overfitting may still occur.
- Due to their straightforward mathematical formulation, cubic splines can be easily incorporated (together with the appropriate constraints) into the functional model of an adjustment.

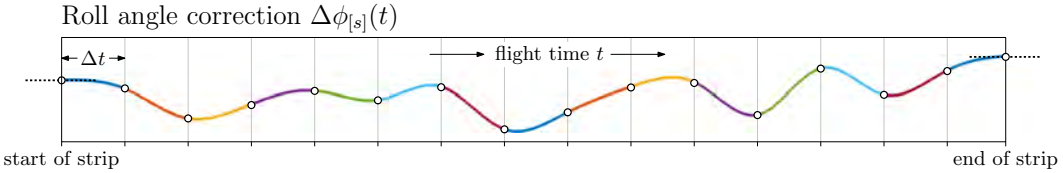

Figure 3.7: Example of roll angle correction $\Delta\phi_{[s]}(t)$ for a single flight strip $[s]$. The correction is modelled as natural cubic spline with constant segment length Δt. At the beginning and the end of a strip, the first and second derivatives are constrained to zero. The continuity and smoothness of the spline function are ensured by the C^0, C^1, and C^2 continuity constraints.

Correction model This section contains the equations required for the incorporation of the proposed correction model into the adjustment. It is emphasized that an individual correction function is estimated for each trajectory element and for each flight strip $[s]$. If we denote the start and end time of the s-th strip with $t_{s[s]}$ and $t_{e[s]}$ respectively, the total number of polynomial segments for each trajectory

element of this strip is defined by

$$n_{[s]} = \left\lceil \frac{t_{e[s]} - t_{s[s]}}{\Delta t} \right\rceil \tag{3.29}$$

where Δt is the segment length of a single polynomial in time domain. The k-th cubic polynomial ($k = 1, \ldots, n_{[s]}$) of the s-th strip is represented – e.g. for the roll angle correction – by

$$\begin{aligned} \Delta\phi_{[s][k]}(t) = \quad & a_{0[s][k]} \\ & + a_{1[s][k]} \left(t - t_{s[s][k]}\right) \\ & + a_{2[s][k]} \left(t - t_{s[s][k]}\right)^2 \\ & + a_{3[s][k]} \left(t - t_{s[s][k]}\right)^3 \end{aligned} \tag{3.30}$$

whereby the start time of the polynomial is

$$t_{s[s][k]} = t_{s[s]} + (k-1) \cdot \Delta t \tag{3.31}$$

and the polynomial is defined for the time interval

$$\begin{aligned} &\text{for } \; k = 1, \ldots, n_{[s]} - 1 \quad && \rightarrow t \in [t_{s[s][k]}, t_{s[s][k+1]}] \\ &\text{for } \; k = n_{[s]} && \rightarrow t \in [t_{s[s][k]}, t_{e[s]}] \end{aligned}$$

However, if the last polynomial is very short, e.g. smaller than $\Delta t/2$, it should be merged with the previous one.

The coefficients $a_{0[s][k]}, a_{1[s][k]}, a_{2[s][k]}$, and $a_{3[s][k]}$ of each polynomial (eq. 3.30) are estimated by adjustment; a summary can be found in Table 3.3.

Constraints To ensure that the splines are continuous and smooth at the junctions of the polynomials, the following constraints have to be incorporated for the inner knots ($k = 1, \ldots, n_{[s]} - 1$) into the adjustment:

- the $\mathbf{C}^0$ **continuity** expresses that the polynomials are continuous at the internal knots:

$$\Delta\phi_{[s][k]}(t_{s[s][k+1]}) = \Delta\phi_{[s][k+1]}(t_{s[s][k+1]}) \tag{3.32}$$

- the $\mathbf{C}^1$ **continuity** expresses that the first derivative of the polynomials is continuous at the internal knots:

$$\Delta\phi'_{[s][k]}(t_{s[s][k+1]}) = \Delta\phi'_{[s][k+1]}(t_{s[s][k+1]}) \tag{3.33}$$

- the $\mathbf{C}^2$ **continuity** expresses that the second derivative of the polynomials is continuous at the internal knots:

$$\Delta\phi''_{[s][k]}(t_{s[s][k+1]}) = \Delta\phi''_{[s][k+1]}(t_{s[s][k+1]}) \tag{3.34}$$

The required first and second derivatives of eq. (3.30) are

$$\begin{aligned}\Delta\phi'_{[s][k]}(t) = \quad & a_{1[s][k]} \\ & + 2\,a_{2[s][k]}\,(t - t_{s[s][k]}) \\ & + 3\,a_{3[s][k]}\,(t - t_{s[s][k]})^2\end{aligned} \tag{3.35}$$

$$\begin{aligned}\Delta\phi''_{[s][k]}(t) = \quad & 2\,a_{2[s][k]} \\ & + 6\,a_{3[s][k]}\,(t - t_{s[s][k]})\end{aligned} \tag{3.36}$$

Additionally, boundary conditions are introduced to avoid steep slopes of the correction function at the beginning and at the end of each flight strip (Figure 3.7). This is accomplished by setting the first and second derivatives to zero at the beginning ($t = t_{s[s]} = t_{s[s][1]}$) of each strip

$$\Delta\phi'_{[s][1]}(t_{s[s]}) = 0 \quad \Rightarrow a_{1[s][1]} = 0 \tag{3.37}$$

$$\Delta\phi''_{[s][1]}(t_{s[s]}) = 0 \quad \Rightarrow a_{2[s][1]} = 0 \tag{3.38}$$

and at the end ($t = t_{e[s]}$) of each strip

$$\Delta\phi'_{[s][n_{[s]}]}(t_{e[s]}) = 0 \tag{3.39}$$

$$\Delta\phi''_{[s][n_{[s]}]}(t_{e[s]}) = 0 \tag{3.40}$$

The equations (3.32) – (3.34) and (3.37) – (3.40) are incorporated as constraints into the adjustment.

Fictional observations If a single strip is not fully overlapping with other strips, some polynomials can not be estimated due to lack of correspondences. As a consequence the equation system becomes singular. To overcome this problem, fictional observations (sometimes also denoted as zero-observations) are added for the 0-degree polynomial coefficients $a_{0[s][k]}$ to the equation system. They have the form

$$a_{0[s][k]} = 0 + v_{[s][k]} \tag{3.41}$$

where $v_{[s][k]}$ denotes the residual of the observation. As *a priori* precision of these observations $\sigma_{a_{0[s][k]}}$ the trajectory precision estimates from the Kalman filter should be used. If this information is not available, the measurement precisions, as declared by the manufacturers, can be used alternatively. Besides removing the rank deficiency, these observations have also other important effects: they avoid a high unmotivated oscillation of the trajectory correction functions and ensure that they converge steadily to zero in areas without redundancy, i.e. in areas without overlap. The objective function for these additional observations is:

$$\Omega_{\mathrm{STCM}} = \operatorname{argmin}\left\{\sum_{s=1}^{S}\sum_{k=1}^{n_{[s]}}(w_{[s][k]}\,a^2_{0[s][k]})\right\} \tag{3.42}$$

where S denotes the total number of strips, and the weight $w_{[s][k]}$ is defined by

$$w_{[s][k]} = \frac{1}{\sigma^2_{a_{0[s][k]}}} \tag{3.43}$$

It should be noted that no fictional observations are needed for the remaining coefficients $a_{1[s][k]}$, $a_{2[s][k]}$, and $a_{3[s][k]}$, as their determination is ensured by the constraints described in the previous section. We will discuss the usage of fictional observations for parameters in general in section 3.3.

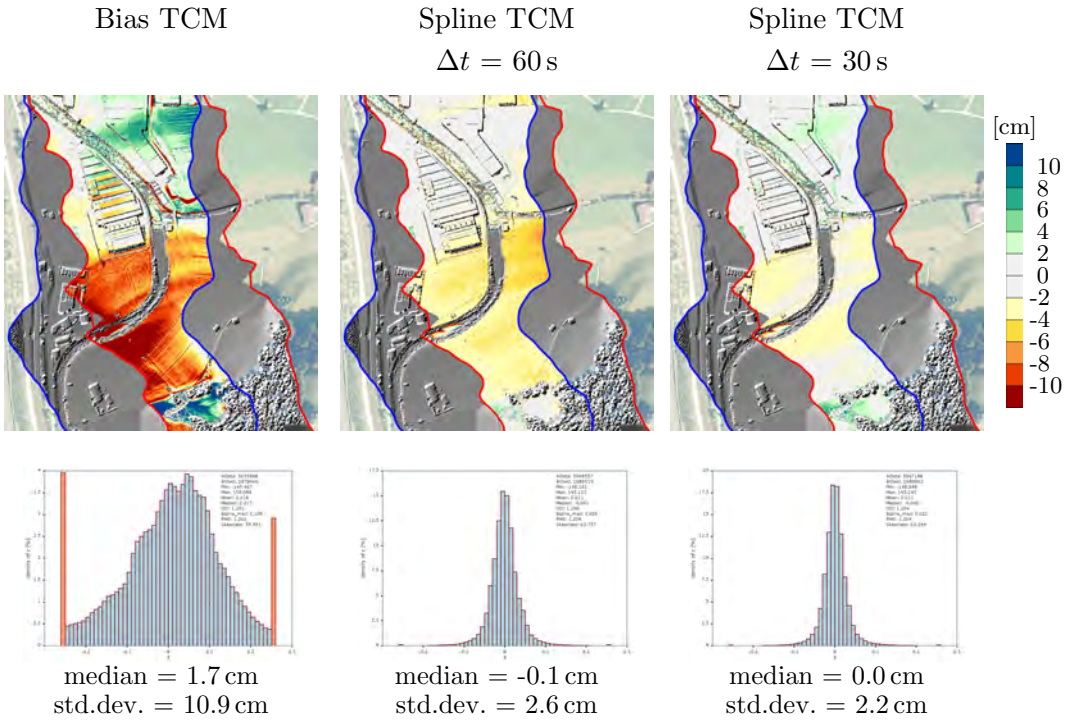

Figure 3.8: Comparison between Bias TCM (left) and Spline TCM with segment lengths Δt of 60 s (middle) and 30 s (right). Top: height differences within the overlap area of two lidar strips (red and blue boundaries). Bottom: Histograms of height differences.

Possible problems Some problems may arise by using the *STCM*:

- **Absolute deformation of the block**: Due to the high flexibility of the trajectory correction model, systematic discrepancies between overlapping strips can almost completely be eliminated, especially if a small segment length Δt is used. However, an absolute deformation of the whole lidar and image block might occur if Δt is too small (*model overfitting*), as in such cases the estimated trajectory correction parameters compensate not only trajectory errors, but also the effect of other error sources (e.g. a wrongly calibrated laser scanner). Thus, an appropriate choice of Δt is very important and will be discussed on the basis of real data in section 4.3. Alternatively, block deformations can also be avoided – almost independent from the actual choice of Δt – by using

a large number of ground control points that are homogeneously distributed over the whole block. We will also show in section 4.4 that the incorporation of aerial images strongly mitigates the oscillation of the spline correction functions.

- **Local effect of ground control points**: Usually, single ground control points can be used to correct the datum of the whole block. However, by using a time-dependent trajectory correction model only, such widely isolated points can have a local effect only, i.e. the datum is corrected in the vicinity of these points only. This problem can be avoided by using the datum correction parameters Δg_x^e, Δg_y^e, Δg_z^e, which have been introduced at the beginning of this section. As they correct a global shift of the whole block, e.g. due to systematic GNSS errors, the strip wise trajectory corrections correct predominately the residual local error patterns. Alternatively this problem can also be avoided – since it is closely related to the previous one – by using a dense network of ground control points.

- **Determinability of trajectory correction functions**: For a reliable estimation of the time-dependent trajectory correction functions, a dense and homogeneous distribution of the correspondences is needed. Furthermore, the determinability of the correction functions depends on the terrain geometry and can therefore not be guaranteed in any case, e.g. over completely featureless, flat terrain; however, practical experience has shown that this is a rather theoretical problem.

3.1.5 Summary

Table 3.3 gives a summary of the parameters that *can* be estimated by adjustment. It should be noted that depending on the assembly of the sensors, the flight configuration, and the terrain geometry, some of these parameters may be completely correlated and therefore not estimable. Besides that, *model overfitting* should be avoided, i.e. only the parameters that are needed for modeling systematic errors should be estimated. The parameters introduced in the previous sections can be categorized as follows:

1. **Laser scanner calibration parameters**

   The **sensor calibration** parameters correct for systematic errors of the scanner's range and angle measurements by estimating an offset (bias) and scale parameter for each polar coordinate. These parameters might be omitted if the scanner is already well-calibrated. An exception to this are flights with long ranges and almost horizontal angle measurements. In such cases, the atmospheric refraction has a not negligible effect on the range and angle measurements. As the sensor calibration parameters are formulated in a very general way, they can also be applied to partly compensate these effects.

   The **mounting calibration** parameters are formed by three angles (*misalignment*), describing the rotation of the scanner w.r.t. the INS, and a 3D vector (*lever-arm*) describing the positional offset between GNSS antenna and the origin of the scanner. The estimation of the misalignment angles is recommended in any case, as erroneous angles can cause due to the leverage effect

Parameters				
	category	name		#
laser scanner	**sensor calibration**	range offset (bias)	$\Delta\rho_{[l]}$	L
		range scale	$\varepsilon_{\rho[l]}$	L
		angle offsets (biases)	$\Delta\alpha_{[l]}, \Delta\beta_{[l]}$	$2L$
		angle scales	$\varepsilon_{\alpha[l]}, \varepsilon_{\beta[l]}$	$2L$
	mounting calibration	misalignment angles	$\alpha_{1[l]}, \alpha_{2[l]}, \alpha_{3[l]}$	$3L$
		lever-arm components	$a^i_{x[l]}, a^i_{y[l]}, a^i_{z[l]}$	$3L$
cameras	**interior orientation**	2D coordinates of principal point	$x^c_{0[c]}, y^c_{0[c]}$	$2C$
		principal distance	$c^c_{[c]}$	C
		image distortion parameters	$K'_{n[c]}, P'_{n[c]}$	$C(n_r + n_t)$
	mounting calibration	misalignment angles	$\alpha_{1[c]}, \alpha_{2[c]}, \alpha_{3[c]}$	$3C$
		lever-arm components	$a^i_{x[c]}, a^i_{y[c]}, a^i_{z[c]}$	$3C$
images	**coupled images**	correction of 3D coordinates of projection centers	$\Delta X^e_{0[i]}, \Delta Y^e_{0[i]}, \Delta Z^e_{0[i]}$	$3I$
		correction of rotation angles	$\Delta\omega_{[i]}, \Delta\varphi_{[i]}, \Delta\kappa_{[i]}$	$3I$
	loose images	3D coordinates of projection centers	$X^e_{0[i]}, Y^e_{0[i]}, Z^e_{0[i]}$	$3I$
		rotation angles	$\omega_{[i]}, \varphi_{[i]}, \kappa_{[i]}$	$3I$
	tie points	3D coordinates of image tie points	$X^e_{[t]}, Y^e_{[t]}, Z^e_{[t]}$	$3T$
trajectory	**position**	x correction coefficients	$\Delta g^e_{x[s]}$	S
		y correction coefficients	$\Delta g^e_{y[s]}$	S
		z correction coefficients	$\Delta g^e_{z[s]}$	S
	rotation	roll correction coefficients	$\Delta\phi_{[s]}$	S
		pitch correction coefficients	$\Delta\theta_{[s]}$	S
		yaw correction coefficients	$\Delta\psi_{[s]}$	S
	datum	datum correction parameters	$\Delta g^e_x, \Delta g^e_y, \Delta g^e_z$	3

for $s \in \mathcal{S} = \{1, \ldots, s, \ldots, S\}, l \in \mathcal{L} = \{1, \ldots, l, \ldots, L\}, c \in \mathcal{C} = \{1, \ldots, c, \ldots, C\}$
$i \in \mathcal{I} = \{1, \ldots, i, \ldots, I\}, t \in \mathcal{T} = \{1, \ldots, t, \ldots, T\}$

Table 3.3: Overview of the parameters estimated by adjustment. S = no. of strips, L = no. of laser scanners, C = no. of cameras, I = no. of images, n_r = no. of radial distortion coefficients, n_t = no. of tangential distortion coefficients, T = no. of image tie points. The number of trajectory correction parameters is given for the *Bias Trajectory Correction Model*.

very large point displacements on the ground. This is not necessarily true for the lever-arm, where errors are propagated 1:1 to the ground. Thus, a re-estimation of the lever-arm components is only recommended if terrestrial measurements of the lever-arm are not available or inaccurate.

2. **Camera calibration parameters**

   The parameters of the **interior orientation** include the principal point, the principal length, and the image distortion parameters. If these parameters are already known in advance, or if *undistorted images* are used, the estimation of some of these parameters might be omitted.

   The **mounting calibration** parameters are analogous to the laser scanner case described above. It is emphasized that for the estimation of the mounting calibration parameters the exposure times of the images must be known. Unfortunately in practice, in contrast to lidar measurements, the exposure times are often not recorded. Such images can not be coupled to the flight trajectory and have to be treated as *loose images* in the adjustment (see next point).

3. **Image parameters**

   We differentiate between coupled and loose images.

   Coupled images are coupled to the flight trajectory, i.e. the exterior orientation of these images can be formulated through the direct georeferencing equation as function of the flight trajectory and the camera's mounting calibration (cf. section 3.14). However, it might be necessary to further correct the image's position and rotation obtained this way, e.g. if the time stamps of the images are inaccurate or in case the residuals show systematic patterns. Thus, the elements of the exterior orientation can be corrected individually for each image by three coordinate correction parameters and three angle correction parameters. These parameters must be observed through fictional observations to keep the coupling to the trajectory intact.

   Loose images are images for which the relation to the flight trajectory can not be established, e.g. images that have been collected without GNSS/INS system or images without recorded time stamps. In such cases the elements of the exterior orientation are *directly* estimated by adjustment. Some of the advantages of the hybrid adjustment get thereby lost, e.g. the estimation of the trajectory corrections is far less supported by loose images than by coupled images.

   Finally, the image **tie points** form the numerically largest parameter group in the hybrid adjustment. For each tie point the 3 coordinates are estimated.

4. **Trajectory correction parameters**

   The flight trajectory estimated in advance from GNSS and INS measurements is corrected individually for each strip and trajectory element, as well as globally for the whole block.

   For the **strip wise correction** of the trajectory among four different Trajectory Correction Models (TCM) can be chosen:

   - **Bias TCM** → correction by 0-degree polynomials

- **Linear TCM** → correction by 1-degree polynomials
- **Quadratic TCM** → correction by 2-degree polynomials
- **Spline TCM** → correction by natural cubic splines

A suitable correction model needs to be chosen individually for each flight campaign depending on the systematic errors of the original flight trajectory.

The **block wise correction** of the trajectory is applied to correct for a global shift of the whole block, e.g. due to systematic GNSS errors. Such a shift can only be estimated by introducing ground-truth data into the adjustment.

3.2 Correspondences

We have discussed the adjustment's parameter model in the previous section. To estimate these parameters and improve the georeference of the lidar strips and the aerial images at once, various types of correspondences are used. These correspondences are established between the following input data types (cf. Figure 1.1 and 3.1):

- **lidar strips** (**STR**): given by the measurements of the scanner, the trajectory of the aircraft, and priors for the mounting calibration.
- **aerial images** (**IMG**): imagery, either coupled to the trajectory by a time stamp and the mounting calibration (*coupled images*), or with priors for the exterior orientation (*loose images*).
- **control point clouds** (**CPC**): datum-defining point clouds with known coordinates in object space (e-system), e.g. point clouds from Terrestrial Laser Scanning (TLS) or a DEM from an earlier flight campaign.
- **ground control points** (**GCP**): datum-defining points with known coordinates in object space (e-system), e.g. measured by GNSS or total stations, and image space (c-system).

Five different correspondence types can be established between these data inputs; a summary is given in Figure 3.1, 3.9, and Table 3.4. As can be seen, two correspondence types can be associated to the strip adjustment of lidar strips and the bundle adjustment of aerial images respectively, whereas the fifth type is newly introduced in this work to establish a link between the laser scans and the aerial images. The various correspondences serve to define the observations used for parameter estimation in the hybrid adjustment.

Three distinct steps are needed to establish the correspondences in object space: the *selection*, the *matching*, and the *rejection* step, cf. section 2.1. For each of these steps different variants will be described in the sections 3.2.1–3.2.3. Thereby, a special focus lies on the large amounts of data, as they typically occur in topographic mapping. An appropriate error metric for the minimization of discrepancies between overlapping point clouds will be proposed in section 3.2.4. Finally, in section 3.2.5, the various correspondence types will be described in detail.

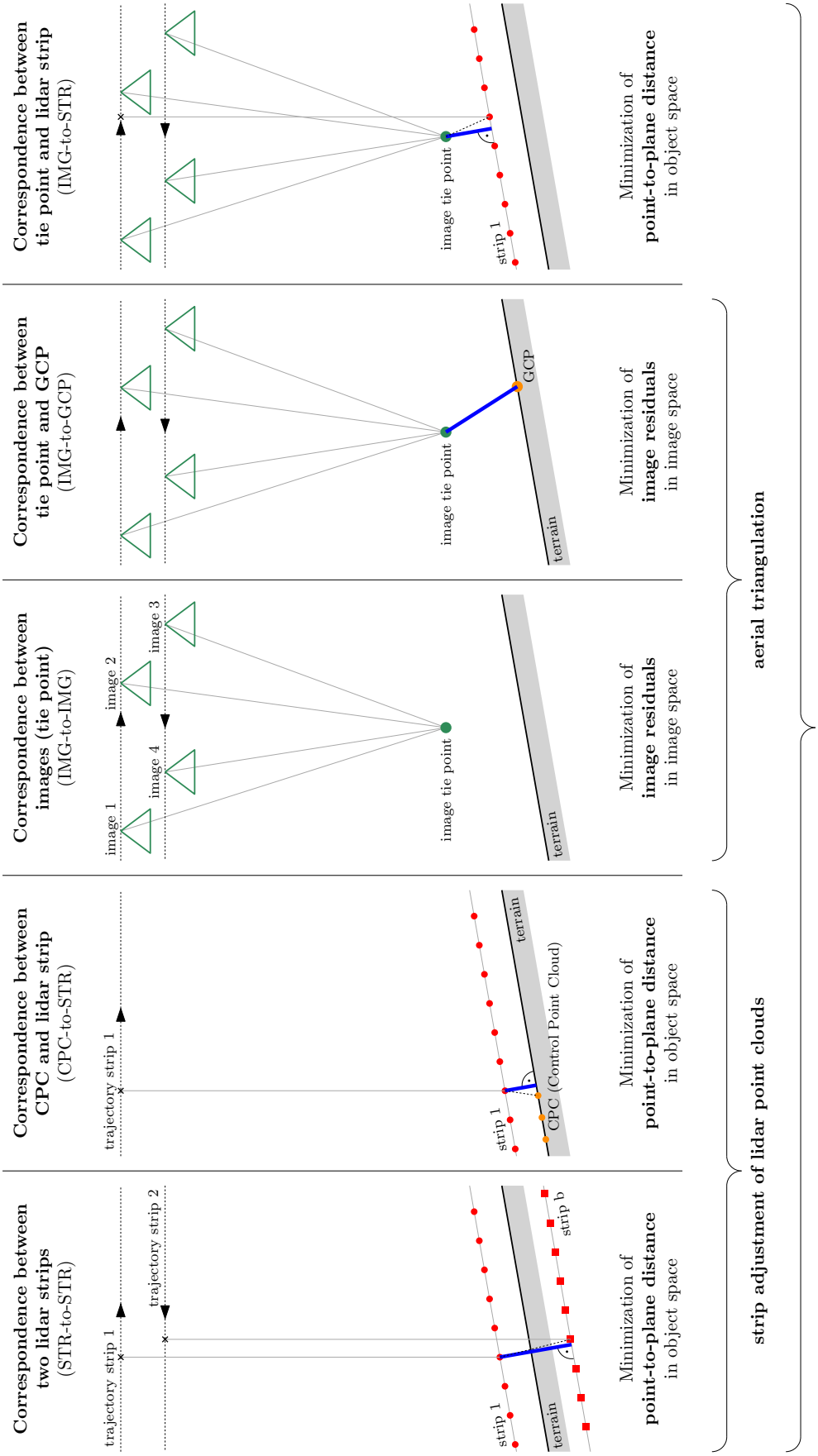

Figure 3.9: Five different types of correspondences are used in the hybrid adjustment of lidar strips and aerial images.

Correspondences			
type	correspondences between	where	section
STR-to-STR	lidar strip & lidar strip	object space	3.2.5.1
CPC-to-STR	control point cloud & lidar strip	object space	3.2.5.2
IMG-to-STR	image points & lidar strip	object space	3.2.5.3
IMG-to-IMG	image points & image points	image space	3.2.5.4
IMG-to-GCP	image points & ground control points	image space	3.2.5.4

Table 3.4: Overview of the correspondences established in the hybrid adjustment.

3.2.1 Selection strategies

The correspondence selection strategies presented in this section refer to the *selection* step of the ICP framework discussed in section 2.1. It is proposed to select the correspondences on a point basis, the main reasons for this are: the highest possible resolution level of the data is exploited, no time-consuming pre-processing of the data is required (in contrast to correspondences which are found by segmentation and/or interpolation), and no restrictions are imposed on the object space (e.g. the presence of rooftops or horizontal fields).

In the original version of the ICP algorithm *each* point is selected as correspondence. However, for lidar data this is not feasible. This is particularly true for strip adjustments of a complete data acquisition campaign, in which hundreds of strip pairs have to be processed simultaneously. Thus, compared to the full amount of available data (up to several million points), only a comparatively small number (a few thousands) of points can be selected within the overlap area of each strip pair. Since the selected subset heavily affects the final alignment accuracy, the selection of relevant points is crucial.

We consider four different strategies for the selection of correspondences within the overlap area of two point clouds. The main difference between these strategies is the information used as input for the point selection, cf. Table 3.5. It is noted, that these strategies can be applied to all correspondences established in object space, namely STR-to-STR correspondences, CPC-to-STR correspondences, and IMG-to-STR correspondences.

The four selection strategies, sorted by increasing computational complexity, are:

- **Random Sampling (RS)** This is the fastest strategy, because points are simply selected randomly, without considering the coordinates or the normal vectors of the points. For airborne lidar point clouds, in which the point density is usually nearly constant (in contrast to terrestrial lidar point clouds), this option can be considered as an approximation of *Uniform Sampling*.

- **Uniform Sampling (US)** The aim of this strategy is to select points in object space as uniformly as possible. This leads to a homogeneous distribution of the selected points, where regions of equal area are equally weighted within the adjustment. On the contrary, if a normal direction is predominating (e.g. flat terrain), many redundant points with approximately parallel normal vectors, which do not contribute significantly to the parameter estimation, are selected. This option can be implemented by dividing the overlap area into a voxel

structure and selecting the closest point to each voxel center. Consequently, the edge length of a single voxel can be interpreted as the mean sampling distance along each coordinate direction.

- **Normal Space Sampling (NSS)** The aim of this strategy is to select points such that the distribution of their normals in angular space is as uniform as possible (Rusinkiewicz and Levoy, 2001). For this the angular space (slope vs. aspect) is divided into classes (e.g. 2.5°x10°), and points are randomly sampled within these classes. This strategy does not consider the position of the points.
- **Maximum Leverage Sampling (MLS)** This strategy selects those points, which are best suited for the estimation of the parameters. For this, the effect of each point on the parameter estimation, i.e. its leverage, is considered. The points with the maximum leverage (= the lowest redundancy) are selected. This strategy considers the coordinates and the normal vectors of the points. This algorithm is described in detail in section 3.2.1.1.

	RS	**US**	**NSS**	**MLS**
coordinates of points	no	yes	no	yes
normal vectors of points	no	no	yes	yes

Table 3.5: Information used by the selection strategies.

Sometimes it can be advantageous to combine the presented strategies. For example, in case of high-density lidar data it might be useful to first select points with the *Uniform Sampling* strategy and further select a subset from these with the *Maximum Leverage Sampling* strategy, cf. Figure 3.12.

Figure 3.10 compares the selection strategies on the basis of a (in terms of orientation) rather difficult dataset. For this, a synthetic point cloud made of 10201 points (=101^2) was generated by sampling a plane with two orthogonal ditches. For each strategy 10% of the original points were selected. It is noted that only the two ditches can constrain all transformation parameters (rotation and shift) at its finest level. As RS and US do not consider the orientation of the normal vectors, many redundant points are selected on the flat terrain and only a few points are selected within the ditches. As a consequence, both strategies are only recommended for terrain with steady height variations (e.g. urban area, hilly or mountainous terrain). However, NSS considers the normal vectors and thus a sufficient number of points is selected within the ditch. MLS additionally evaluates the coordinates of the points in order to estimate the leverage of each point on the parameter estimation. As a result, points are primarily selected in the ditch and towards the edges of the overlap area.

3.2.1.1 Maximum Leverage Sampling

The quality of the parameter estimation heavily depends on the selected subset of points. For example, if too many correspondences come from featureless regions, the adjustment can fail to converge because of lack of constraints. Herein a new method

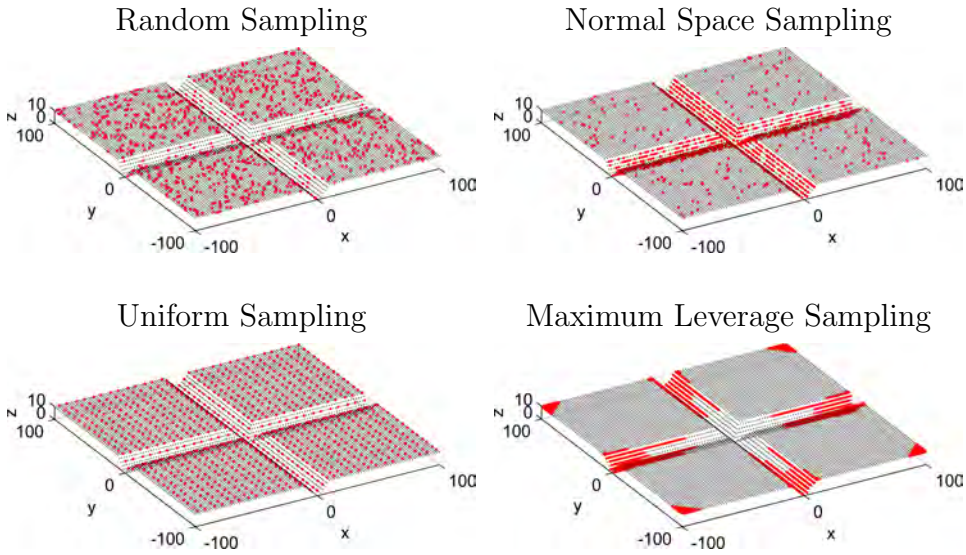

Figure 3.10: Comparison of different selection strategies. With each strategy 10% of points are selected. An animation of this scene can be found at https://youtu.be/ZTGRw3C73PQ.

is proposed for the selection of points which minimizes the uncertainty of the estimated transformation parameters, i.e. those points are selected which constrain the transformation the most. As a consequence, a very small number of correspondences is sufficient for the alignment of overlapping lidar strips. This is of particular advantage when hundreds of strip pairs have to be processed simultaneously in a strip adjustment.

We start from some basic formulas of the Gauß-Markow adjustment model. Then we derive the hat matrix H on which the presented method is based on, including some brief explanations of its properties. Subsequently, an example of the hat matrix for a specific case (point-to-plane error metric and rigid body transformation model) is given. Finally, the point selection algorithm is presented.

The hat matrix H We consider a system of linear equations given by

$$\mathbf{l} = A\mathbf{x} \tag{3.44}$$

where the u unknown transformation parameters $\mathbf{x}$ are linked with the n original observations $\mathbf{l}$ by the full-column rank n-by-u coefficient matrix A. This overdetermined equation system ($n > u$) is solved by introducing n residuals $\mathbf{v}$ for the observations $\mathbf{l}$

$$\mathbf{l} + \mathbf{v} = A\hat{\mathbf{x}} \tag{3.45}$$

and minimizing the least squares objective function $E = \mathbf{v}^T\mathbf{v}$. By substituting $\mathbf{v}$ with $A\hat{\mathbf{x}} - \mathbf{l}$ and setting the partial derivative $\partial E/\partial\hat{\mathbf{x}} = 0$, the estimates for the parameters $\hat{\mathbf{x}}$ are determined by

$$\hat{\mathbf{x}} = (A^TA)^{-1}A^T\mathbf{l} \tag{3.46}$$

The unknown $\hat{\sigma}_0$ can be estimated by

$$\hat{\sigma}_0 = \sqrt{\frac{\mathbf{v}^T\mathbf{v}}{n-u}} \tag{3.47}$$

The covariance matrix $\Sigma_{\hat{\mathbf{x}}\hat{\mathbf{x}}}$ of the estimated unknown parameters $\hat{\mathbf{x}}$ is then given by

$$\Sigma_{\hat{\mathbf{x}}\hat{\mathbf{x}}} = \hat{\sigma}_0\, Q_{\hat{\mathbf{x}}\hat{\mathbf{x}}} \tag{3.48}$$

$$Q_{\hat{\mathbf{x}}\hat{\mathbf{x}}} = (A^T A)^{-1} \tag{3.49}$$

If we write $\hat{\mathbf{l}} = \mathbf{l} + \mathbf{v}$ for the estimated observations, (3.45) can be rewritten together with (3.46) as

$$\hat{\mathbf{l}} = A(A^T A)^{-1} A^T \mathbf{l} \tag{3.50}$$

To emphasize the fact that each $\hat{l}_i$ is a linear combination of the original observations $\mathbf{l}$, (3.50) can be written as

$$\hat{\mathbf{l}} = H\mathbf{l} \tag{3.51}$$

with

$$H = A(A^T A)^{-1} A^T \tag{3.52}$$

The n-by-n matrix H is known as the hat matrix, as it "puts a hat on $\mathbf{l}$". On the one hand H is a projection matrix, as it projects $\mathbf{l}$ into $\hat{\mathbf{l}}$. On the other hand H describes the amount of leverage or influence each observed value in $\mathbf{l}$ has on each fitted value in $\hat{\mathbf{l}}$. For instance, the i-th row of H contains the influence of the original observations $\mathbf{l}$ on the estimated observation $\hat{\mathbf{l}}$. More precise, the element h_{ij} can be interpreted as the influence of the observation l_j on $\hat{l}_i$. This value is independent from the actual value of l_j, since H depends (for uncorrelated and unweighted observations) only on A.

Due to these properties, the hat matrix can be used to identify observations which have a large influence on the parameter estimation. Such influential observations are defined according to Belsley et al. (2005) as:

> "An influential observation is one which, either individually or together with several other observations, has a demonstrably larger impact on the calculated values of various estimates (...) than is the case for most of the other observations."

For a specific observation l_i, the influence on the parameter estimates is most directly reflected in its leverage on the corresponding estimated observation $\hat{l}_i$ (Hoaglin and Welsch, 1978). This information is precisely contained in the corresponding diagonal element h_{ii} of the hat matrix. Thus, we focus our analysis on the diagonal elements of H, the so called leverages. They can be directly computed by

$$h_{ii} = \mathbf{a}_i (A^T A)^{-1} \mathbf{a}_i^T \tag{3.53}$$

where $\mathbf{a}_i$ denotes the i-th row of A. This way the memory-intensive computation of the off diagonal elements of H can be avoided.

The leverages have two important properties. According to Belsley et al. (2005), for the leverages h_{ii} it holds that

$$0 \leq h_{ii} \leq 1 \tag{3.54}$$

Further, as a projection matrix, H is symmetric and idempotent ($H^2 = H$). The trace of an idempotent matrix is equal to its rank, i.e. $\text{trace}(H) = \text{rank}(H)$. From (3.52), it can be seen that $\text{rank}(H) = \text{rank}(A) = u$, and hence $\text{trace}(H) = u$, i.e.

$$\sum_{i=1}^{n} h_{ii} = u \tag{3.55}$$

where u denotes the number of parameters. The redundancy numbers, which are commonly used in adjustment theory, are linked to the leverages by

$$r_{ii} = 1 - h_{ii} \tag{3.56}$$

According to Förstner and Wrobel (2016), the redundancy number describes the contribution of a single observation to the overall redundancy $r = n - u$, i.e. $\sum_{i=1}^{n} r_{ii} = r$.

Side note on partial leverages The leverages discussed so far, assume that all parameters are of equal interest. However, an observation may be influential only for one or a few parameter. For instance, a point on horizontal terrain is especially important for the estimation of the vertical component of the translation vector, but at the same time it is entirely redundant for the estimation of its horizontal components. Thus, the influence of an observation on a single parameter may be of interest. It is given by the partial leverages.

The partial leverage $h_{j,i}$ describes the influence of the i-th observation on the estimation of the j-th parameter and is defined according to Chatterjee and Hadi (1986) as

$$h_{j,i} = \frac{v_{j,i}^2}{\mathbf{v}_j^T \mathbf{v}_j} \tag{3.57}$$

$$v_j = (I - H_{[j]})A_j \tag{3.58}$$

with

I	...	n-by-n identity matrix
$H_{[j]}$	...	hat matrix calculated by omitting the j-th column of A
A_j	...	j-th column of A
$v_{j,i}$	...	i-th element of v_j

As their name already implies, the partial leverages measure the contribution of an individual parameter j to the overall leverage of an observation

$$h_{ii} = \sum_{j=1}^{u} h_{j,i} \tag{3.59}$$

To be complete, it should be noted that in presence of a stochastic model for the observations $P = Q_{ll}^{-1}$ the hat matrix becomes

$$H = A(A^T P A)^{-1} A^T P \tag{3.60}$$

i.e. H depends now on A and P. If the observations are correlated, i.e. the weight matrix P is not a diagonal matrix, the leverages are not restricted to the range [0,1].

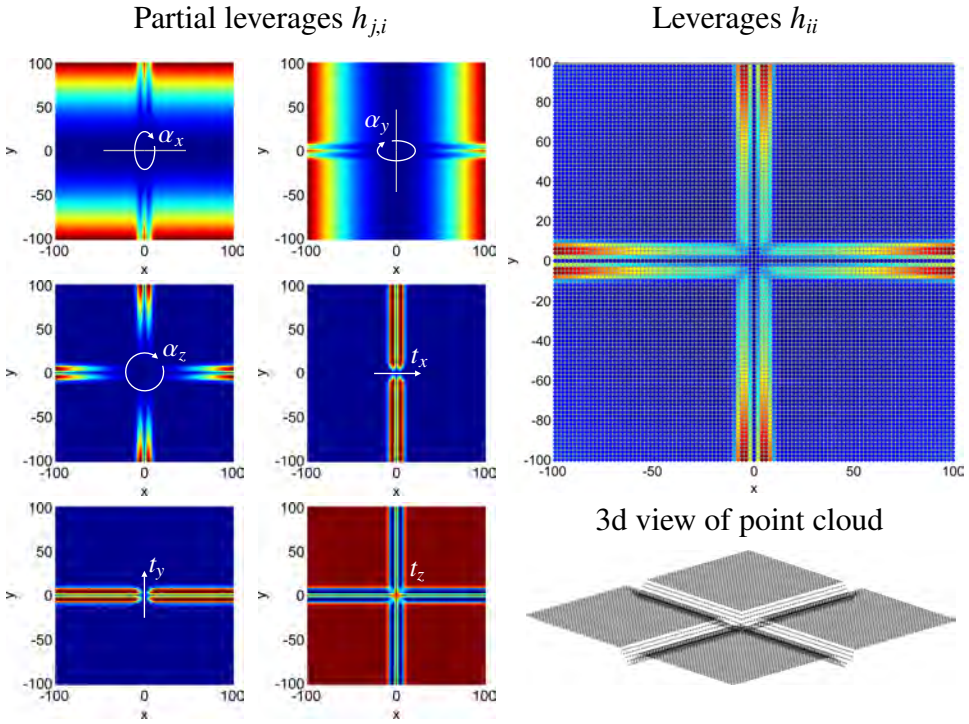

Figure 3.11: Partial leverages (left) and leverages (right) of the synthetic point cloud introduced in Figure 3.10. (red = high leverage, blue = low leverage). An animation of the point selection in this scene can be found at https://youtu.be/5Dbe4H5w8HQ.

Example: Calculation of leverages This example shows how to calculate the (partial) leverages depicted in Figure 3.11. It is noted, that the points selected by the MLS strategy are strongly influenced by the parameter model used for the transformation of the point clouds. In section 3.1 a comprehensive parameter model, including several calibration and correction parameter, was presented. However, for a better understanding, a simpler transformation model is chosen as parameter model in this example, namely the *rigid body transformation model*.

We can formulate the rigid body transformation T for a georeferenced point cloud $\mathbf{p}_i, i \in \mathcal{I} = \{1, \ldots, i, \ldots, I\}$, e.g. a directly georeferenced lidar strip, by

$$T(\mathbf{p}_i) = R\,\mathbf{p}_i + \mathbf{t} \tag{3.61}$$

where $\mathbf{t}$ denotes a 3-by-1 translation vector and R denotes a 3-by-3 orthogonal rotation matrix. Due to the good initial relative orientation of the point clouds, the rotation matrix R can be linearized substituting $\cos(\alpha) \approx 1$ and $\sin(\alpha) \approx \alpha$. Thus

(3.61) can be written as

$$T(\mathbf{p}_i) = \mathbf{p}_i + \mathbf{r} \times \mathbf{p}_i + \mathbf{t} \tag{3.62}$$

where $\mathbf{r} = (\alpha_x\, \alpha_y\, \alpha_z)^T$ is the vector containing the rotation angles around the x, y, and z axes, and $\mathbf{t} = (t_x\, t_y\, t_z)^T$. After a few algebraic steps, the n-by-6 coefficient matrix A can be found for the parameter vector $\mathbf{x}^T = (\mathbf{r}^T\, \mathbf{t}^T)$ as

$$A = \begin{bmatrix} (\mathbf{p}_1 \times \mathbf{n}_1)^T) & \mathbf{n}_1^T \\ (\mathbf{p}_2 \times \mathbf{n}_2)^T) & \mathbf{n}_2^T \\ \vdots & \vdots \\ (\mathbf{p}_I \times \mathbf{n}_I)^T) & \mathbf{n}_I^T \end{bmatrix} \tag{3.63}$$

As can be seen, each point $\mathbf{p}_i$ contributes one row in A, i.e. corresponds to one observation. It is clear, that not all points have an equal importance in the least squares adjustment. Thus, with (3.53) the leverage h_{ii} of each point $\mathbf{p}_i$ can be computed. This tells us how much influence a point $\mathbf{p}_i$ has on the estimation of the transformation parameters.

In Figure 3.11 the partial leverages and the leverages are visualized for the synthetic point cloud introduced in section 3.2.5.1. It can be clearly seen, that the partial leverages (left) identify those points which are most influential for the estimation of a single transformation parameter. For instance, for the rotation parameter α_x, points with larger distance from the rotation axis x are more influential than points next to it. The leverages (right), as the sum of the partial leverages, represent the influence of each point on the simultaneous estimation of all six transformation parameters. As expected, the points in the ditches and on the edges of the point cloud have the largest impact on the parameter estimation.

Summarizing, the diagonal elements of the hat matrix, called leverages, describe the influence of an observation on the parameter estimation. For uncorrelated and unweighted observations, the hat matrix can be calculated exclusively from the coefficient matrix A, see (3.52). Otherwise also the weight matrix P must be considered, see (3.60). Using the ICP methodological framework introduced in section 2.1, each point corresponds to one observation and therefore the leverages can be used to describe the influence of each point on the estimation of the transformation parameter. In the next section we show how points are selected on the basis of this information.

The selection algorithm Usually the leverages are used for the identification of potential blunders in the observation data. However, we use the leverages to identify those points which are best suited for the estimation of the transformation parameters, i.e. have the largest impact on the parameter estimation. In terms of redundancy numbers (3.56), the points with the lowest redundancy are selected. Table 3.6 provides a description of the algorithm.

The selection algorithm starts with the indices of all n points in $\mathbf{s}$, i.e. at the beginning all points are selected. Based upon this, the points with the lowest leverages are removed iteratively from $\mathbf{s}$ until m points are left. It is noted, that due to the correlation of the leverages (see (3.52)), they have to be recomputed in each iteration.

To speed up the algorithm, instead of removing only one single point, k points with the lowest leverages may be removed from s in each iteration. We found out that for a comparative small value of k (e.g. $k = 10$), this has a negligible effect on

Algorithm **Maximum leverage sampling**

Inputs:
  Point cloud: $\mathbb{P} = \{\mathbf{p}_1, \mathbf{p}_2, \ldots, \mathbf{p}_n\}$
  Normals: $\mathbb{N} = \{\mathbf{n}_1, \mathbf{n}_2, \ldots, \mathbf{n}_n\}$
  No. of points to select: m
Initialize vector with indices of all points: $\mathbf{s} = (1, 2, \ldots, n)^T$
Compute coefficient matrix A
while rows$(A) > m$ **do**
  $Q_{\hat{\mathbf{x}}\hat{\mathbf{x}}} = (A^T A)^{-1}$ (3.49)
  for $i = 1$ to rows(A) **do**
    $h_{ii} = \mathbf{a}_i Q_{\hat{\mathbf{x}}\hat{\mathbf{x}}}^{-1} \mathbf{a}_i^T$ (3.53)
  end for
  Find index j of point with lowest h_{ii}: $j = \text{find}(\min(h_{ii}))$
  Delete row $\mathbf{a}_j$ from A
  Delete j-th element from $\mathbf{s}$
end while
Return $\mathbf{s}$ with indices of selected points

Table 3.6: The Maximum Leverage Sampling algorithm.

the final selection of points, but leads to a substantial reduction in runtime.

3.2.2 Matching

In this step the correspondences are established, i.e. each point previously selected by one (or a combination) of the selection strategies presented in section 3.2.1 is paired to one point in the overlapping point cloud. This task refers to the *matching* step of the ICP framework discussed in section 2.1.

The simplest strategy is to match the selected points to their closest points (*nearest neighbours*) as proposed by Besl and McKay (1992). We found that for lidar and image data this is an adequate choice, mainly due to the good initial relative orientation and the high point density of lidar strips. The search for closest points can be realized efficiently using k-d trees.

Further matching methods are either computationally too expensive, e.g. normal shooting (Chen and Medioni, 1992), reverse calibration (Blais and Levine, 1995), or not necessary (Planitz et al., 2005) due to the good initial orientation of the point clouds, e.g. closest compatible point (Sharp et al., 2002). Thus, within this work, no other variants were investigated for this step.

3.2.3 Rejection of correspondences

The aim of this step is the a priori detection and rejection of false correspondences (outliers), as they may have a large effect on the result of the adjustment. This task refers to the *rejection* step of the ICP framework discussed in section 2.1. For the following considerations we assume that a set $\mathcal{P}$ of P correspondences, $p \in \mathcal{P} = \{1, \ldots, p, \ldots, P\}$, have been established in the *selection* and *matching* step.

The proposed correspondence rejection criteria are:

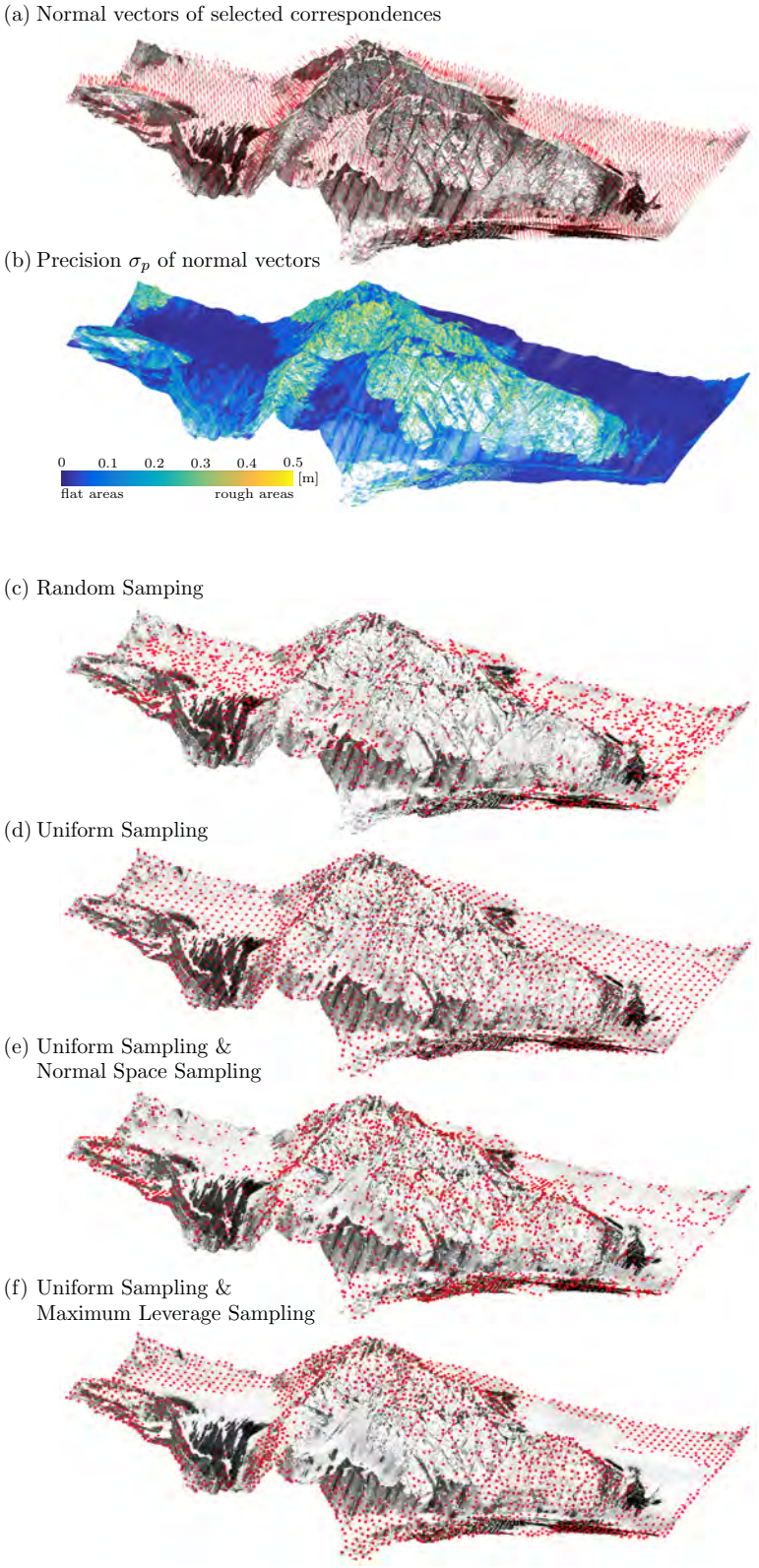

Figure 3.12: (a) and (b): Normal vectors of selected correspondences with their precision. It is recommended to establish correspondences in smooth areas only, thus all points with $\sigma_p \leq 0.2\,\mathrm{m}$ have been rejected here. (c) to (f): Selection of correspondences with different (combinations of) selection strategies.

- **Rejection based on the reliability of the normal vectors of corresponding points** For the recommended point-to-plane error metric (section 3.2.4) the normal vectors of corresponding points are needed. The normal vectors can be estimated for each point using a principal component analysis of the covariance matrix of the coordinates of neighbouring points (Shakarji, 1998). It is recommended to select a neighbourhood based on a fixed radius search, where the search radius should be chosen in dependence of (a) the point density and (b) the topography of the strips. Considering the point density in selecting the search radius should ensure that a sufficient number of neighbouring points is used for the normal vector estimation, e.g. $n \geq 8$, whereas the topography has to be considered so that the radius does not exceed the size of the available smooth surface areas. Usually, a search radius in the range of 1–3 m is appropriate in the case of lidar strips. Given this set of N three dimensional points $\mathbf{p}_{[n]}$, $n \in \mathcal{N} = \{1, \ldots, n, \ldots, N\}$, the 3-by-3 covariance matrix of its coordinates is denoted by $C(\mathbf{p}_{[n]})$. The principal components of the covariance matrix are its eigenvectors and form an orthogonal basis. The associated eigenvalues correspond to the variance in the directions of the eigenvectors. Assuming a descending ordering of the eigenvalues ($\lambda_1 \geq \lambda_2 \geq \lambda_3$), the third eigenvector $\mathbf{e}_3$ is a least-squares estimate for the normal vector of the adjusting plane ($\mathbf{n} = \mathbf{e}_3$). The square root of the third eigenvalue can be used as a reliability measure for the normal vector. This value corresponds to the standard deviation of the selected points from the estimated plane and can therefore be interpreted as a measure for the roughness of the adjusting plane

$$\sigma_p = \sqrt{\lambda_3} \tag{3.64}$$

To ensure a high reliability of the normal vectors, corresponding points within rough areas should be rejected for the alignment process, e.g.

$$\sigma_p \geq 0.1\,\text{m} \tag{3.65}$$

Figure 3.12 shows the overlap area of two lidar strips in a mountainous region where correspondences have been established within smooth areas only.

- **Rejection based on the angle between the normal vectors of corresponding points** This criteria rejects correspondences with strongly differing plane orientations. For this the angle between the normals of two corresponding points $\mathbf{p}_{[p]}$ and $\mathbf{q}_{[p]}$ is used:

$$\alpha = \arccos(\mathbf{n}_{\mathbf{p}_{[p]}}^T \cdot \mathbf{n}_{\mathbf{q}_{[p]}}) \qquad \text{for } ||\mathbf{n}_{\mathbf{p}_{[p]}}|| = ||\mathbf{n}_{\mathbf{q}_{[p]}}|| = 1 \tag{3.66}$$

To ensure that two corresponding points belong to the same plane, e.g. a roof or street, we recommend to reject all correspondences with α larger than

$$\alpha \geq 5^\circ \tag{3.67}$$

- **Rejection based on the distance between corresponding points** For this strategy the distribution of the a priori distances between corresponding points is analyzed. For the recommended point-to-plane error metric (section 3.2.4) the signed distances $d_{[p]}$, $p \in \mathcal{P}$, are assumed to have a Gaussian distri-

bution. A robust estimator for the standard deviation (Hampel, 1974) of this contaminated normal distribution is given by

$$\sigma_{\text{mad}} = 1.4826 \cdot \text{mad} \tag{3.68}$$

where mad is the median of the absolute differences (with respect to the median)

$$\text{mad} = \text{median}(|d_{[p]} - \widetilde{d}|) \qquad \text{for } p \in \mathcal{P} \tag{3.69}$$

where $\widetilde{d}$ denotes the median of the point-to-plane distances. We propose to reject all correspondences with distances outside the range

$$d_{\text{max}} = \widetilde{d} \pm 3\,\sigma_{\text{mad}} \tag{3.70}$$

- **Rejection of correspondences in non-stable areas** If multiple flight missions are carried out at different measurement epochs, the terrain might have been changed between these measurements. An example is shown in the Figures 4.7 and 4.8 where six lidar missions have been carried out between 2006 and 2015 to monitor the temporal development (*change detection*) of the Gepatschferner glacier (Oetztal alps, Austria) for geomorphological analysis. For multi-epoch adjustments it is necessary to restrict the correspondences to stable areas. As can be seen Figure 3.13 (left), bedrock areas have been chosen as stable areas for multi-epoch correspondences in this case. However, it may also be necessary to mask correspondences within a single flight mission. An example is shown in Figure 3.13 (right), where correspondences within the dynamic water areas have been rejected.

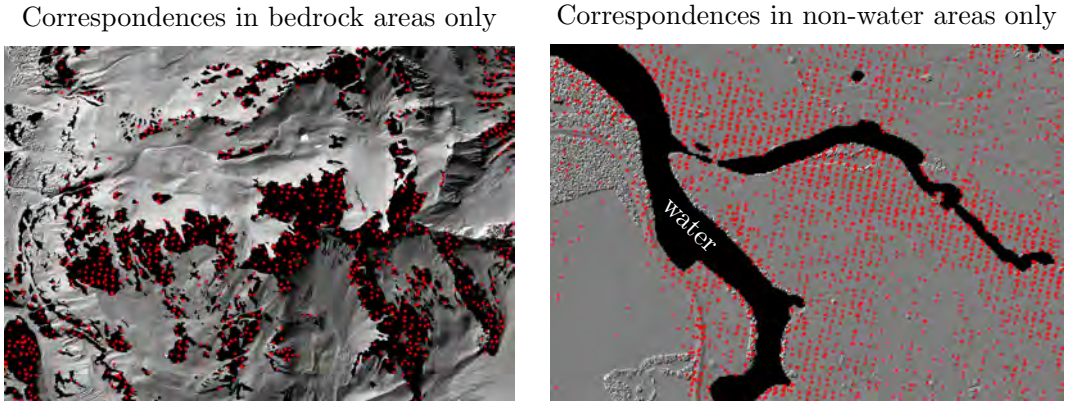

Figure 3.13: Limitation of correspondences to stable areas (left) and non-dynamic areas (right). The *Uniform Sampling* strategy was chosen for the selection of correspondences here.

Additionally, a rejection based on additional attributes can be performed if invariant attributes are available for the correspondences (Sharp et al., 2002). For example, if reflectance values are available from lidar measurements, false corresponding points can possibly be detected by comparing their reflectance values.

It is not guaranteed that with these strategies all outliers in the observation data

are rejected a priori. Thus, a robust adjustment method is highly recommended for the detection and removal of the remaining ones.

3.2.4 Error metric

The aim of the hybrid adjustment is to simultaneously improve the relative and absolute orientation of the lidar strips and the aerial images. This is achieved by minimizing some kind of distance measure (*error metric*) between the correspondences established in the previous steps. For this, two types of distances are commonly used (Figure 3.14):

1. **Point-to-point error metric** This error metric minimizes the Euclidean (unsigned) distance between corresponding points (Besl and McKay, 1992). The least squares objective function is thereby defined by

$$\Omega_{\text{point-to-point}} = \text{argmin} \left\{ \sum_{[p]=1}^{P} d_{s[p]}^2) \right\} \tag{3.71}$$

with the point-to-point distance defined as

$$d_{s[p]} = ||\mathbf{p}_{[p]} - \mathbf{q}_{[p]}|| \tag{3.72}$$

where $\mathbf{p}_{[p]}$ and $\mathbf{q}_{[p]}$ are the corresponding points of the $[p]$-th correspondence.

This error metric should be avoided in lidar, as generally, due to the different ground sampling of two lidar strips, no real point-to-point correspondences exist. Moreover, the convergence speed is somewhat slow (Rusinkiewicz and Levoy, 2001).

2. **Point-to-plane error metric** Perpendicular (signed) distance of one point to the tangent plane of the other point (Chen and Medioni, 1992). The least squares objective function for this error metric is:

$$\Omega_{\text{point-to-plane}} = \text{argmin} \left\{ \sum_{[p]=1}^{P} d_{p[p]}^2) \right\} \tag{3.73}$$

The point-to-plane distance can thereby be conveniently expressed by the Hessian normal form:

$$d_{p[p]} = (\mathbf{p}_{[p]} - \mathbf{q}_{[p]})^T \mathbf{n}_{[p]} \tag{3.74}$$

where $\mathbf{n}_{[p]}$ is the normal vector associated to the point $\mathbf{p}_{[p]}$ (with $||\mathbf{n}_{[p]}|| = 1$).

In contrast to the point-to-point error metric, it is not necessary that the corresponding points are identical in object space. The only requirement is that the corresponding points belong to the same plane in object space (e.g. roof or street). This error metric is characterized by a high convergence speed, as flat regions can slide along each other without costs, i.e. without increasing the value of the objective function $\Omega_{\text{point-to-plane}}$.

In Figure 3.15 a comparison between the two error metric is shown. It can clearly be seen that the convergence of the point-to-plane error metric performs significantly

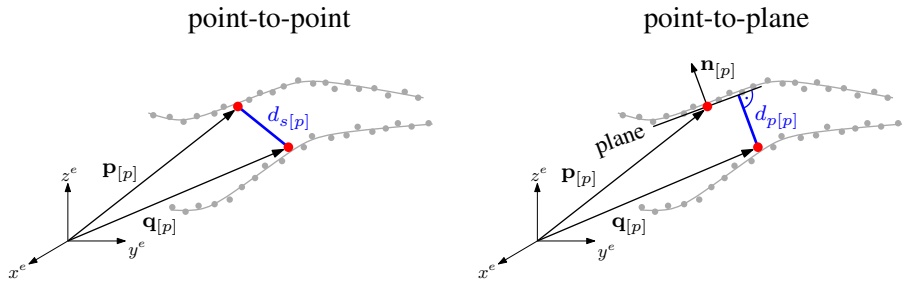

Figure 3.14: The point-to-point error metric minimizes the euclidean distance between two corresponding points (red). In contrast, the point-to-plane error metric minimizes the perpendicular distance from one point to the tangent plane of the other point.

better. Whilst the final alignment is reached with the point-to-point error metric only after 20 iterations, the convergence is approximately 4 times faster using the point-to-plane error metric.

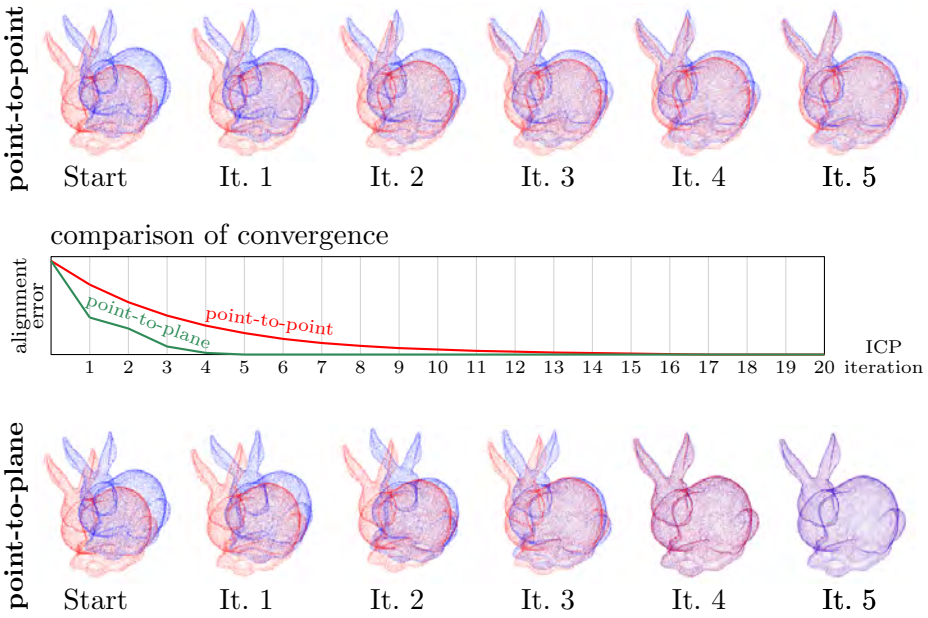

Figure 3.15: Comparison of convergence between point-to-point (top) and point-to-plane (bottom) error metric. A video of this comparison can be found at https://youtu.be/LcghboLgTiA.

3.2.5 Types of correspondences

3.2.5.1 STR-to-STR correspondences

These correspondences are established within the overlap area of two overlapping lidar strips (STR-to-STR), cf. Figure 3.9. We assume to have a set $\mathcal{K}$ of K overlapping lidar strip pairs, $\mathcal{K} = \{1, \ldots, k, \ldots, K\}$. The correspondences are established

for each of these pairs by the *selection* (section 3.2.1), *matching* (section 3.2.2), and *rejection* step (section 3.2.3). This leads to a set $\mathcal{P}$ of P STR-to-STR correspondences:

$$p \in \mathcal{P} = \{1, \ldots, p, \ldots, P\} \tag{3.75}$$

As shown in the previous chapter, a single correspondence is defined by two points from overlapping strips and their normal vectors (estimated from the neighbouring points). As a point and its normal vector define a tangent plane, consequently, a correspondence represents two homologous tangent planes in object space. In the adjustment the weighted sum of squared point-to-plane distances is minimized:

$$\Omega_{\text{STR-to-STR}} = \text{argmin} \left\{ \sum_{[p]=1}^{P} \left(w_{[p]}\, d_{[p]}^2 \right) \right\} \tag{3.76}$$

whereby, $w_{[p]}$ denotes the weight and $d_{[p]}$ the point-to-plane distance of the $[p]$-th correspondence defined by the lidar points $\mathbf{p}_{[p]}$ and $\mathbf{q}_{[p]}$. It should be noted, that these points are determined by the direct georeferencing equation (3.1), i.e. in consideration of the scanner measurements, the trajectory, the mounting calibration parameters, and the additional parameters described in section 3.1.

The *weights* of the correspondences $w_{[p]}$ could be estimated in a mathematically rigorous way by propagating the errors of the original measurements on the point-to-plane distances $d_{[p]}$. For that, the influencing factors (especially on the range measurement) need to be considered, e.g. the precision of the scanner and trajectory measurements, the precision of the mounting calibration parameters, the roughness of the ground, the material of the ground (especially its porosity and its water content), the incidence angle, the beam divergence, and the energy distribution within the footprint. In order to model these influences, many inputs are required, from which some parts may not be available or stem from unreliable sources. Instead, we propose to estimate the precision of the point-to-plane distances from the point clouds itself or, more specifically, from the previously established correspondences. Let us assume that the correspondence $[p]$ belongs to the strip pair $[k]$, then its weight is determined by

$$w_{[p]} = \frac{1}{\sigma_{\text{mad}[k]}^2} \tag{3.77}$$

with

$$\sigma_{\text{mad}[k]} = 1.4826 \cdot \text{mad}_{[k]} \tag{3.78}$$

where mad is the median of the absolute differences (with respect to the median) (Hampel, 1974) of all point-to-plane distances belonging to the strip pair $[k]$ and $\sigma_{\text{mad}[k]}$ is a robust estimator for the standard deviation of this possibly contaminated set of correspondences (due to false correspondences), cf. section 3.2.3.

3.2.5.2 CPC-to-STR correspondences

These correspondences are established within the overlap area of a control point cloud and a lidar strip (CPC-to-STR), cf. Figure 3.9. CPCs are fixed in object space (e-system) and therefore serve to define the datum. They can be provided in many forms, e.g. as georeferenced point clouds from Terrestrial Laser Scanning (TLS), as a DEM from an earlier flight campaign to which the new acquired block should fit,

or even as single (widely isolated) points from total station or GNSS measurements. Thus, a flexible concept, that can handle all these possibilities, is needed. We propose to treat the various forms of CPCs simply as further point clouds, whose orientations are fixed in object space. The correspondences are established by matching each CPC point to its nearest neighbour in the overlapping strips; this leads to a set $\mathcal{Q}$ of Q CPC-to-STR correspondences:

$$q \in \mathcal{Q} = \{1, \ldots, q, \ldots, Q\}$$

In the adjustment, like in the previous section, the weighted sum of squared point-to-plane distances is minimized

$$\Omega_{\text{CPC-to-STR}} = \text{argmin} \left\{ \sum_{[q]=1}^{Q} \left(w_{[q]}\, d_{[q]}^2 \right) \right\} \tag{3.79}$$

whereby the point-to-plane distances are defined by

$$d_{[q]} = (\mathbf{p}_{[q]} - \mathbf{q}_{[q]})^T \mathbf{n}_{[q]} \tag{3.80}$$

and the lidar strips and the CPCs are represented by the points $\mathbf{p}_{[q]}$ and $\mathbf{q}_{[q]}$, respectively. It is recommended to estimate the normal vector $\mathbf{n}_{[q]}$ from the lidar points, as this gives the possibility to use also isolated points (with unknown normal vector) as CPCs.

3.2.5.3 IMG-to-STR correspondences

These correspondences are established within the overlap area of the (coupled or loose) aerial images and the lidar strips (IMG-to-STR), cf. Figure 3.9. When integrating lidar and image measurements the specific characteristics of both measurement techniques must be considered. Even tough both techniques ultimately serve the mapping of the Earth's surface, they have a slightly different view on it. Lidar is an active measurement system operating at a single wavelength (mono-spectral), usually in the near infrared range. It relies on the diffuse backscattering of the emitted laser pulse. Usually lidar gives a rather uniform sampling of the Earth's surface. In contrast, photogrammetry is a passive measurement system capturing the scattered solar radiation in the optical spectrum. The photogrammetric reconstruction process relies on sufficient texture variance. Consequently, corners and edges can be well reconstructed, whereas the accuracy decreases in areas with low texture or a bad signal-to-noise ratio, e.g. shadowed areas. The main geometrical differences between the two techniques stem from the ability of the lidar pulse to penetrate small-scale structures (e.g. vegetation), whereas the photogrammetric reconstruction leads mostly to points from the topmost surface (Figure 3.16). For instance, in case of a grass field, the laser penetrates the grass layer to a certain extent, whereas the triangulated image points describe the top of the grass layer. Geometrical differences may also arise in case of dynamic areas (e.g. water) or objects (e.g. vehicles) due to different measurement times; while lidar is a continuous measurement system, images are captured at single points in time, thereby covering a larger area. These are some of the aspects that need to be considered in the hybrid adjustment. This particularly applies to the correspondences discussed in this

section, where only areas in which the scanner and the cameras have the same view on the Earth's surface should be taken into account.

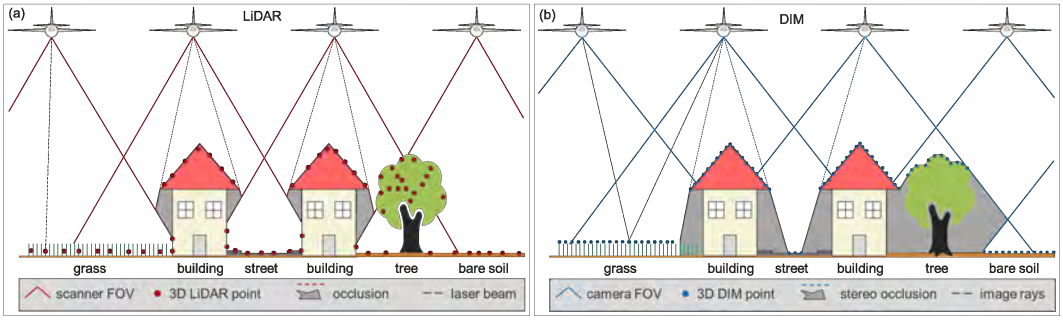

Figure 3.16: Reconstruction of points with (a) lidar and (b) DIM (from Mandlburger et al. (2017)).

In the above context, correspondences between lidar strips and images should be limited to smooth and textured areas. The IMG-to-STR correspondences are established (as usual) by the selection step, the matching step, and the rejection step. This leads to a set $\mathcal{V}$ of V IMG-to-STR correspondences:

$$v \in \mathcal{V} = \{1, \ldots, v, \ldots, V\}$$

In Figure 3.17 a set of IMG-to-STR correspondences is shown in object and image space. The depicted scene includes relatively flat areas (roads, roofs, facades, bare soil) and rough areas (low and high vegetation). In the first step a subset of image tie points can be selected by one of the selection strategies presented in section 3.2.1 (*selection* step). If feasible (e.g. in terms of computer memory), this step can be skipped so that *all* tie points are used for matching, as we did in this example. The correspondences are then established by matching the image tie points with the nearest neighbour in the lidar point clouds (*matching* step), cf. section 3.2.2. Finally, potentially wrong correspondences (outliers) are rejected by the criteria described in section 3.2.3 (*rejection* step). We rejected in this example all correspondences with an estimated roughness $\sigma_p \geq 0.02\,\text{m}$ (cf. equation 3.64) and with point-to-plane distances outside the range $\widetilde{d} \pm 3\,\sigma_{\text{mad}}$ (cf. equation 3.70). As can be seen, the resulting correspondences are predominately in smooth areas, e.g. on streets, terraces, roofs, and bare soil. Based on the roughness measure of each correspondence $[v]$, an individual weight ($0 \leq w_{p[v]} \leq 1$) is defined for each correspondence by

$$w_{p[v]} = 1 - \frac{\sigma_{p[v]}}{\sigma_{p,\text{max}}} \tag{3.81}$$

whereby $\sigma_{p,\text{max}}$ is the maximum allowed roughness measure (0.02 m in the current example). In the adjustment, the weighted sum of squared point-to-plane distances is minimized

$$\Omega_{\text{IMG-to-STR}} = \text{argmin} \left\{ \sum_{[v]=1}^{V} \left(w_{[v]} w_{p[v]}\, d_{[v]}^2 \right) \right\} \tag{3.82}$$

whereby $w_{[v]}$ is the weight defined by the measurement precision of the image tie

points and lidar points. We propose to estimate $w_{[v]}$ from the set of correspondences $\mathcal{V}$ in accordance to equation 3.77. The point-to-plane distances are defined by

$$d_{[v]} = (\mathbf{p}_{[v]} - \mathbf{q}_{[v]})^T \mathbf{n}_{[v]} \tag{3.83}$$

where the image tie points and the lidar strips are represented by the points $\mathbf{p}_{[v]}$ and $\mathbf{q}_{[v]}$, respectively. It is recommended to estimate the normal vector $\mathbf{n}_{[v]}$ from the lidar points, as the point density of the tie points is usually to low to ensure a reliable estimation of the normal vector.

Finally it is noted that in case of *coupled images* the lidar strips and the aerial images are not just linked by the IMG-to-STR correspondences, but they also share the same flight trajectory. This is especially important in areas where only few correspondences can be established (e.g. in case of dense vegetation or water) as the common trajectory prevents in such cases a divergence of the lidar block and the image block.

3.2.5.4 IMG-to-IMG and IMG-to-GCP correspondences

These two types of correspondences form the core of each bundle block adjustment of images (cf. Figure 3.9), therefore only a short summary is given here. The mathematical model for both types of correspondences is given by the collinearity equations (cf. eq. (3.20) and (3.21)).

Local features and their descriptors are used to establish correspondences between overlapping images (IMG-to-IMG). Many different feature detectors (e.g. SIFT, SURF, FAST) and descriptors (e.g. FREAK, BRISK, HOG) have been proposed in the past; a comparison addressing some of them can be found in Mikolajczyk and Schmid (2005). The object points – denoted as *image tie points* here – have *unknown* coordinates $X^e_{[t]}, Y^e_{[t]}, Z^e_{[t]}$ that are estimated by adjustment (cf. Table 3.3). These unknown coordinates usually represent the largest parameter block.

If object points with *observed* coordinates – i.e. Ground Control Points (GCPs) – are observed in image space, we denote this as IMG-to-GCP correspondences. At this point, it is worth mentioning that in the proposed hybrid adjustment the datum can be defined in different ways: (a) by CPCs, (b) by GCPs, (c) by fixing the trajectory of one ore more laser strips, or (d) by fixing the given orientation of a subset of images. Of course, options can be combined. The optimal choice of options depends largely on the specific project. For instance, if change detection among different measurement epochs is the aim of the project, it might be the best choice to introduce the DEM of one epoch as CPC for the other ones. A main benefit of the hybrid adjustment is that, e.g. in the presence of CPCs, the datum of the images can be adjusted without the explicit need of GCPs, whose measurement in object and image space is usually quite time-consuming. Of course this applies in reverse as well, i.e. the datum of the laser scanner block can be adjusted with GCPs only. However, due to this high flexibility, options are manifold and further investigations are necessary to fully understand the mutual influence between these options.

The objective is to minimize for both types of correspondences the weighted sum of squared residuals (= reprojection errors). Having a set $\mathcal{R}$ of R IMG-to-IMG correspondences and a set $\mathcal{U}$ of U IMG-to-GCP correspondences

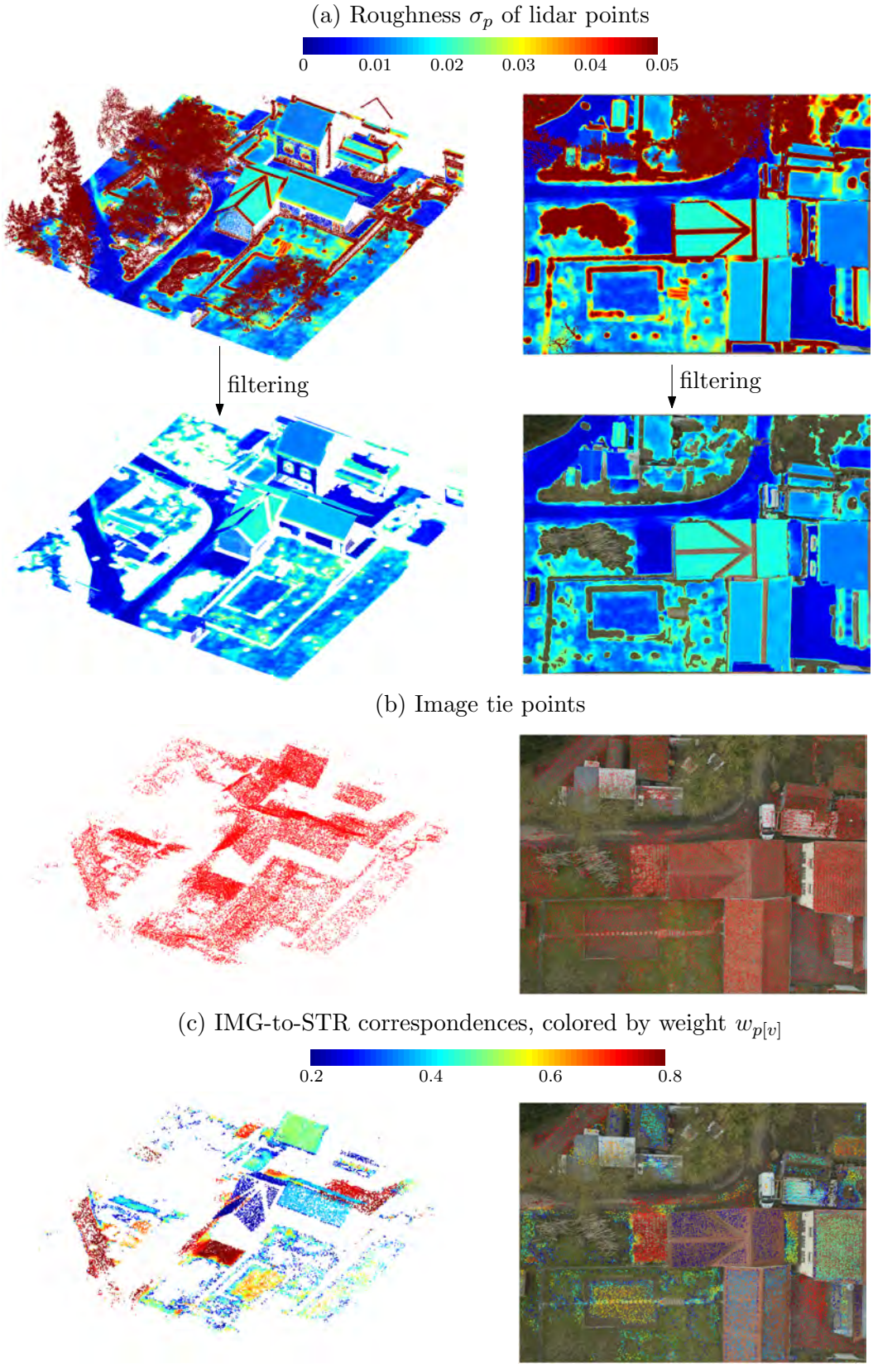

Figure 3.17: Correspondences between image tie points and lidar strips (IMG-to-STR) in object space (left) and image space of a single image (right).

Figure 3.18: Example of IMG-to-IMG matches. Here, only every 500-th correspondences is shown of the 16377 correspondences that have been found in total. This image pair is taken from the example in section 4.4.

$$r \in \mathcal{R} = \{1, \ldots, r, \ldots, R\}, u \in \mathcal{U} = \{1, \ldots, u, \ldots, U\}$$

we can therefore formulate the two objective functions by

$$\Omega_{\text{IMG-to-IMG}} = \text{argmin} \left\{ \sum_{[r]=1}^{R} \left(w_{x_{[r]}} r_{x_{[r]}}^2 + w_{y_{[r]}} r_{y_{[r]}}^2 \right) \right\} \tag{3.84}$$

$$\Omega_{\text{IMG-to-GCP}} = \text{argmin} \left\{ \sum_{[u]=1}^{U} \left(w_{x_{[u]}} r_{x_{[u]}}^2 + w_{y_{[u]}} r_{y_{[u]}}^2 \right) \right\} \tag{3.85}$$

whereby the weights w are derived from the covariance matrix of the uncertain image measurements and r are the reprojection errors, i.e. the discrepancies between the modeled and the measured image coordinates.

3.3 Workflow and solution

A simplified flowchart of the hybrid adjustment is shown in Figure 3.19. For the sake of simplicity, we thereby omitted all I/O-steps, i.e. the import and export of the data. The workflow can be divided into three stages: the pre-processing, the main iteration loop, and the post-processing stage.

The pre-processing stage includes three image-based steps. The two objectives of this stage are to establish the IMG-to-IMG correspondences and to get a first estimate of the 3D coordinates of the image tie points. These coordinates are estimated in a pure aerial triangulation (i.e. without consideration of lidar strips and CPCs) and are used for the IMG-to-STR matching in object space later on.

The main iteration loop starts with the direct georeferencing of the lidar strips. Thereby the *current* parameters are used, i.e. the priors of the parameters in the first iteration and the parameters estimated by the hybrid adjustment for all subsequent iterations. Then, as in the ICP algorithm, the correspondences in object space (STR-to-STR, CPC-to-STR, IMG-to-STR) are newly established in each iteration. After

the hybrid adjustment a convergence criteria is tested, e.g. the relative change of the weighted sum of squared errors. If it is not met, a new iteration starts. Usually, due to the high convergence speed of the point-to-plane error metric (cf. Fig. 3.14) only 3 to 5 iterations are needed until convergence is reached.

Finally, the lidar strips are georeferenced with the last parameter estimates in the post-processing stage.

The observations and respective objective functions for each type of correspondence have been defined in the previous sections by the equations 3.76, 3.79, 3.82, 3.84, and 3.85. Additionally, if parameters have been directly observed, fictional observations are introduced into the adjustment. This is done by minimizing

$$\Omega_{\text{FO}} = \text{argmin} \left\{ \sum_{j=1} w_j \Delta x_j^2 \right\} \tag{3.86}$$

with

$$\Delta x_j = \hat{x}_j - x_{0,j} \tag{3.87}$$

where $x_{0,j}$ is the initial value of the parameter with the index j, $\hat{x}_j$ its estimated value by adjustment, and $w_j = 1/\sigma_j^2$ the weight defined by the measurement precision σ_j. We already discussed the fictional observation of the polynomial coefficients for the *Spline Trajectory Correction Model* in section 3.1.4.1 and the fictional observations for the correction parameters of the image's exterior orientation in section 3.1.2. Besides that, direct observations of parameters are typically introduced for terrestrial measurements of the mounting calibration parameters (misalignment angles and lever-arm) and the object coordinates of the GCPs.

Summarizing, the objective function of the hybrid adjustment is defined by

$$\begin{aligned} \Omega_{\text{HA}} = \text{argmin}\{ & \Omega_{\text{STR-to-STR}} + \Omega_{\text{CPC-to-STR}} + \\ & \Omega_{\text{IMG-to-STR}} + \Omega_{\text{IMG-to-IMG}} + \\ & \Omega_{\text{IMG-to-GCP}} + \Omega_{\text{FO}} \} \end{aligned} \tag{3.88}$$

That is, the least squares adjustment is expected to minimize the weighted squared sum of the following quantities:

- STR-to-STR: The point-to-plane distances between overlapping lidar strips.
- CPC-to-STR: The point-to-plane distances between the datum-defining CPCs and the overlapping lidar strips.
- IMG-to-STR: The point-to-plane distances between the image tie points and overlapping lidar strips.
- IMG-to-IMG: The reprojection errors of the image tie points in image space.
- GCP-to-IMG: The reprojection errors of the datum-defining observed GCPs in image space.
- FO: The differences between the parameter's initial and estimated values for a subset of parameters.

By minimizing these quantities, the parameters described in section 3.1 are estimated, cf. Table 3.3.

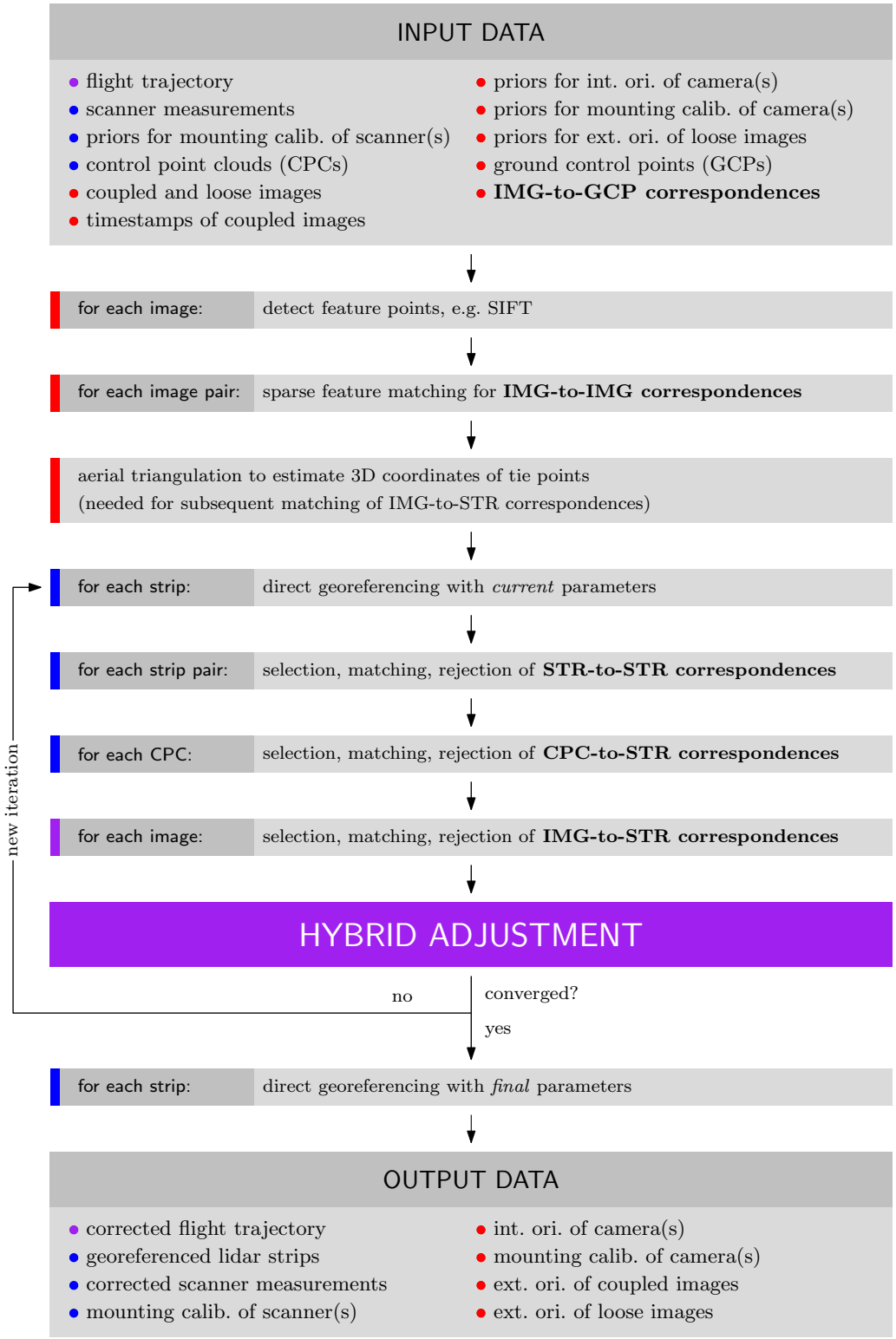

Figure 3.19: Flowchart of hybrid adjustment method. Blue: lidar related steps/data. Red: image related steps/data. Purple: lidar *and* image related steps/data.

4 Experimental results

We will show the practical benefits and limits of the hybrid adjustment on the basis of four examples.

4.1 Correspondence framework: comparison of variants

In this example, the introduced correspondence framework is demonstrated on the basis of synthetic lidar data. The motivation for using synthetic data is that the correct orientation is known exactly, and the correctness of the estimated transformations can be evaluated relative to this ground truth orientation. A digital elevation model (DEM) of the selected lidar scene, which consists primarily of almost flat terrain intersected by a narrow ditch, is shown in Figure 4.1. This dataset was chosen because it is a rather difficult scene for most surface matching algorithms, as there is only one feature – the ditch – which can constrain the transformation at the finest level. Thus, this dataset is used to emphasize the differences among the presented variants.

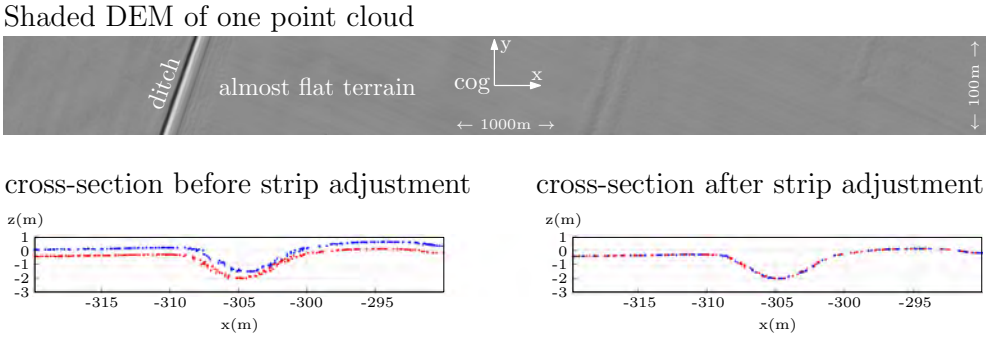

Figure 4.1: Top: digital elevation model of lidar test scene, bottom: cross-section through ditch before and after the strip adjustment.

The two synthetic point clouds were generated by the following steps:

1. Extraction of a $1000 \times 100\,\mathrm{m}^2$ area from a real lidar strip.
2. Derivation of a DEM from this point cloud (least squares moving planes interpolation, grid size = 0.5 m).
3. Generation of the two synthetic lidar strips: bilinear interpolation of the DEM at randomly distributed positions in the xy plane for each of the two point clouds (mean point density = $5\,\mathrm{points/m}^2$).
4. Transformation of one of the two point clouds by a rigid body transformation. For the first two experiments (comparison of selection strategies and error

metric) a translation vector $t = (0.5\,0.5\,0.5)^T$ m and a rotation about the z axis with $\alpha_Z = 0.1°$ were chosen. This leads to point displacements at the edges of the point cloud of about 1 m, which is far more than usual displacements between real lidar strips. For the third experiment (convergence analysis), each of the 6 transformation parameters was varied within a specific range, whereas the other 5 transformation parameters were set to zero.

The ICP algorithm (section 2) applied in this experiment tries to bring back the transformed point cloud to its original position. After each iteration, for each point the euclidean distance between its actual position and its original position can be computed. We denote the root-mean-square of these distances as alignment error and use this error metric for the comparison of different ICP variants. As transformation model the rigid body transformation (3 rotations, 3 translations) was chosen.

Comparison of Selection Strategies First, we examine the effect of the selection strategies (introduced in section 3.2.1) on the convergence of the ICP algorithm. For this purpose, with each strategy about 300 points are selected for the estimation of the 6 transformation parameters.

As can be seen in Figure 4.2, with *Random Sampling (RS)* and *Uniform Sampling (US)*, most of the points are selected in flat regions, containing a lot of redundant information for the alignment process. From these points the translation in x and y, as well as the rotation around the z axis, can only hardly be estimated. For these 3 parameters, points within the ditch would be most useful, but since these strategies don't focus on local terrain features, only a few points are selected within this area.

However, *Normal Sampling (NS)* and *Maximum Leverage Sampling (MLS)* consider the usefulness of points for the alignment process. Especially the MLS strategy selects the points with the highest leverage on the estimation of the transformation parameters. Thus, for the test scene, points are predominantly selected within the ditch and – in order to constrain the rotation about the ditch axis – in a perpendicular direction to it. It can also be recognized that the algorithm prefers points towards the edges, as they better constrain the transformation.

	Translation [mm]			**Rotation** [(″) = 1/3600 °]		
	σ_{t_x}	σ_{t_y}	σ_{t_z}	σ_{α_x}	σ_{α_y}	σ_{α_z}
RS	38.0	29.6	0.3	0.033	0.003	0.410
US	30.5	23.8	0.2	0.024	0.003	0.314
NS	17.8	47.9	0.7	0.079	0.009	0.661
MLS	11.5	22.2	0.6	0.059	0.007	0.261

Table 4.1: Precision of estimated transformation parameters for different sampling strategies in first ICP iteration. RS = Random Sampling, US = Uniform Sampling, NS = Normal Sampling, MLS = Maximum Leverage Sampling.

The convergence of the ICP algorithm for different selection strategies can be compared in Figure 4.2. Here, one can see that with RS and US the convergence rate is rather slow and, even worse, the final alignment error is 2-3 times larger than

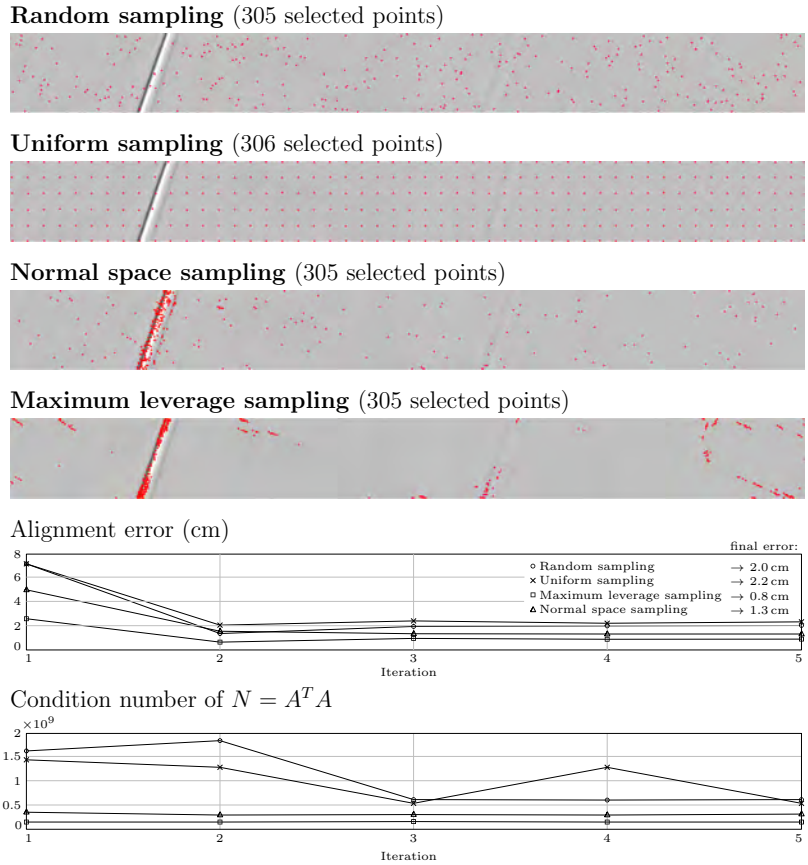

Figure 4.2: Effect of different correspondence selection strategies on convergence and condition number.

with MLS. NS performs relatively well, but since points are not selected optimally, the final error is considerably larger than with MLS. The point selection not only influences the convergence of the ICP algorithm, but also the a posteriori stochastic of the parameters. The standard deviations of the transformation parameters for the first ICP iteration can be compared in Table 4.1. For further iterations, the ratios between different selection strategies remain similar. This is also confirmed by a comparison of the condition numbers of the normal equation matrix $N = A^T A$, which indicate if the equation system is ill-conditioned (high condition number) or well-conditioned (low condition number).

Comparison of Error Metrics In section 3.2.4 the point-to-point and point-to-plane error metric were introduced. As shown in Figure 4.3, the convergence speed of the point-to-point error metric is very slow, and even for a good initial alignment many ICP iterations are necessary until the final alignment is reached. However, with the point-to-plane metric flat regions can slide along each other within one iteration without causing costs and therefore speed of convergence is improved dramatically.

Convergence Analysis The errors to be minimized by a strip adjustment have typically magnitudes of up to a few dm. Only in exceptional cases the displacement

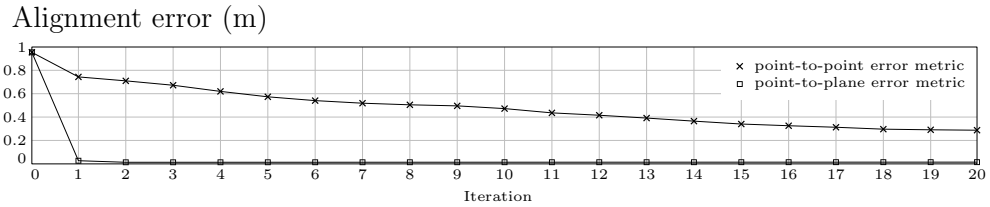

Figure 4.3: Effect of different error metrics on the convergence of the strip adjustment. The results are based on the *Uniform Sampling* strategy for correspondence selection.

of lidar strips are affected by gross errors, e.g. due to a wrong processing of the trajectory. Such errors can cause point displacements in the range of several meters. With this experiment we tried to find out if the presented method converges also with such bad initial orientations, and if so, how many iterations are necessary until the global minimum is reached. For this purpose, each of the six transformation parameters was varied for the transformation of one point cloud within a specific range, whereas the remaining five parameters were set to zero. For each transformation parameter the range limits were selected so that they cause maximum point displacements of about 10 m. In Figure 4.4 the numbers of iterations which are necessary to reach an alignment error smaller than 1 cm (stop criterion) are reported for each experiment. For example, for $t_x = 6\,\text{m}$ (and $t_y = t_z = \alpha_x = \alpha_y = \alpha_z = 0$) the presented method needs 7 iterations to fulfill the stop criterion. It can be seen that even for this difficult scene, all adjustments converged to the right solution. However, it should be noted that if the initial alignment is very bad, a relatively high number of iterations can be necessary, e.g. 9 iterations for $t_x = -10\,m$. In our experience, gross errors in airborne lidar are always far below the selected range limits and therefore a divergence of the strip adjustment can almost be excluded.

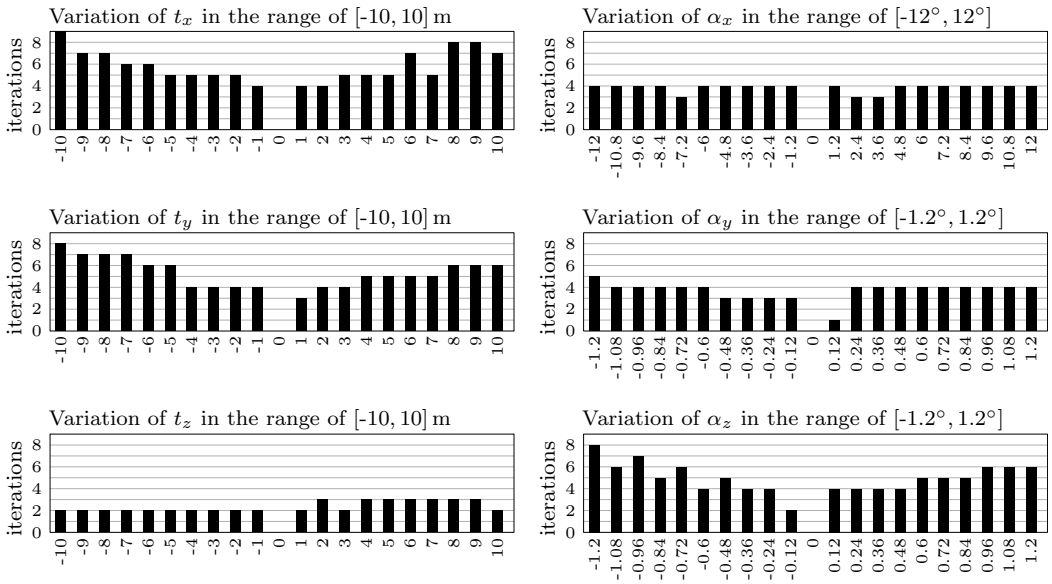

Figure 4.4: Convergence analysis by variation of transformation parameters.

4.2 Lidar strip adjustment for geomorphological studies

In this example, we demonstrate the application of the strip adjustment method on an airborne lidar block measured in July 2012 which is located in the Austrian Alps (Tyrol, Kaunertal, Gepatschferner) (46°51'85" N, 10°42'79" E; WGS 84). This block is one of a total of 6 blocks acquired between 2006 and 2015 for geomorphological studies. The block consists of 95 longitudinal strips and 8 cross strips (Figure 4.5 (a)); the cross strips were flown in both directions. The lidar system was carried by a helicopter that flew over the terrain in a constant height above ground of approx. 600 m. Further information about the flight campaign is summarized in Table 4.2. A quality control of the delivered data revealed large systematic discrepancies (of up to several dm) in the overlap area of neighbouring strips. For this reason, an improvement of the georeferencing of the data by means of strip adjustment, was absolutely necessary.

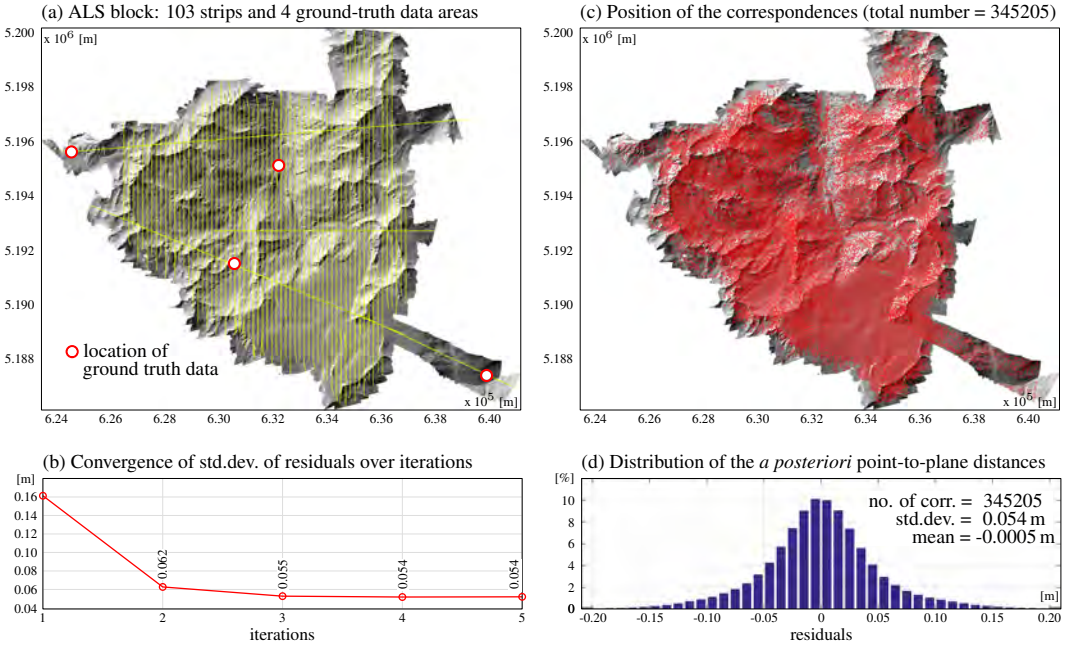

Figure 4.5: Strip adjustment results for an airborne lidar block covering an area of approx. 119 km^2 in the Austrian Alps (Kaunertal).

Next to the georeferenced strips, also the original scanner measurements and the trajectory data were provided. However, no *a priori* information about the mounting calibration was available. Thus, approximate values for these parameters were determined so that the misalignment R_s^i approximately rotates the s-system into the i-system, whereas the lever-arm $\mathbf{a}^i$ was approximated by the null vector. In total, 627 parameters were estimated in the adjustment; this includes 3 scanner calibration parameters (range offset $\Delta\rho$, range scale ε_ρ, scan angle scale ε_α), 6 mounting calibration parameters, and 6 trajectory correction parameters for each of the 103 strips (*Bias Trajectory Correction Model*, cf. Figure 3.6). As it can be seen in Figure 4.5 (b), five correspondence iterations (cf. Figure 3.19) were performed within the strip adjustment, although three iterations would have been sufficient. The reason for this is that we used, instead of a convergence criteria based e.g. on the change of

Lidar data specifications	
scanner model	Riegl LMS-Q680i
area of lidar block	approx. 119 km^2
no. of strips	103
no. of ground-truth data areas	4
size of input data	58.8 GB
overall no. of points	1 455 111 768
mean point density (single strip)	2.5 points/m^2
mean point density (block)	12.2 points/m^2
frequency of trajectory data	256 Hz
terrain elevation	2100 to 3450 m

Table 4.2: Key parameters of the lidar data used.

the parameter estimates $\hat{\mathbf{x}}$ after each iteration, a fixed number of 5 correspondence iterations.

In total, 748 pairs of overlapping strips were identified. The STR-to-STR correspondences between each of these strip pairs were selected by the *Uniform Sampling* strategy with a mean sampling distance of 50 m. In this mountainous region, this strategy led to a broad and relatively homogeneous distribution of the normal vector directions. The normal vectors were estimated by considering all neighbouring points within a fixed search radius of 2 m. In order to ensure the reliability of the normal vector estimation, correspondences were rejected in rough areas (e.g. vegetation) with $\sigma_p > 10$ cm. The positions of the correspondences are visualized in Figure 4.5 (c). The distribution of the *a posteriori* point-to-plane distances $d_{[p]}$ is shown in Figure 4.5 (d). The residuals are normally distributed, which indicates that systematic errors were widely eliminated by strip adjustment and confirms the appropriateness of the applied transformation model. In Figure 4.6 the mean and the standard deviation of these residuals are visualized individually for each strip pair. The strip pairs are thereby ordered by decreasing number of correspondences. As expected, the magnitude of the mean values is increasing by decreasing no. of correspondences (which is equivalent to a decreasing weight of the strip pairs), whereas the standard deviation remains, mainly due to the homogeneity of the terrain and of the surveying conditions, nearly constant.

The datum of the lidar block was defined by 4 control point clouds (Figure 4.5 (a)). Altogether, these areas consist of 205 points, which were chosen predominantly on roofs and streets and were determined by a combination of static GNSS and total station measurements. These points were matched with 24 overlapping strips, giving in total 632 datum-defining CPC-to-STR correspondences.

Change detection In total, six lidar blocks of the Gepatschferner glacier have been measured between 2006 and 2015. The main aim of these missions was to study the geomorphological processes in this area on the basis of height difference models. An overview about the lidar missions is shown in Figure 4.7. One can see, that the amount of data almost tripled within 10 years. Each of these blocks has been adjusted by the method presented herein. The bedrock areas of the lidar block

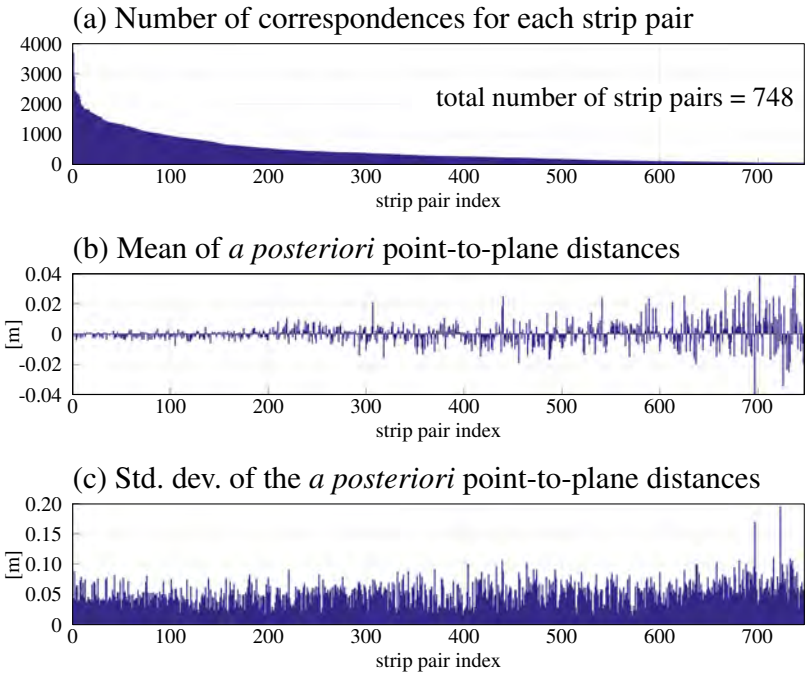

Figure 4.6: Strip adjustment results for all 748 overlapping strips pairs. The strip pairs are ordered according to the no. of correspondences.

described above (2012/07) have been used as control point clouds in the adjustments of the remaining lidar blocks. The changes of the glacier tongue over the years is visualized as shaded DEMs in Figure 4.8. A 3D visualization of the height changes from 2012/07 to 2014/07 is shown in Figure 4.9. Here, it can be recognized that height differences within stable areas are within ±4 cm.

Results	
no. of estimated parameters	627
no. of iterations	5
no. of overlapping strip pairs	748
no. of correspondences (STR-to-STR)	345205
→ mean of residuals	-0.0005 m
→ std.dev. of residuals	0.054 m
no. of correspondences (CPC-to-STR)	632
→ mean of residuals	-0.0002 m
→ std.dev. of residuals	0.053 m

Table 4.3: Strip adjustment results.

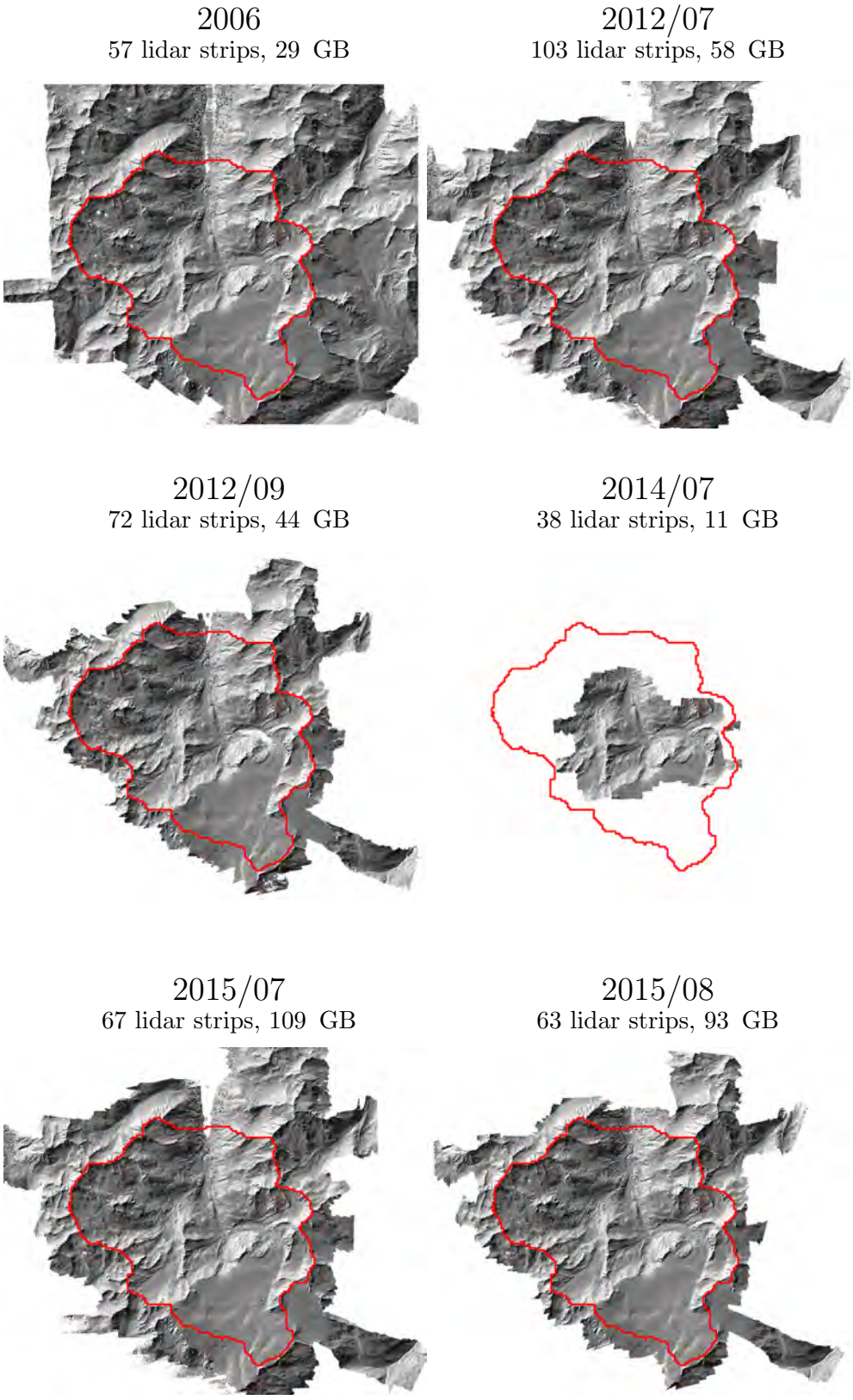

Figure 4.7: Lidar blocks of the Gepatschferner glacier measured between 2006 and 2015.

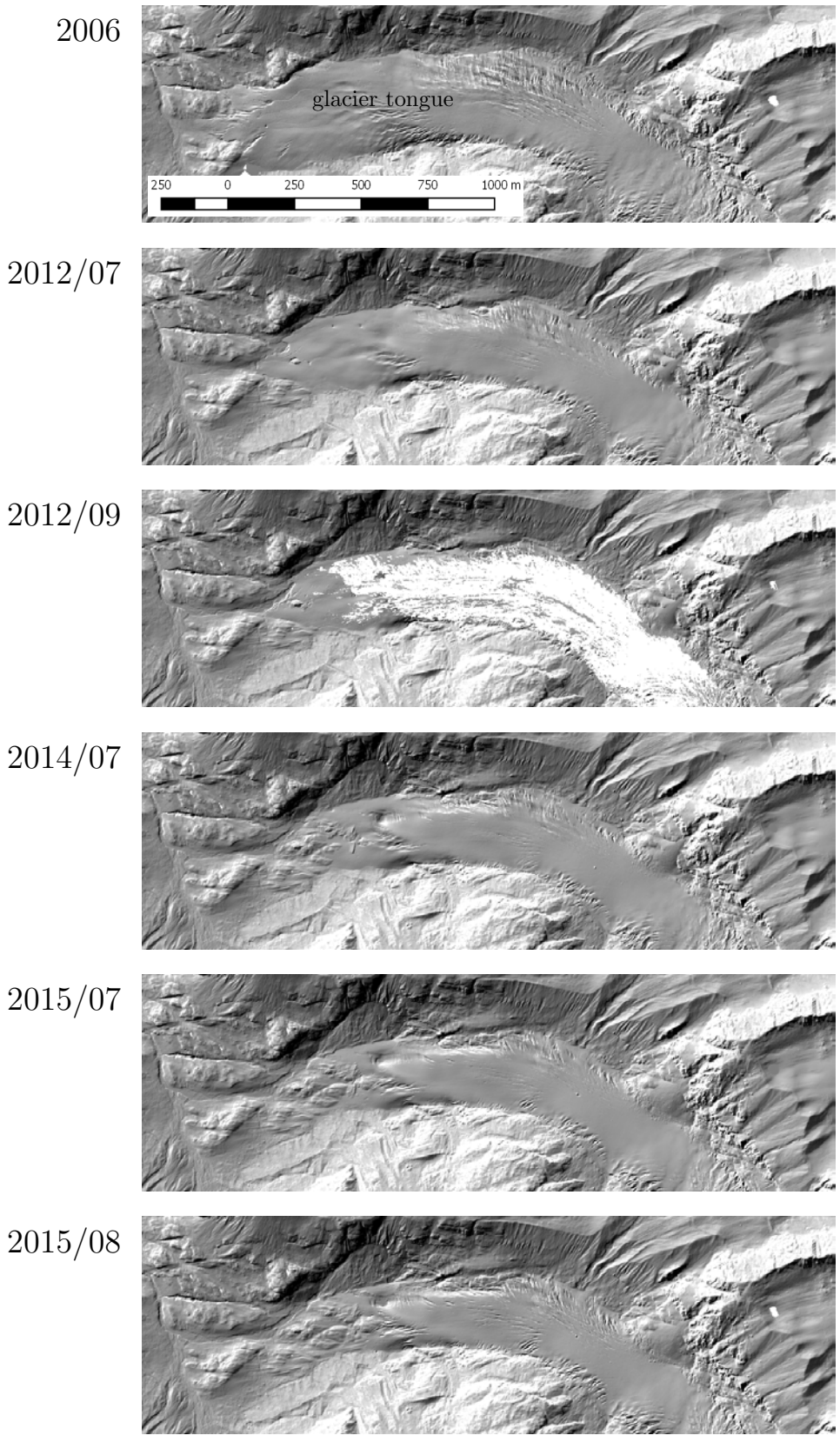

Figure 4.8: The tongue of the Gepatschferner glacier from 2006 to 2015.

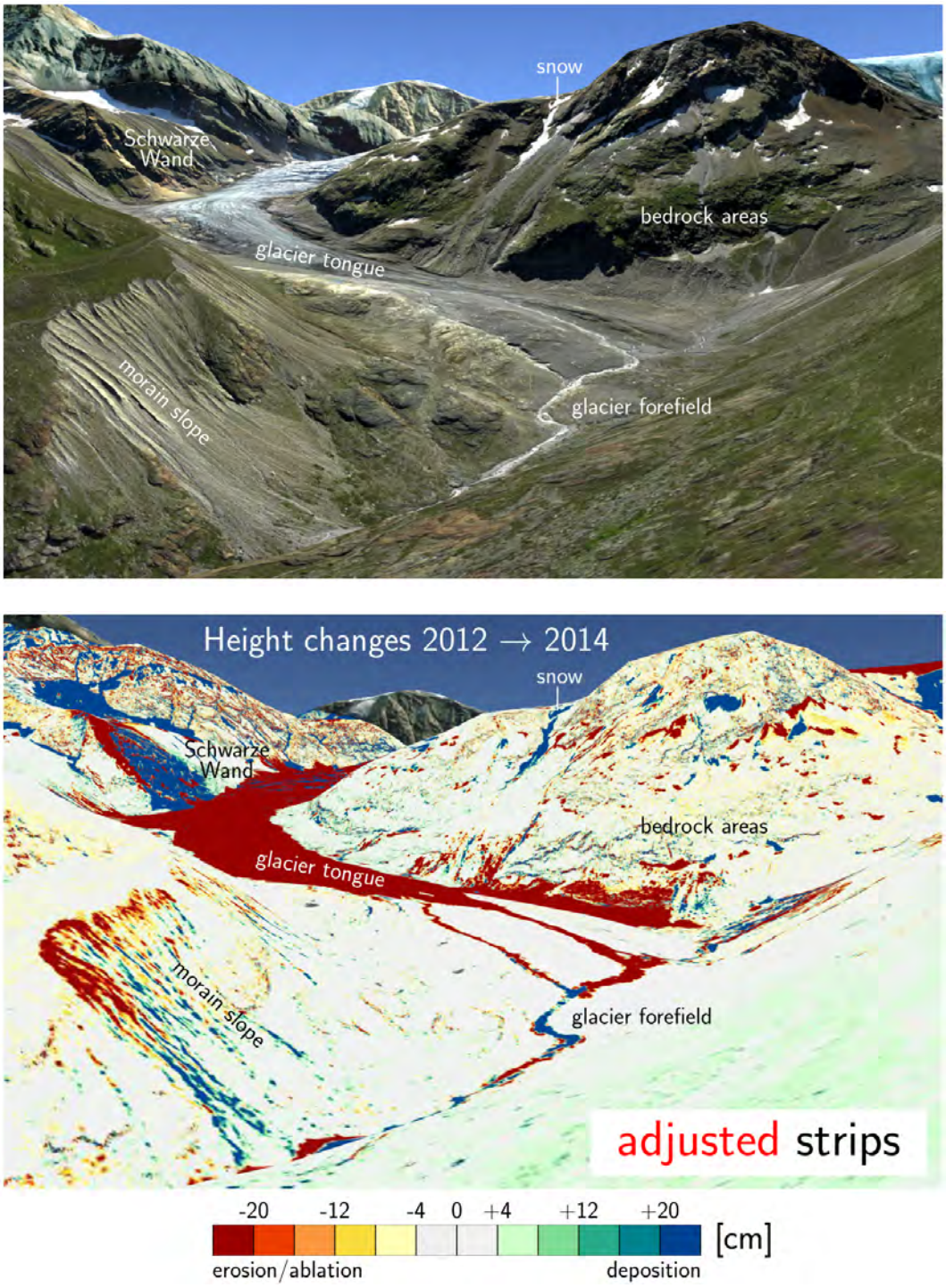

Figure 4.9: Height changes between the measurement epochs 2012/07 and 2014/07.

4.3 Correction of time-dependent trajectory errors

In this example the correction of time-dependent trajectory errors using the *Spline Trajectory Correction Model* is demonstrated. The study site Neubacher Au is a Natura2000 protection area located at the lower course of the Pielach River (Lower Austria) near the confluence with the Danube River (48°12'50" N, 15°22'30" E; WGS 84). Due to the complex topography and vegetation structure, the alluvial area was captured under leaf-off conditions by a UAV-mounted laser scanner (Figure 4.10, top right). The manufacturer's specifications about the UAV, the laser scanner, and the GNSS/INS solution are reported in Table 4.4.

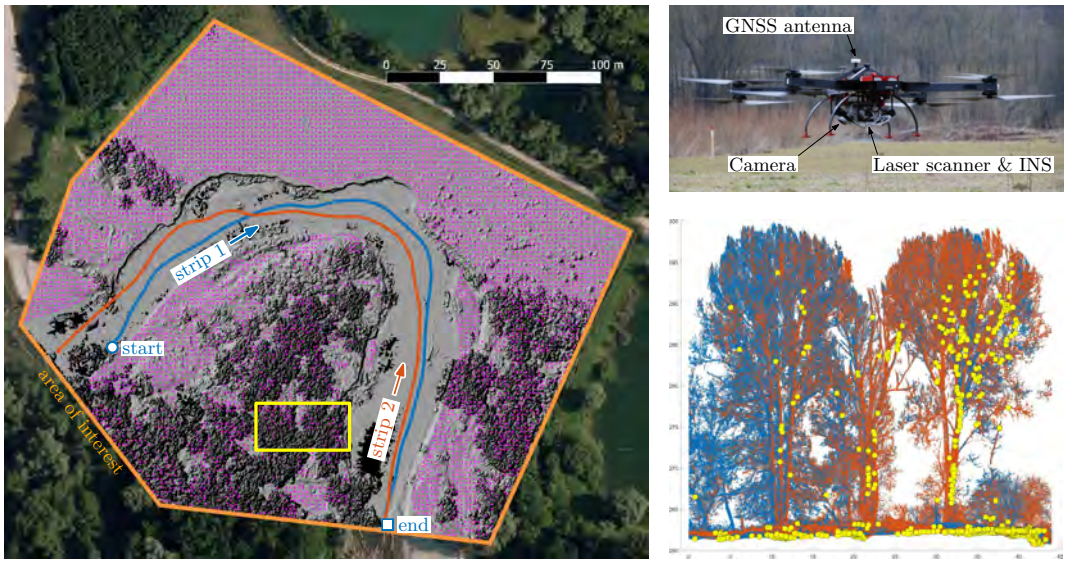

Figure 4.10: The trajectory correction model is demonstrated on the basis of a single pair of strips (flight trajectories in blue/orange). These two strips were acquired by following the course of the Pielach river in 25 m flying altitude. The magenta points were taken from a simultaneous (manned) lidar campaign and introduced as control point cloud into the strip adjustment. The point clouds within the rectangle are depicted at the bottom right corner (yellow points = position of STR-to-STR correspondences in this area). Top right: Riegl RiCopter.

Data capturing was carried out with 14 longitudinal, 4 cross strips, and 2 strips along the Pielach river[1]. The regular distance between longitudinal strips was 40 m and the flying altitude was 25–50 m above ground. Depending on the sensor-to-target range the resulting laser footprint diameter is 1.0–2.5 cm, enabling the detection of small vegetation objects. The UAV was autonomously flying the programmed path (based on waypoints) with a speed of 8 m/s. The mission parameters and the large scanner field of view resulted in a mean laser pulse density of 1500 points/m^2 and in multiple strip overlaps so that the vegetation was captured from multiple sides (cf. Figure 4.11). The point clouds acquired in this flight campaign were already used in other publications: in Mandlburger et al. (2015b) the potential

[1] An animation of the captured point clouds after strip adjustment can be seen here: https://youtu.be/GwyNhUjFr2I

Measurement system		
laser scanner	model	Riegl VUX-1UAV
	pulse repetition rate	350 kHz
	range accuracy	10 mm
	range precision	5 mm
	scan angle resolution	0.001°
	field of view	230°
	beam divergence	0.5 mrad
	wavelength	1550 nm
GNSS/INS	model	Trimble Applanix AP20
	roll accuracy	0.015°
	pitch accuracy	0.015°
	yaw accuracy	0.035°
	position accuracy	5-30 cm
	INS sampling rate	200 Hz
UAV	model	Riegl RiCopter
	max. payload	16 kg
	max. flight time	30 min
	size	192 x 182 x 47 cm

Table 4.4: Key features of the deployed measurement system as declared by the manufacturers.

of the data for vegetation modelling was investigated and in Mandlburger et al. (2015c) a comparison between airborne and bathymetric lidar data was presented. For these works, strip adjustment was performed for all strips. However, for a better understanding, the presented *Spline Trajectory Correction Model* is demonstrated in the following on the basis of a single pair of strips only (Figure 4.10).

In this minimal example we compare the results of the *Spline Trajectory Correction Model* with the simple *Bias Trajectory Correction Model* (Table 4.5). With the latter only a bias is estimated for each trajectory element per strip; looking at the equations (3.29) and (3.30) this corresponds to

$$n_{[s]} = 1 \quad \Rightarrow \Delta t = t_{e[s]} - t_{s[s]} \tag{4.1}$$

$$a_{1[s][k]} = a_{2[s][k]} = a_{3[s][k]} = 0 \tag{4.2}$$

and the coefficient $a_{0[s][k]}$ is the bias estimated by adjustment.

The two investigated strips were acquired by following the course of the Pielach river in 25 m flying altitude. These two strips were later used to investigate short term water level differences, thus a very high strip registration accuracy was required to distinguish signal (i.e. water level differences) from noise. To minimize the discrepancies between these two strips, approx. 29000 STR-to-STR correspondences were established (cf. Figure 4.12) ...

- within the overlap volume of the two strips,

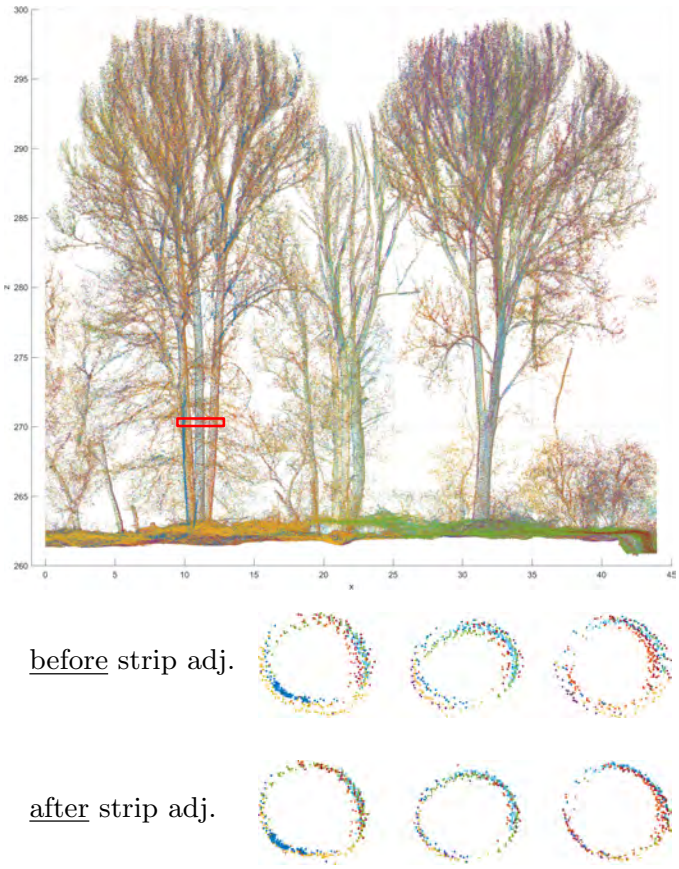

Figure 4.11: Top: Point cloud captured during an airborne lidar campaign *after strip adjustment* (different colors correspond to different flight strips). Below: horizontal section through the stems of a tree (height = 0.5 m) before and after strip adjustment.

- inside the area of interest,
- outside the river area due to the water dynamics, and
- only on relatively smooth surface areas (details later).

The *Normal Space Sampling* method (section 3.2.1) was used for the selection of the correspondences. Thereby, the correspondences are selected so that the distribution of their normals in angular space (slope vs. aspect) is as uniformly as possible. As can be seen in Figure 4.10 (bottom right), this leads to a broad distribution of the correspondences in 3D object space, i.e. correspondences are not only established on the terrain, but also on thicker stems and branches.

The datum of the strip adjustment was defined by a control point cloud containing 5630 homogeneously distributed points, which have been extracted from a simultaneous *manned* airborne lidar flight campaign (Figure 4.10, left). These points were matched with the two overlapping strips, giving in total approx. 7900 datum-defining CPC-to-STR correspondences. The large number of ground truth points avoid the problem of block deformation, which was discussed in section 3.1.4.1.

Strip adjustment results		
	Bias TCM	*Spline TCM*
# parameters		
• scanner calibration	4	4
• mounting calibration	6	6
• trajectory correction coefficients	11	504
# observations		
• correspondences		
• STR-to-STR (Figure 4.12, 4.13)	29180	28662
→ *std. dev. residuals*	*1.83 cm*	*1.38 cm*
→ *mean residuals*	*0.01 cm*	*0.00 cm*
• CPC-to-STR	7888	7866
→ *std. dev. residuals*	*1.82 cm*	*1.65 cm*
→ *mean residuals*	*0.00 cm*	*0.00 cm*
• coefficients (eq. 3.41)	0	126
# constraints	0	390
redundancy	37047	36530

Table 4.5: Comparison of strip adjustment results for both trajectory correction models (TCM).

To minimize the point-to-plane distances, the normal vector is needed for each correspondence (cf. Figure 3.14). The normal vectors were estimated by considering a maximum no. of 20 neighbouring points within a maximum search radius of 0.5 m. However, if the estimated normal vector is unreliable – i.e. if the standard deviation of the points from the adjusting plane exceeds $\sigma_{p,\max}$ – the associated correspondence was rejected. As a result, correspondences are established within relatively smooth areas only (in this example we used $\sigma_{p,\max} = 2\,\text{cm}$). All parameters, i.e. the search radius, the no. of neighbouring points, and $\sigma_{p,\max}$, were chosen empirically by considering the point density, the topography, and the measurement accuracy of the laserscanner (Table 4.4).

In Figure 4.12 and 4.13 the residual point-to-plane distances of each STR-to-STR correspondence can be inspected in object space and time domain, respectively. As can clearly be seen, using the *Bias Trajectory Correction Model* the residuals show a strong systematic pattern, with amplitudes of up to 3-4 cm. As these errors are significantly larger than the measurement accuracy of the laser scanner (Table 4.4), it can be concluded that time-dependent trajectory errors are the dominant remaining error source. If we take a closer look at the error pattern in time domain (upper part of Figure 4.13), it can be recognized that the systematic part of these errors can be well-modelled by smooth and continuous functions, e.g. by cubic splines, as we propose here. Thus, with the *Spline Trajectory Correction Model* the systematic errors could be widely eliminated, leading to residuals that are mainly random distributed over time (lower part of Figure 4.13). We have chosen in this example a segment length Δt of 10 s for the estimation of the spline correction functions,

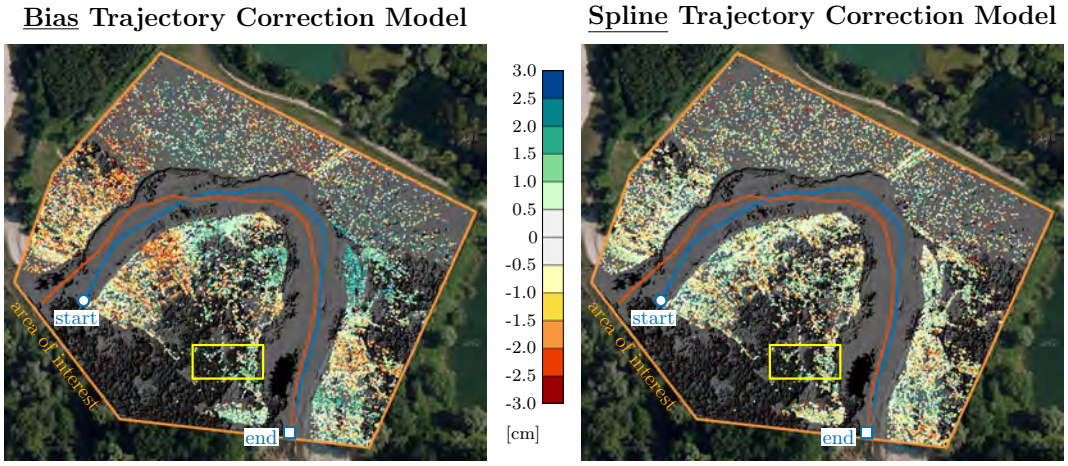

Figure 4.12: Residual point-to-plane distance for each STR-to-STR correspondence after strip adjustment (total no. of correspondences ≈ 29000). A systematic pattern of the residuals can be recognized for the simple *Bias Trajectory Correction Model*. These systematic errors are eliminated to a large extent by using the *Spline Trajectory Correction Model* presented in this article.

which leads to 10 segments for strip 1 and 11 segments for strip 2 (Figure 4.15). By using this correction model, the relative orientation of the strips – defined as std. dev. of the residual point-to-plane distances for all STR-to-STR correspondences, cf. Table 4.5 – was improved by 25%, i.e. from 1.83 cm to 1.38 cm. Accordingly, the absolute orientation of the strips was improved by 10%, i.e. from 1.82 cm to 1.65 cm. A comparison with Table 4.4 shows that these values, as well as the estimated correction functions are widely in conformity with the accuracies declared by the manufacturers.

An appropriate choice of the segment length Δt is of great importance. On the one hand, a too small segment length increases the model complexity without improving significantly the goodness of fit of the model. As can be seen in Figure 4.14, this applies to Δt <10 s in the current case. On the other hand, *systematic* errors of the trajectory can not be fully compensated if the segment length is too long. Thus, a good balance between goodness of fit and the complexity of the model – i.e. the no. of unknown parameters – has to be found. Several statistical tests can be applied to this purpose, e.g. the Akaike Information Criterion (AIC) or Minimum Description Length (MDL) tests (Burnham and Anderson, 2002). In this example, a good trade-off was found for Δt =10 s.

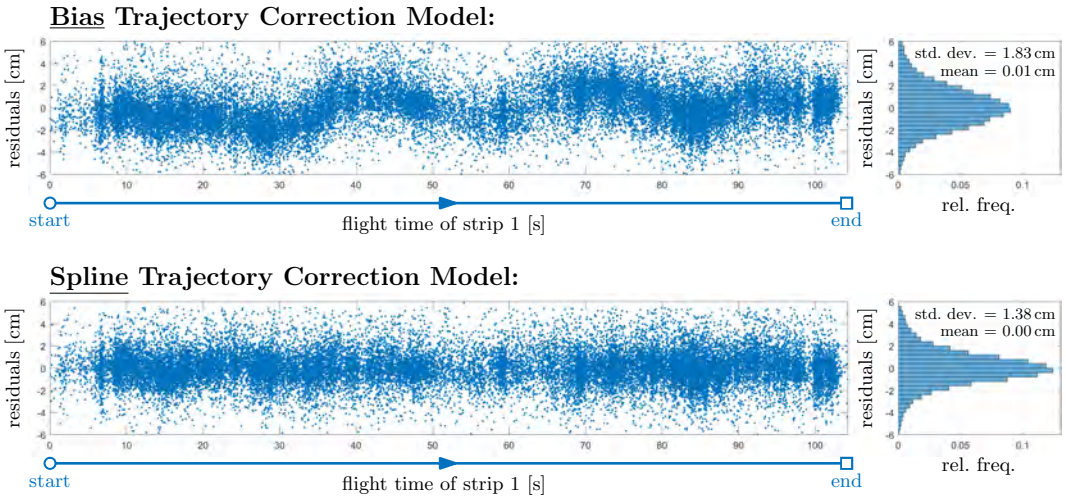

Figure 4.13: Residual point-to-plane distance for each STR-to-STR correspondence after strip adjustment depending on the flight time of strip 1. *Bias Trajectory Correction Model*: the systematic error pattern in object space (cf. Figure 4.12, left) is also clearly visible in time domain. *Spline Trajectory Correction Model*: the residuals are predominantly random distributed, i.e. systematic errors are minimized by the estimated spline functions (cf. Figure 4.15).

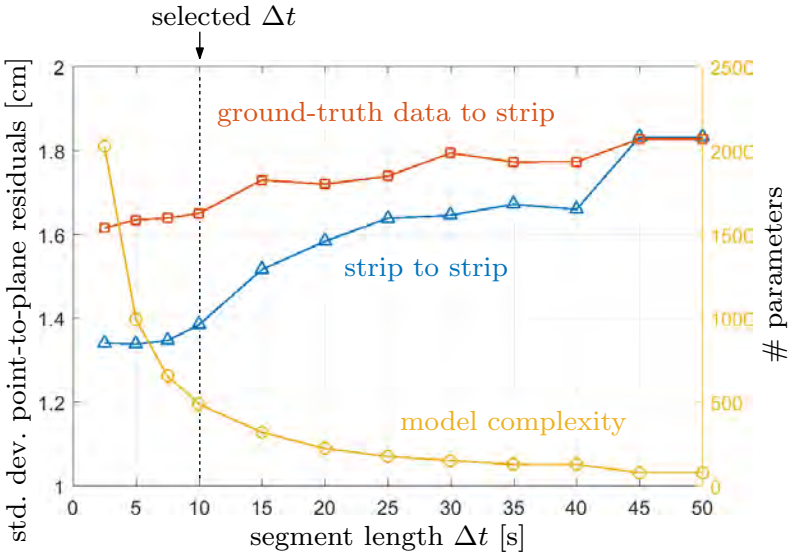

Figure 4.14: Goodness of fit vs. model complexity for different segment lengths Δt.

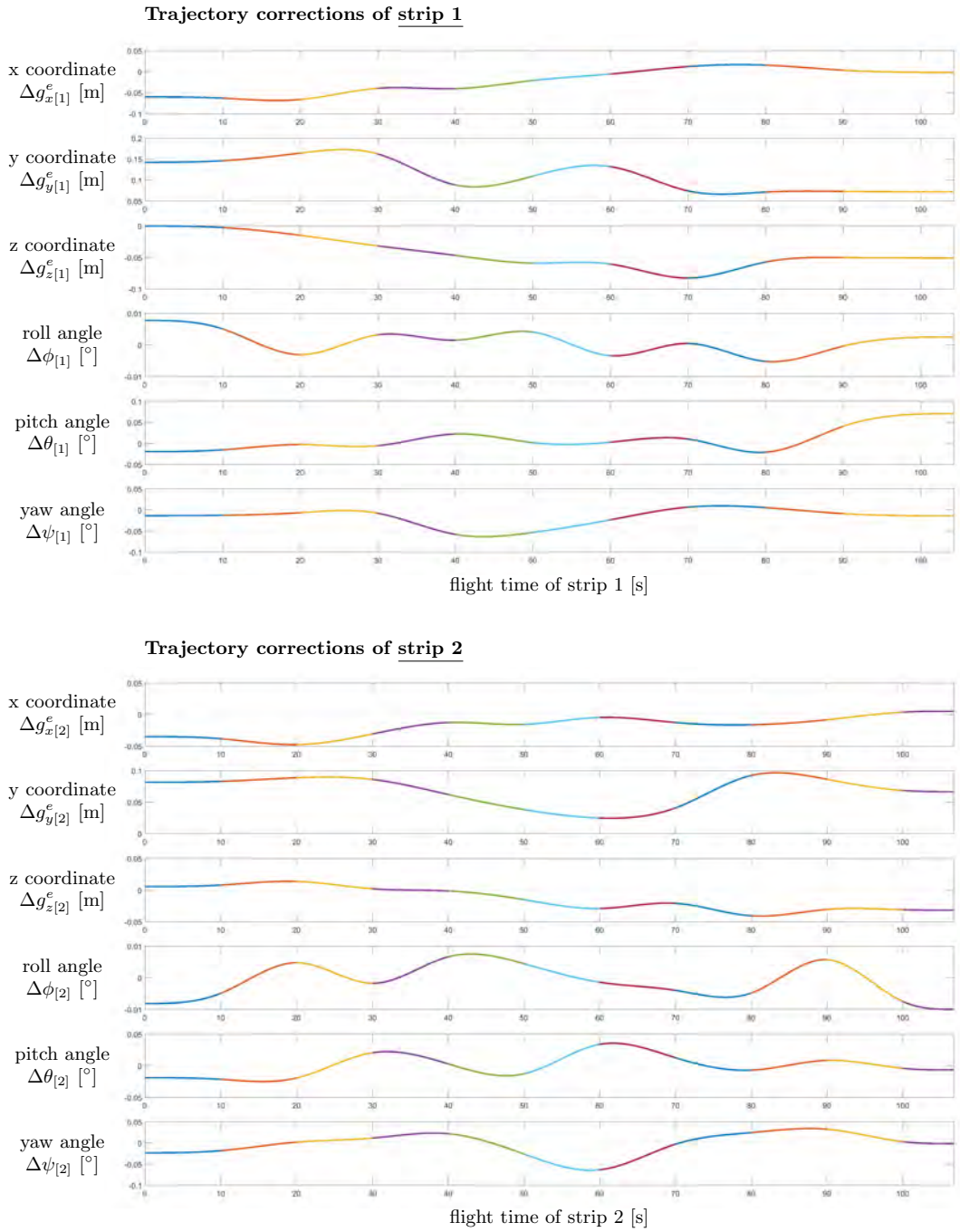

Figure 4.15: Estimated trajectory correction functions for both strips.

4.4 Hybrid adjustment of high resolution lidar and image data

The aim of this example is to show the potential of the hybrid adjustment for terrain modeling on the basis of high-resolution data captured by UAVs. It is demonstrated that using the method presented herein, lidar and image data can be simultaneously georeferenced with a relative precision of 1 cm (std. dev.). In our experience, this level of accuracy can only be achieved by a thorough and *simultaneous* calibration of all sensors, i.e. of the lidar scanner, the camera(s), GNSS, and INS. It is noted, that preliminary results from the same flight campaign have been published by Cramer et al. (2018). Thereby, the lidar point clouds have been adjusted by the strip adjustment method presented in this work.

The study area is located in Hessigheim, Germany, (48°59'67" N, 9°11'20" E; WGS 84), cf. Figure 4.16. The lidar data was collected by a Riegl RiCopter UAV and the Riegl VUX-1LR scanner (Figure 4.18). The mean point density within a lidar strip is $\approx 350\,\text{points/m}^2$. As GNSS-inertial solution an Applanix APX-20 board was used. The accuracy of the post-processed flight trajectory is 2–5 cm for the position coordinates, 0.015° for the roll and pitch angles, and 0.035° for the yaw angle. The data was collected in a flying height of about 40 m above ground and a flying speed of about 8 m/s. Oblique imagery with an average GSD of 20 mm was captured from two Sony Alpha 6000 cameras together with the lidar data. As precise time stamps are available for these images, they are handled as *coupled images* in the adjustment. A second flight campaign with the CopterSystems CS-SQ8 copter and a PhaseOne iXU-RS 1000 camera was carried out for the acquisition of high-resolution nadir images with an average GSD of 4 mm and 80/60 overlap. Due to inaccurate time stamps, these images are introduced as *loose images* into the adjustment. Ground truth data was measured by a combination of GNSS static baseline and tacheometry measurements (Figure 4.17). The accuracy of the thereby measured points is between 2 and 4 mm. As control point clouds (CPC) gable roof shaped structures, fixed on tripods, are used. A dense point cloud was derived from the observed corner points of these structures. Checkerboard targets with a diameter of 27 cm are used as ground truth data for the aerial images. These points were either used as ground control points (GCP) or as check points (CP) in the following experiments. In sum, 4 longitudinal lidar strips, 506 oblique images (coupled images), and 76 nadir images (loose images) have been chosen for this example to demonstrate the capabilities of the hybrid adjustment.

Computation parameters The following provides a detailed summary of the computation parameters used in the hybrid adjustment:

- **Lidar**: For the alignment of the lidar point clouds only the last echoes within a scan angle of ±35° are used. As no initial mounting calibration was provided, the scanner coordinate system (s-system) is initially aligned with the INS coordinate system (i-system). Thus, the mounting calibration parameters of the scanner ($R_s^i, \mathbf{a}^i$) and a subset of the scanner calibration parameters (range offset $\Delta\rho$, range scale ε_ρ, and scan angle scale ε_α) are estimated by adjustment. The planes used to establish the correspondences involving lidar data (STR-to-STR, IMG-to-STR, CPC-to-STR) are estimated from points within a search

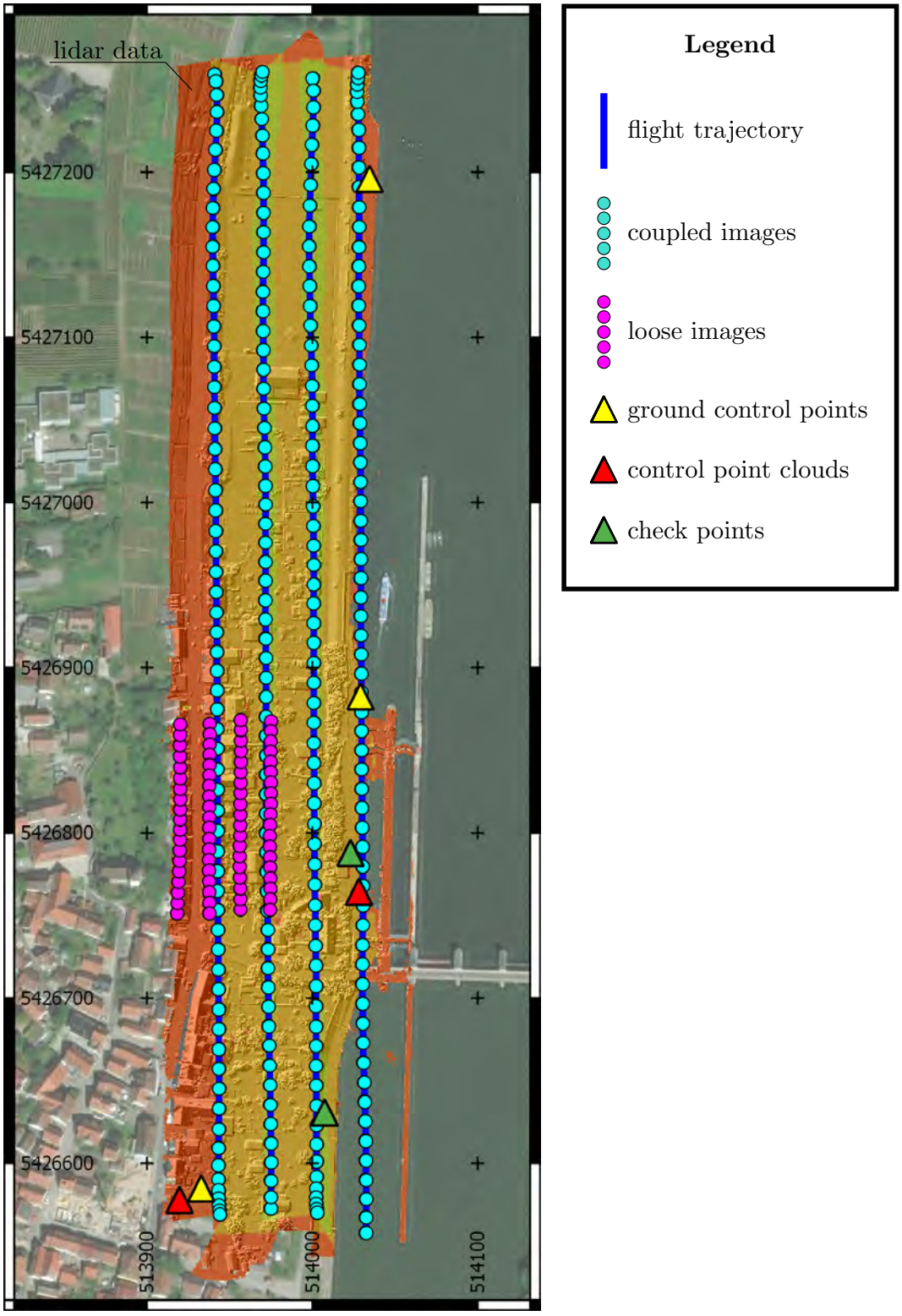

Figure 4.16: Overview of the data used in the final version of the hybrid adjustment (experiment no. 7). The area covered by the lidar data is colored according to the strip overlap.

ground control points and check points

control point clouds

Figure 4.17: Ground-truth-data for images and lidar. On the right, the alignment of the lidar points (orange) and the control point cloud (blue) is shown after the hybrid adjustment.

Figure 4.18: UAVs used for data capturing. Left: Riegl RiCopter with VUX-1LR scanner and two Sony Alpha 6000 cameras. Right: CopterSystems CS-SQ8 copter with PhaseOne iXU-RS 1000 camera.

radius of 0.50 m, whereby a plane is only used if at least 15 points are found within the sphere defined by this search radius.

- **Images**: A distinction must be made here between the oblique images of the two Sony Alpha 6000 cameras and the nadir images of the PhaseOne iXU-RS 1000 camera. As the images of the Sony cameras are coupled to the flight trajectory, the mounting calibration parameters are estimated for these two cameras ($R^i_{c[1]}, R^i_{c[2]}, \mathbf{a}^i_{[1]}, \mathbf{a}^i_{[2]}$). Additional correction parameters of the six parameters of the exterior orientation ($\Delta X^e_{0[i]}, \Delta Y^e_{0[i]}, \Delta Z^e_{0[i]}, \Delta\omega_{[i]}, \Delta\varphi_{[i]}, \Delta\kappa_{[i]}$) are estimated for each image $[i]$. These correction parameters are (fictionally) observed to zero with an a priori precision that corresponds to the above reported precision of the flight trajectory. These observations honor the zero-expectation of these parameters and maintain the coupling of the cameras to the flight trajectory, cf. section 3.1.2. In contrast, the images of the PhaseOne camera are treated as loose images, i.e. the initial six parameters of the exterior orientation are free to change, i.e. not coupled to a flight trajectory and not observed through fictional observations. The camera calibration parameters of all three cameras are estimated by adjustment, including the image distortion parameters. The a priori precision of the image measurements was set for all cameras to 0.5 px.

- **Trajectory**: After using the *Bias Trajectory Correction Model* the quality control of the lidar strips showed systematic time-dependent residuals (we will address this point in experiment no. 4 later on). Thus, the *Spline Trajectory Correction Model* is applied to correct these errors. Thereby, a segment length Δt of 5 s is used. The 0-degree polynomial coefficients of the spline function are fictionally observed to zero, again according to the above reported precision of the flight trajectory. A single set of datum correction parameters (Δg_x^e, Δg_y^e, Δg_z^e) is used to correct for a global shift of the entire lidar and image block.

- **Ground truth data**: Within the used image block, five points, used either as ground control points or check points, are available. The a priori precision of these points is assumed to be 4 mm. Only two control point clouds are present in the southern part of the block. This suboptimal distribution was chosen intentionally to highlight some of the risks and benefits of the hybrid adjustment concerning an absolute deformation of the lidar and image block. For the CPC-to-STR correspondences the planes are estimated from the control point clouds with a search radius of 5 cm, where a minimum of 5 points are needed.

- **Correspondences**: The STR-to-STR correspondences are selected in two steps. First, points are selected with the *Uniform Sampling* strategy with a mean sampling distance of 1 m. Then, a subset of 50% of these points is selected by the *Normal Space Sampling* strategy. Correspondences with a roughness $\sigma_p > 2$ cm and with an angle of $\alpha > 5°$ between the normals of corresponding points are rejected. For the IMG-to-IMG correspondences only points depicted in at least 3 images are used. As IMG-to-STR correspondences a subset of these tie points was selected with the *Uniform Sampling* strategy using a mean sampling distance of 2 m. All correspondences with roughness $\sigma_p > 2$ cm are rejected, cf. Figure 3.17.

- **General**: The correspondences have been re-established in five iterations. In order to identify wrong correspondences (outliers) a l_1-norm minimization is imitated within the adjustment by iteratively re-weighting the observations (Kraus, 1997, p. 218). After the removal of the detected outliers, a final regular least squares adjustment is performed with the remaining correspondences (inliers).

In the following, a series of 7 experiments, in which we gradually increase the complexity by adding new parameters and new input data, will be described to explain the different aspects of the hybrid adjustment. An overview showing the input data, the observations, and the chosen parameter model for each experiment can be found in Table 4.6. The results of each experiment are summarized in the Figures 4.21 – 4.27.

Experiments									
experiment no.			**1**	**2**	**3**	**4**	**5**	**6**	**7**
input data		lidar strips	4	4	4	4	4	4	4
		coupled images	—	—	—	—	—	506	506
		loose images	—	—	—	—	—	—	76
		CPCs	2	2	2	2	2	2	2
		GCPs	—	—	—	—	—	—	3
observations	*correspondences*	STR-to-STR	35850	35158	36041	37089	35662	35721	35765
		CPC-to-STR	644	653	654	767	769	769	769
		IMG-to-STR	—	—	—	—	—	14480	15155
		IMG-to-IMG	—	—	—	—	—	169953	186694
		IMG-to-GCP	—	—	—	—	—	—	18
	fictional observations		3	3	3	26	434	3491	3947
parameters	*laser scanner*	mounting calibration	3	6	6	6	6	6	6
		sensor calibration	—	—	3	3	3	3	3
	cameras	camera calibration	—	—	—	—	—	14	21
		mounting calibration	—	—	—	—	—	12	12
	images	coupled images	—	—	—	—	—	3036	3036
		loose images	—	—	—	—	—	—	456
		tie points / GCPs	—	—	—	—	—	147810	160185
	trajectory correction	position and rotation	—	—	—	23	1678	1678	1678
		datum	3	3	3	3	3	3	3
		total =	6	9	12	35	1690	152562	165400

Table 4.6: Overview about the conducted experiments.

Experiment no. 1 We start with the adjustment of the 4 lidar strips only, i.e. without images. The datum of the lidar block is thereby defined by the two control point clouds in the southern part of the block. Only six parameters are estimated in total: the three misalignment angles of the mounting calibration of the scanner and the three datum correction parameters. As pointed out in section 1.3, many of the works previously published on the topic of lidar strip adjustment aim to estimate the three misalignment angles only (e.g. Toth (2002), Hebel and Stilla (2012)), as they have a major impact on the georeference of the lidar strips. However, large residual errors are still observable after the adjustment within the overlap area of neighboring lidar strips. These errors are visualized in the upper left image of Figure 4.21 (*relative orientation between lidar strips*). We use this mosaic to check the relative orientation between overlapping lidar strips. To generate this mosaic, first a DSM is derived from each lidar strip. Thereby, a mask, marking only the smooth parts (e.g. streets, roofs) of the observed area, is also generated. The height differences between overlapping lidar strips are then calculated for each overlapping strip pair, whereby only smooth areas are considered (Ressl et al., 2008). The final mosaic is derived from these strip height differences by choosing at each grid point the height difference with the maximum absolute value. Due to imperfections of the above mentioned smoothness masks, robust estimators are used to describe the distribution of these residual errors. The median and σ_{mad} values of these errors are 1.8 ± 3.9,cm for the current experiment. In the upper right image of Figure 4.21 (*height differences of lidar block to final version*) the height difference of the adjusted lidar block is shown with respect to the final version of the adjustment, i.e. experiment no. 7, which is assumed to be the optimal solution. Here, one can see that differences are small at the position of the control point clouds, however, towards north differences are steadily increasing. The a posteriori statistics in the lower part of Figure 4.21 show the number and distribution of the established correspondences (top) and the residuals at the GCPs and check points (CPs) (bottom). Summarizing, the relative and absolute orientation of the lidar strips is far from satisfactory for this experiment. We will try to improve the results by extending the parameter model in the subsequent experiments.

Experiment no. 2 In this experiment, the full set of mounting calibration parameters is estimated for the scanner, i.e. the three lever-arm components are added to the parameter model with respect to the previous experiment. We can see in Figure 4.22 that the residuals slightly improve for both, the relative and absolute orientation of the lidar strips. However, still very large residual systematic discrepancies can be observed.

Experiment no. 3 In this experiment, the three scanner calibration parameters, used to correct the polar measurements of the scanner, are estimated additionally. Again, the relative and absolute orientation of the lidar strips can be slightly improved, but residuals are still very large and show a strong bias (Figure 4.23).

Experiment no. 4 The first three experiments showed large systematic residual errors, especially due to the inability of the individual lidar strips to be moved and rotated in object space. In this experiment the *Bias Trajectory Correction Model* is additionally used to individually correct the flight trajectory of each lidar strip.

Thereby, the relative orientation of the lidar strips can be significantly improved from 2.1 ± 3.2,cm to 0.1 ± 1.0 cm (Figure 4.24). Such a level of accuracy is acceptable for most applications. However, locally, still errors with a magnitude of up to 2–3 cm can be recognized in the upper left image; we will try to mitigate these errors in the next experiment. The upper right image and the a posteriori statistics show that the lidar block fits very well to the two control point clouds. However, height differences grow towards north due to lack of ground truth data.

Experiment no. 5 This experiment shows that using the *Spline Trajectory Correction Model*, systematic discrepancies between overlapping lidar strips can widely be eliminated (Figure 4.25). The residual height differences are within ± 1 cm almost over the entire lidar block, having a distribution of 0.0 ± 0.4 cm. However, as pointed out in section 3.1.4.1, the usage of splines for the correction of the flight trajectory elements, involves also some risks, especially if the ground truth data is not well distributed over the boundaries of the block. The latter applies to the current experiment, where control point clouds are situated in the southern part of the block only. Thus, it can be observed, that the quality of the absolute orientation of the lidar block decreases toward north, showing a maximum discrepancy of approximately -10 cm at the northernmost point.

Experiment no. 6 The hybrid adjustment of lidar and image data is first carried out in this experiment. It is noted, that no ground truth data was used as GCPs for the images here, i.e. all points are used as check points only. In the upper central image of Figure 4.26 (*relative orientation between images and lidar strips*) the residual point-to-plane distances of the IMG-to-STR correspondences are shown. No systematic patterns of the residual errors can be recognized here. The mean and standard deviation of these residuals are 0.00 ± 0.6 cm, i.e. the lidar block and the image block are well aligned to each other. In the top right image it can be seen that the absolute discrepancies can be strongly mitigated by the incorporation of aerial images, but the maximum discrepancy is still approximately -4 cm at the northernmost point due to missing ground truth data in this region. However, most important, the images avoid through the incorporation of additional geometric constraints an overcompensation of the flight trajectory errors. This is considered as one of the main benefits of the hybrid adjustment, as it allows to use the *Spline Trajectory Correction Model* without the risk of causing unmotivated local block deformations. As an example, the trajectory corrections for a single strip are depicted in Figure 4.19. Using the lidar data only, the correction functions oscillate to a relatively high degree. However, by supporting the estimation of the trajectory correction functions with the coupled images, the oscillation can be mitigated. The main reason for this is that a single image, which is recorded at a single point in time, covers a relatively large area on the ground. This is not the case in lidar, where at a single point in time only a few ground points (when using multi-echo scanners) are generated. Thus, the stability of the lidar *and* image strip can be strongly increased through the incorporation of images, making strong local deformations more unlikely. The stability of the strips is thereby correlated with the area covered by a single image and the overlap of the images. Another important synergetic effect of the hybrid adjustment is shown in Figure 4.20. Here, the estimated precision $\sigma_{\hat{x}}$ of some parameters is shown for experiment no. 5 and 6, i.e. for the adjustment without

and with aerial images. As it can be seen, the determinability of the parameters increases by adding the aerial images to the adjustment due to a higher redundancy and due to additional geometric constraints newly added through the images. From the a posteriori statistics it can be seen that the residuals at the five check points are within ±3 cm. This is in line with the expected theoretical reconstruction errors of the coupled images (GSD = 20 mm), being $\sigma_Z = 3.4$ cm and $\sigma_{XY} = 0.8$ cm.

Experiment no. 7 This is the final version of the hybrid adjustment, in which all the available data and the most comprehensive parameter model is used. Compared to the previous experiment, three GCPs are used additionally for the datum definition, so that the ground truth data is well distributed from south to north. Moreover, the loose images of the PhaseOne camera are added to the adjustment. The spatial distribution of the correspondences established in object space is shown in Figure 4.28. The quality control of the adjustment reveals a good relative and absolute alignment of the lidar and image data (Figure 4.27). The appropriateness of the functional model of the adjustment is confirmed by the random character of the residual errors. The newly added PhaseOne images with a GSD of 4 mm have been used to generate a dense image matching (DIM) point cloud. A comparison between this point cloud and the lidar point cloud can be seen in Figure 1.2 and 4.29.

Conclusions In this example the benefits of an integrated orientation of lidar strips and aerial images have been shown. The major advantage is the direct optimization of the relative orientation between lidar and image data. However, it was shown that the hybrid adjustment has other synergetic effects as well. The estimation of time-dependent trajectory errors using the *Spline Trajectory Correction Model* strongly benefits from the integration, mainly due to an increased geometric stability of the strips and due to the higher redundancy. In this context, also an absolute deformation of the block can be mitigated in case of an unfavorable distribution of the ground truth data. Moreover, it was shown that the determinability of the parameters increases by the simultaneous adjustment of lidar and image data. This is especially useful when estimated calibration parameters should be transferred to other flight campaigns.

Acknowledgements The data for this example was kindly provided by Institute for Photogrammetry of the University of Stuttgart. This is highly appreciated.

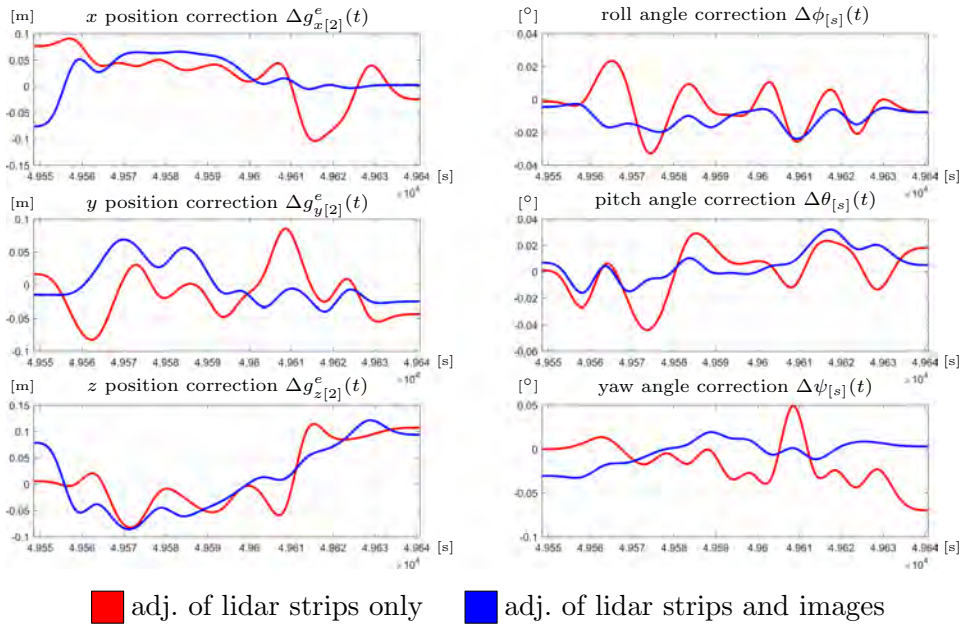

Figure 4.19: Comparison of spline trajectory corrections for strip no. 2 between lidar strip adjustment (experiment no. 5) and hybrid adjustment (experiment no. 6).

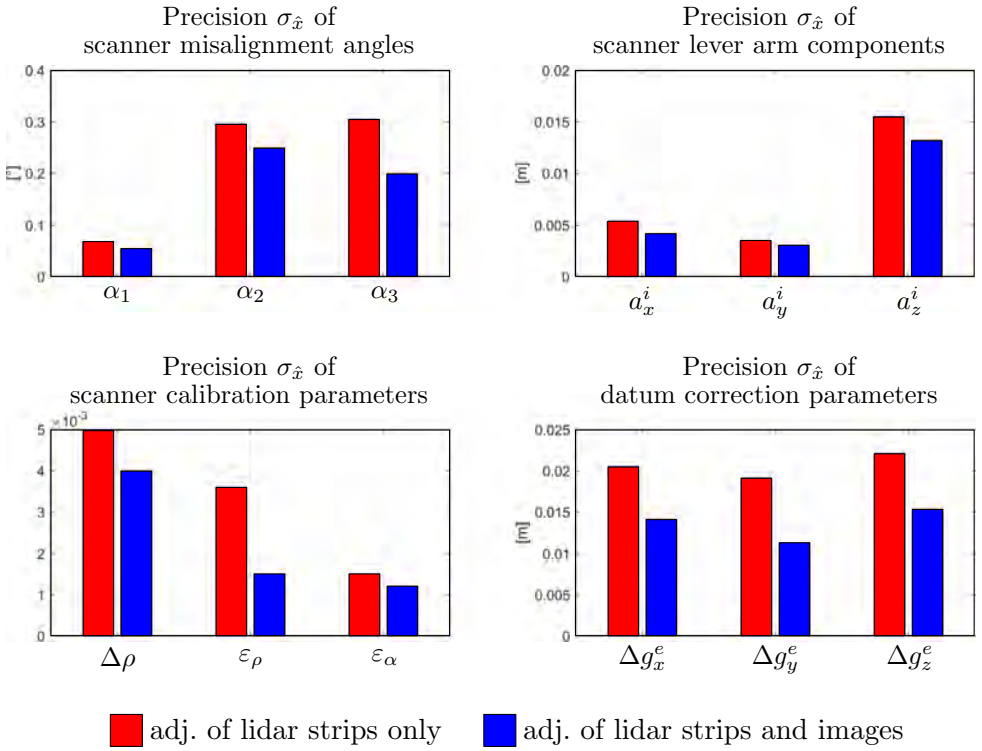

Figure 4.20: Comparison of a posteriori precisions of estimated parameters between lidar strip adjustment (experiment no. 5) and hybrid adjustment (experiment no. 6).

Quality control of experiment no. 1

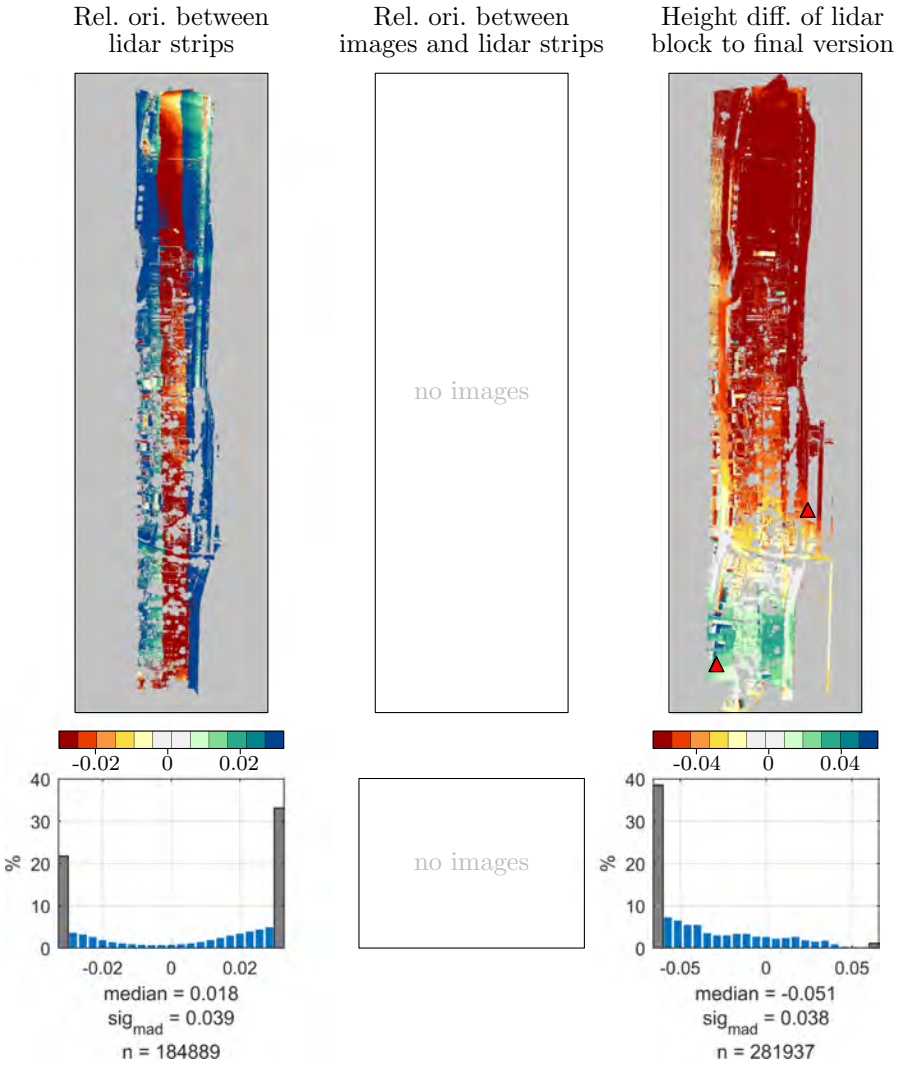

A posteriori statistics

correspondences	unit	n	mean	σ	
STR-to-STR residuals	[m]	35850	0.006	0.033	
CPC-to-STR residuals	[m]	644	0.000	0.015	
IMG-to-IMG residuals x/y (cam1)	[px]	0	—/—	—/—	
IMG-to-IMG residuals x/y (cam2)	[px]	0	—/—	—/—	
IMG-to-IMG residuals x/y (cam3)	[px]	0	—/—	—/—	
IMG-to-STR residuals	[m]	0	—	—	
GCPs and control points (CPs)			**mean**	**min**	**max**
GCP residuals x/y	[m]	0	—/—	—/—	—/—
GCP residuals z	[m]	0	—	—	—
CP residuals x/y	[m]	0	—/—	—/—	—/—
CP residuals z	[m]	0	—	—	—

Figure 4.21: Quality control of experiment no. 1.

Quality control of experiment no. 2

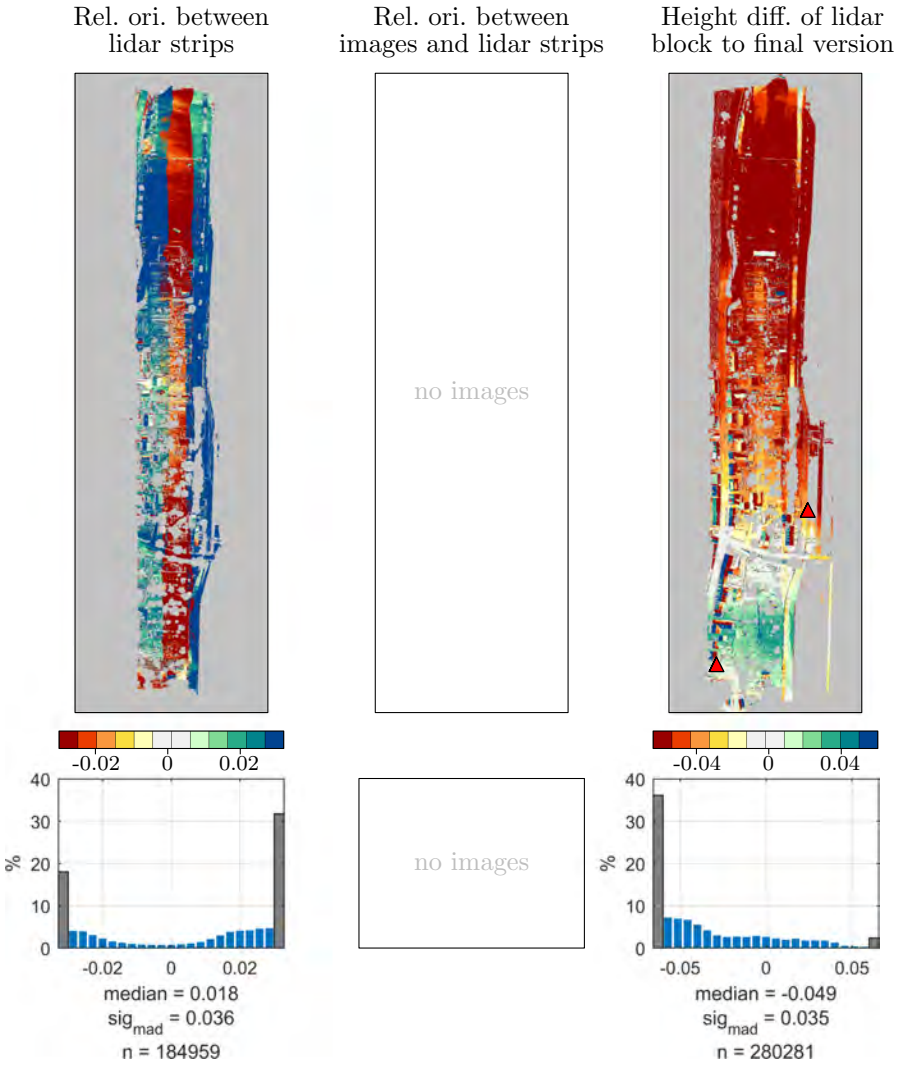

A posteriori statistics

correspondences	unit	n	mean	σ	
STR-to-STR residuals	[m]	35158	0.005	0.028	
CPC-to-STR residuals	[m]	653	0.000	0.008	
IMG-to-IMG residuals x/y (cam1)	[px]	0	—/—	—/—	
IMG-to-IMG residuals x/y (cam2)	[px]	0	—/—	—/—	
IMG-to-IMG residuals x/y (cam3)	[px]	0	—/—	—/—	
IMG-to-STR residuals	[m]	0	—	—	
GCPs and control points (CPs)			**mean**	**min**	**max**
GCP residuals x/y	[m]	0	—/—	—/—	—/—
GCP residuals z	[m]	0	—	—	—
CP residuals x/y	[m]	0	—/—	—/—	—/—
CP residuals z	[m]	0	—	—	—

Figure 4.22: Quality control of experiment no. 2.

Quality control of experiment no. 3

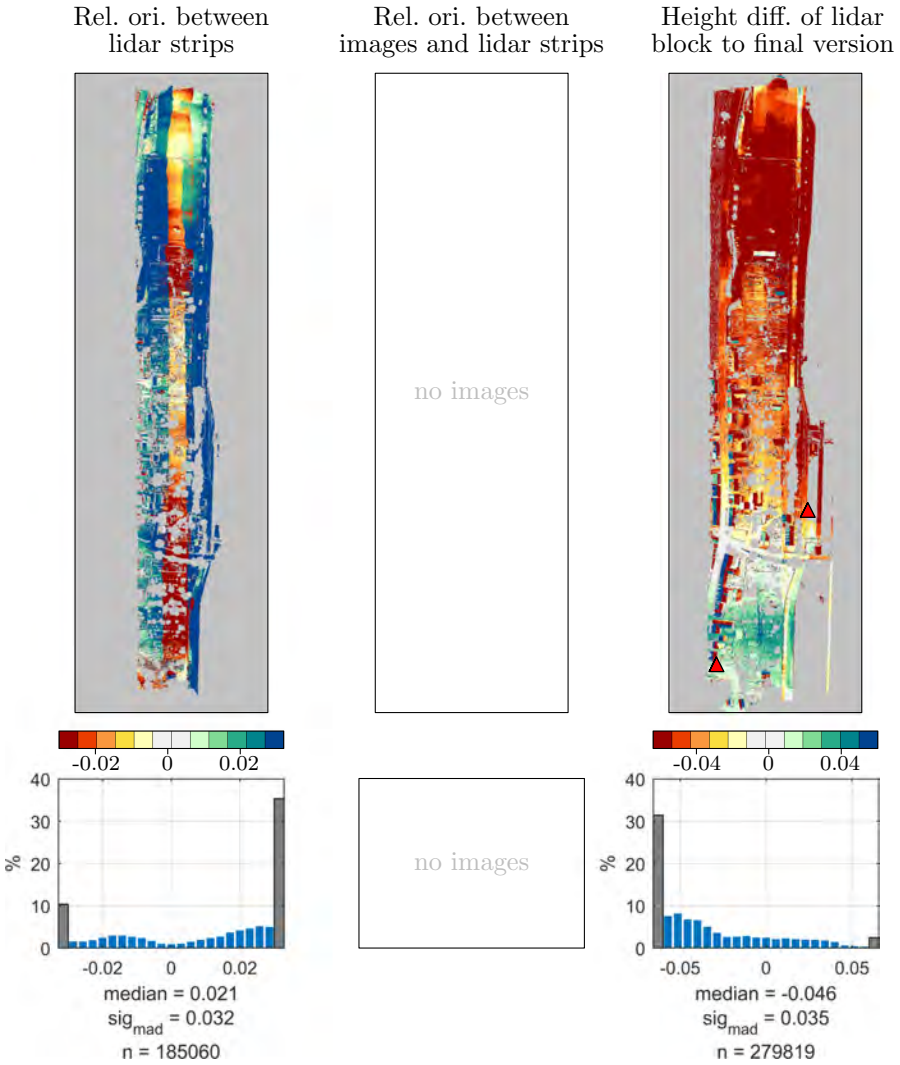

A posteriori statistics

correspondences	unit	n	mean	σ	
STR-to-STR residuals	[m]	36041	0.008	0.027	
CPC-to-STR residuals	[m]	654	0.000	0.010	
IMG-to-IMG residuals x/y (cam1)	[px]	0	—/—	—/—	
IMG-to-IMG residuals x/y (cam2)	[px]	0	—/—	—/—	
IMG-to-IMG residuals x/y (cam3)	[px]	0	—/—	—/—	
IMG-to-STR residuals	[m]	0	—	—	
GCPs and control points (CPs)			**mean**	**min**	**max**
GCP residuals x/y	[m]	0	—/—	—/—	—/—
GCP residuals z	[m]	0	—	—	—
CP residuals x/y	[m]	0	—/—	—/—	—/—
CP residuals z	[m]	0	—	—	—

Figure 4.23: Quality control of experiment no. 3.

Quality control of experiment no. 4

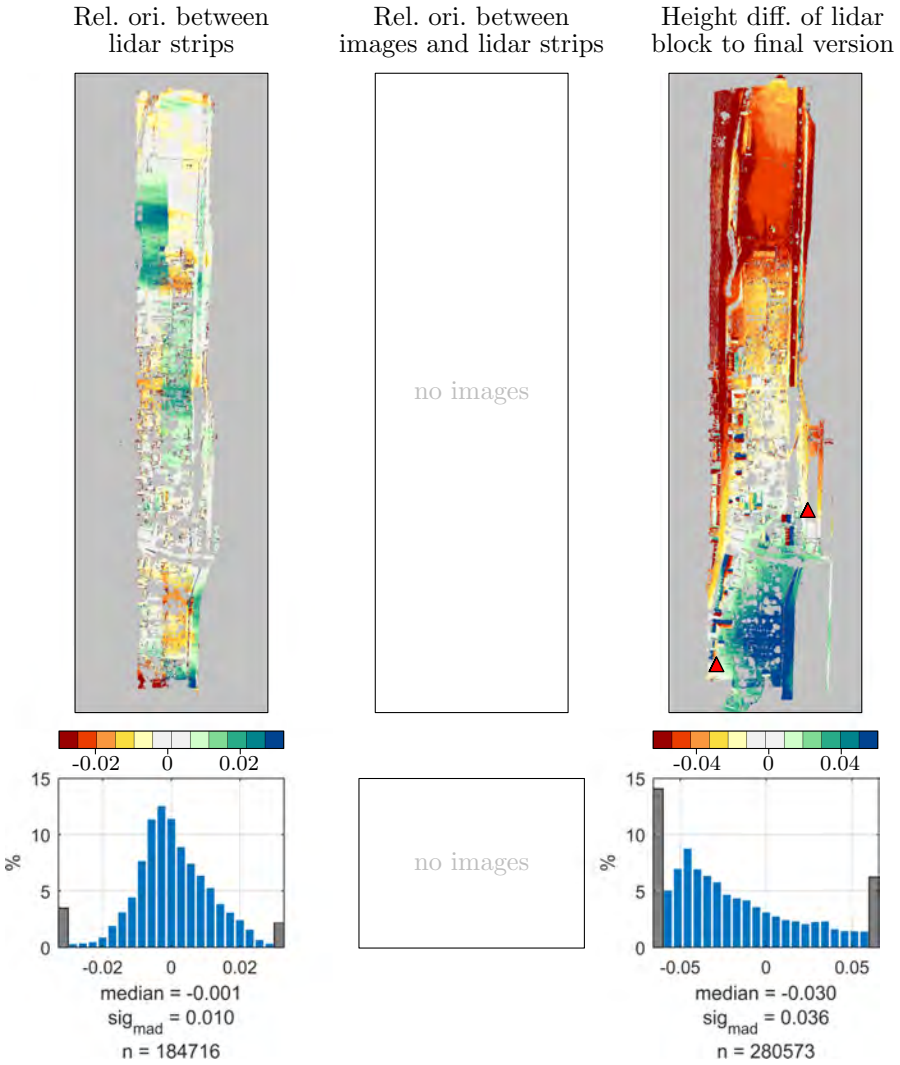

A posteriori statistics

correspondences	unit	n	mean	σ	
STR-to-STR residuals	[m]	37089	0.000	0.013	
CPC-to-STR residuals	[m]	767	0.000	0.005	
IMG-to-IMG residuals x/y (cam1)	[px]	0	—/—	—/—	
IMG-to-IMG residuals x/y (cam2)	[px]	0	—/—	—/—	
IMG-to-IMG residuals x/y (cam3)	[px]	0	—/—	—/—	
IMG-to-STR residuals	[m]	0	—	—	
GCPs and control points (CPs)			**mean**	**min**	**max**
GCP residuals x/y	[m]	0	—/—	—/—	—/—
GCP residuals z	[m]	0	—	—	—
CP residuals x/y	[m]	0	—/—	—/—	—/—
CP residuals z	[m]	0	—	—	—

Figure 4.24: Quality control of experiment no. 4.

Quality control of experiment no. 5

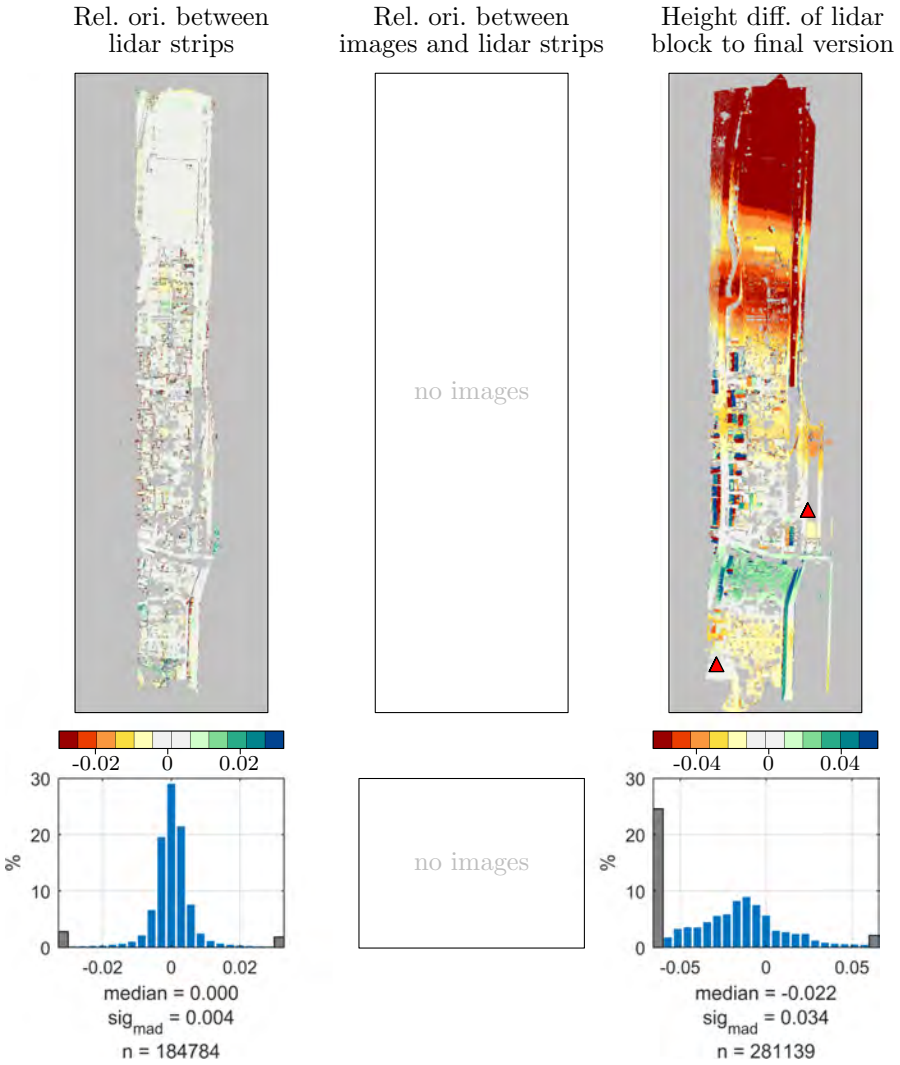

A posteriori statistics

correspondences	unit	n	mean	σ	
STR-to-STR residuals	[m]	35662	0.000	0.009	
CPC-to-STR residuals	[m]	769	0.000	0.004	
IMG-to-IMG residuals x/y (cam1)	[px]	0	—/—	—/—	
IMG-to-IMG residuals x/y (cam2)	[px]	0	—/—	—/—	
IMG-to-IMG residuals x/y (cam3)	[px]	0	—/—	—/—	
IMG-to-STR residuals	[m]	0	—	—	
GCPs and control points (CPs)			**mean**	**min**	**max**
GCP residuals x/y	[m]	0	—/—	—/—	—/—
GCP residuals z	[m]	0	—	—	—
CP residuals x/y	[m]	0	—/—	—/—	—/—
CP residuals z	[m]	0	—	—	—

Figure 4.25: Quality control of experiment no. 5.

Quality control of experiment no. 6

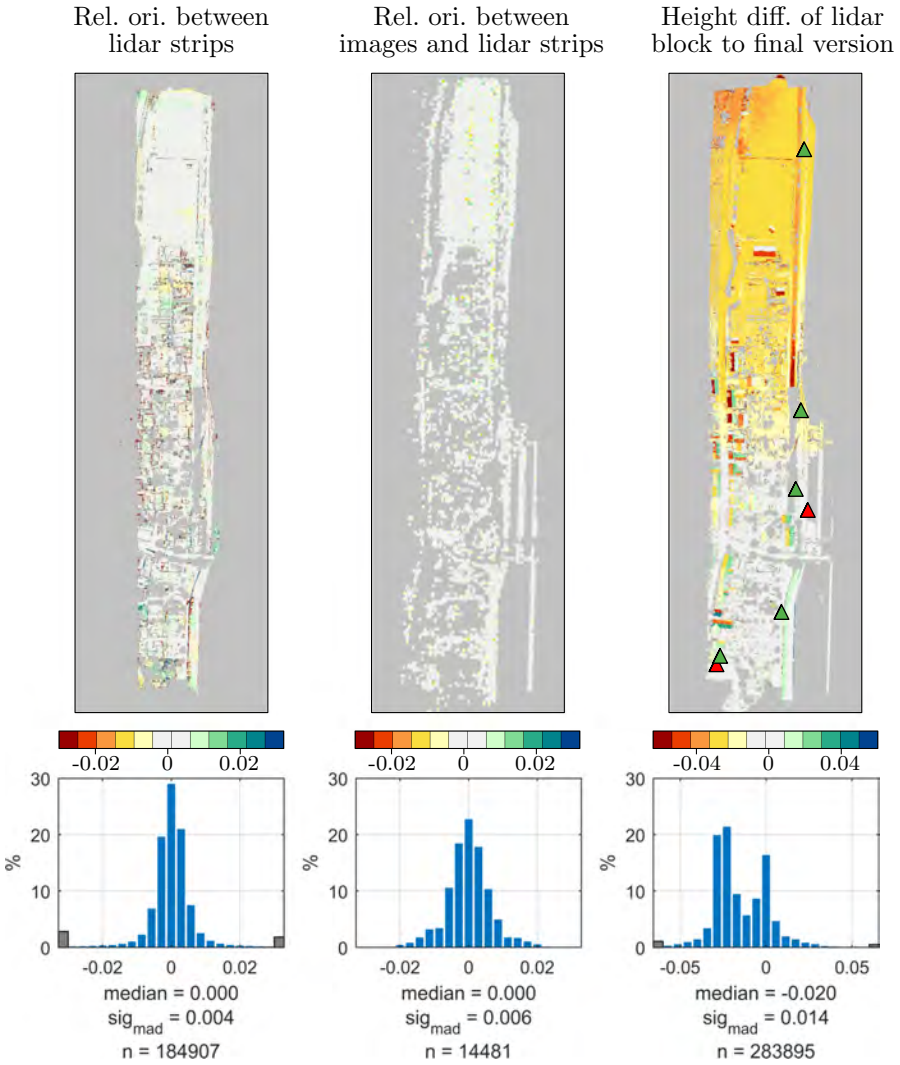

A posteriori statistics

correspondences	unit	n	mean	σ	
STR-to-STR residuals	[m]	35721	0.000	0.009	
CPC-to-STR residuals	[m]	769	0.000	0.004	
IMG-to-IMG residuals x/y (cam1)	[px]	96193	0.00/0.00	0.35/0.35	
IMG-to-IMG residuals x/y (cam2)	[px]	73760	0.00/0.00	0.36/0.34	
IMG-to-IMG residuals x/y (cam3)	[px]	0	—/—	—/—	
IMG-to-STR residuals	[m]	14480	0.000	0.006	
GCPs and control points (CPs)			**mean**	**min**	**max**
GCP residuals x/y	[m]	0	—/—	—/—	—/—
GCP residuals z	[m]	0	—	—	—
CP residuals x/y	[m]	5	-0.016/0.006	-0.017/-0.025	0.006/0.026
CP residuals z	[m]	5	0.013	-0.030	0.029

Figure 4.26: Quality control of experiment no. 6.

Quality control of experiment no. 7

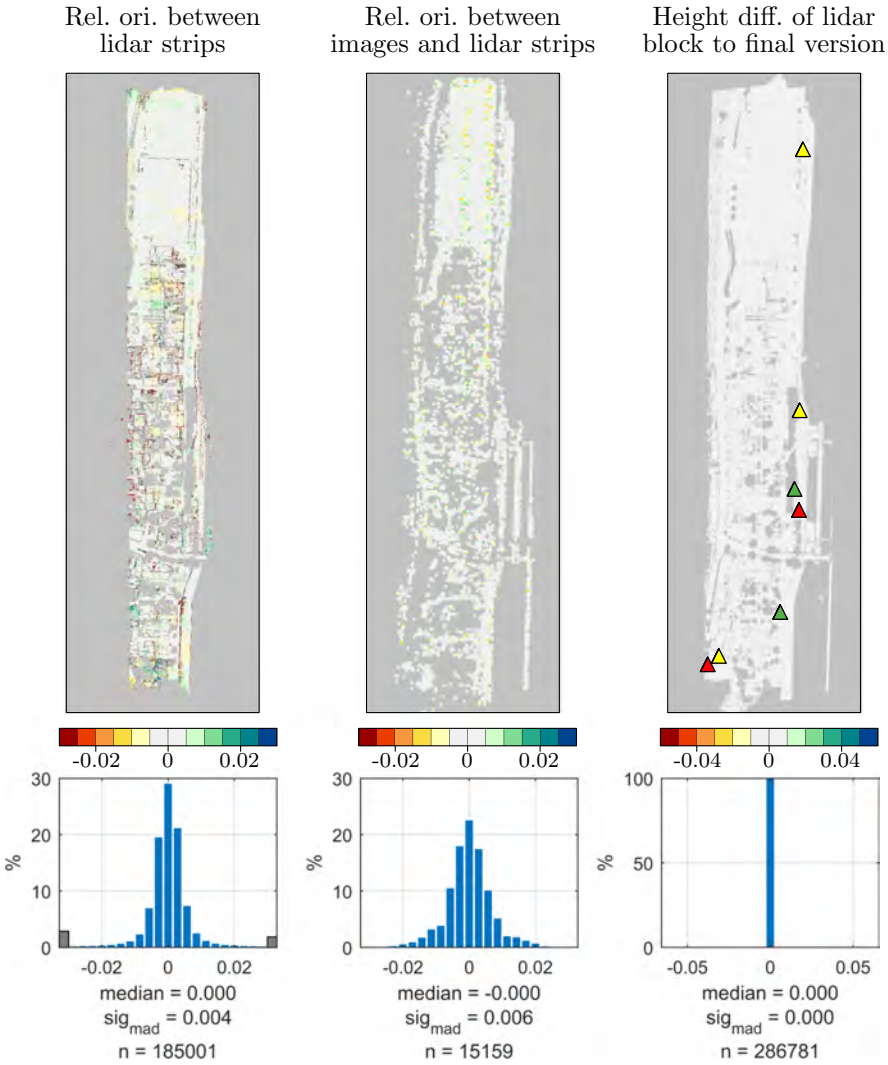

A posteriori statistics

correspondences	unit	n	mean	σ	
STR-to-STR residuals	[m]	35765	0.000	0.009	
CPC-to-STR residuals	[m]	769	0.000	0.004	
IMG-to-IMG residuals x/y (cam1)	[px]	93456	0.00/0.00	0.35/0.35	
IMG-to-IMG residuals x/y (cam2)	[px]	71549	0.00/0.00	0.36/0.34	
IMG-to-IMG residuals x/y (cam3)	[px]	18689	0.00/0.00	0.43/0.35	
IMG-to-STR residuals	[m]	15155	0.000	0.006	
GCPs and control points (CPs)			**mean**	**min**	**max**
GCP residuals x/y	[m]	3	0.003/0.001	-0.002/-0.003	0.008/0.004
GCP residuals z	[m]	3	-0.013	-0.021	0.007
CP residuals x/y	[m]	2	-0.002/0.004	-0.006/0.002	0.003/0.006
CP residuals z	[m]	2	0.018	0.005	0.031

Figure 4.27: Quality control of experiment no. 7.

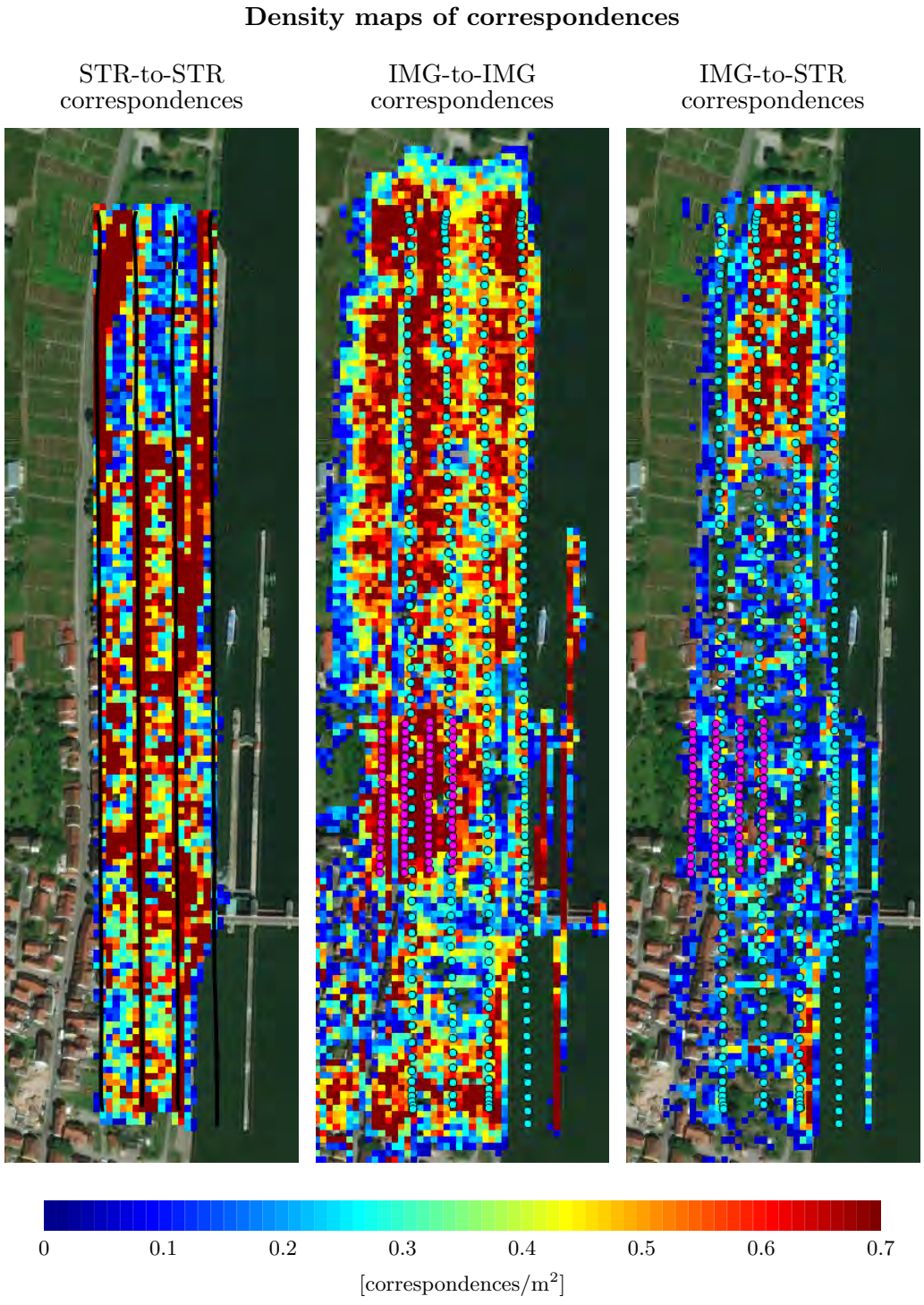

Figure 4.28: Density of correspondences in object space for STR-to-STR, IMG-to-IMG (= tie points), and IMG-to-STR correspondences.

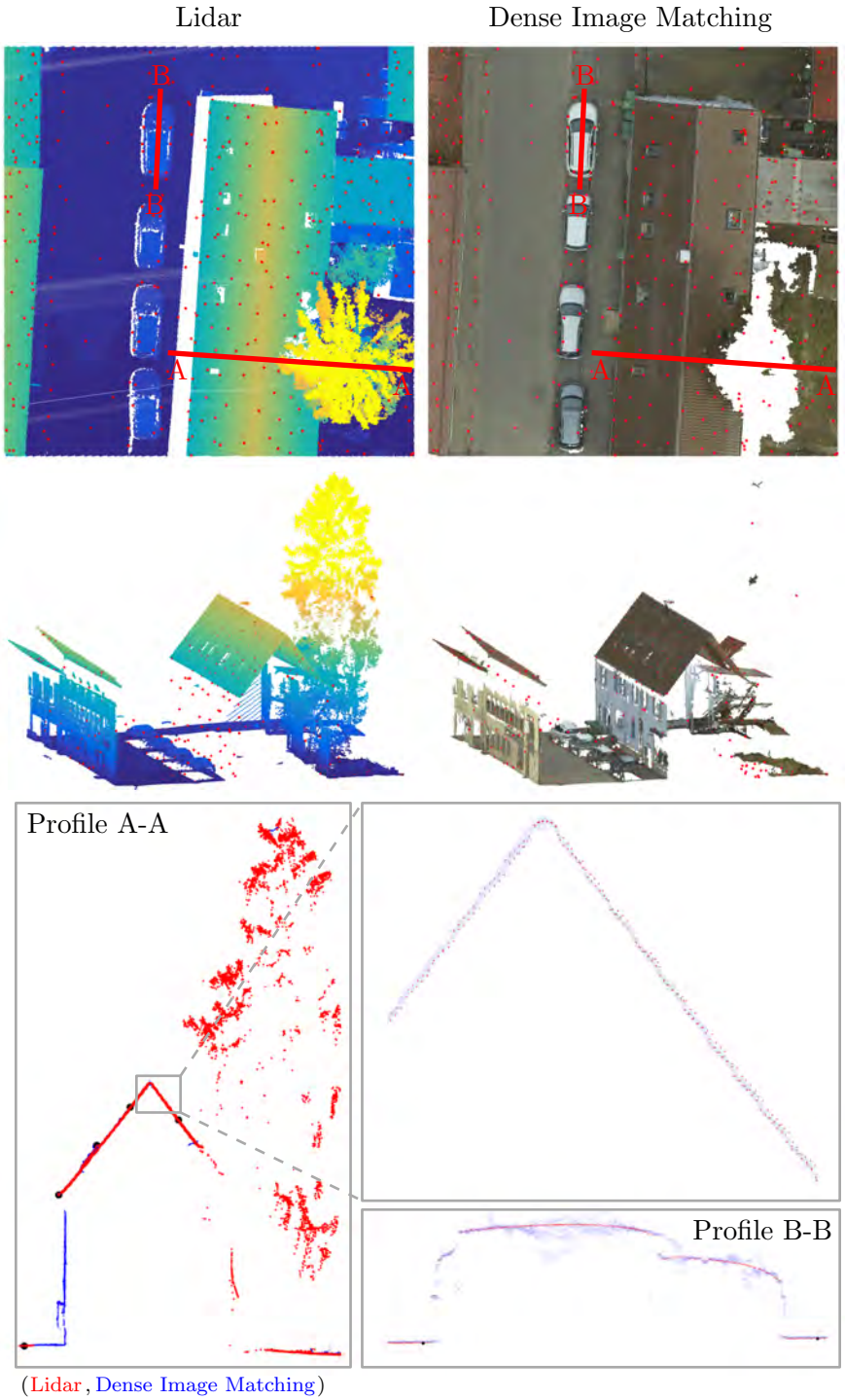

Figure 4.29: Top: Lidar and dense image matching (DIM) point cloud in top view. The image tie points are visualized in as red points. Middle: 3D view. Bottom: Profiles showing the alignment of lidar and image data.

5 Summary and conclusions

Airborne lidar and airborne photogrammetry are both proven techniques for the 3D mapping of the Earth's surface. Both techniques have their own advantages and drawbacks. Airborne lidar typically generates very precise 3D point clouds and has the key ability to penetrate vegetation through small gaps and thereby measure the underlying ground. However, in addition to the laser scanner, expensive (and in former times bulky) GNSS/INS navigation sensors are needed, as the georeferencing accuracy of the generated 3D point clouds strongly depends on the accuracy of the observed flight trajectory. Airborne photogrammetry in turn has the major advantage to capture images at a single point in time that cover large areas and contain spectral information in at least three channels. From these images, very dense and colored point clouds can be derived by means of dense image matching methods (DIM) (Figure 1.2). As the data is not continuously measured (in contrast to lidar), a GNSS/INS navigation system is not strictly mandatory, however, it is mostly used to directly measure the six elements of the exterior orientation of each image. The requirements regarding the accuracy of the flight trajectory are thereby lower compared to lidar systems. The main drawback of the photogrammetric principle is that the reconstruction of a 3D point needs at least two images, which is e.g. rarely the case for points in lower vegetation layers. Due to the complementary strengths of both techniques, many works have been published on the integration of aerial lidar and aerial photogrammetry for the derivation of final products, e.g. true orthophoto, DSM, merging and colorization of point clouds, modeling of buildings. However, this is not the case for the lidar strip adjustment and the aerial triangulation, i.e. for the orientation and calibration of lidar strips and aerial images.

In this thesis a rigorous integration of the lidar strip adjustment and the aerial triangulation, herein denoted as *hybrid adjustment*, was presented (section 3). The main purpose of the hybrid adjustment is to simultaneously optimize the relative and absolute orientation of the lidar and image data. This optimization problem was solved by a least squares adjustment. The methodology of the hybrid adjustment was adapted from the ICP algorithm (section 2). This implies two important aspects: (a) correspondences are established not just once, but in an iterative manner and (b) correspondences are established on a point basis to maintain the highest possible resolution level of the data (instead of using e.g. 2.5D gridded, interpolated data). In total, four types of point clouds are aligned to each other in the hybrid adjustment: lidar strips (STR), image tie points (IMG), control point clouds (CPC), and ground control points (GCP). The point cloud generation process is rigorously modelled within the adjustment for the lidar strips and the image tie points. This means, that not the georeferenced point clouds are used as data input, but the point clouds are modelled by using the original sensor measurements. In case of the lidar strips, the point clouds are generated by combining the original polar measurements of the scanner, the aircraft's flight trajectory, and the mounting calibration parameters of the scanner. The image tie points are modelled in a very similar way, namely by combining the image measurements of homologous points, the aircraft's

flight trajectory, and the mounting calibration parameters of the camera. The flight trajectory is thereby assumed to be estimated in advance by a Kalman filter. The datum (absolute orientation) of the lidar and image block is defined by the remaining two point cloud types: the lidar strips are aligned to the control point clouds and the images are aligned to the ground control points. However, as the lidar and image block are aligned to each other in the hybrid adjustment, both types of ground truth data simultaneously define the datum of the lidar *and* the image block. In consequence, fewer ground truth data is needed in total. This is considered as one of the main benefits of the hybrid adjustment, as time-consuming terrestrial measurements can be reduced.

The functional model of the adjustment is based on three main equations: (a) the lidar direct georeferencing equation (section 3.1.1), (b) the direct georeferencing of images (section 3.1.2), and (c) the collinearity equations (section 3.1.3). These equations establish the relation between the sensor measurements and the points observed in object space. The formulation of this relation through the original sensor measurements, makes it possible to correct the errors where they originally occur. For instance, calibration parameters can be estimated to correct a bias and scale error of the polar measurements of the scanner. This would not be possible if the georeferenced point clouds are used only. Furthermore, the mounting calibration parameters (misalignment angles and lever-arm) of the scanners and the cameras, as well as the camera calibration parameters (including the image distortion parameters), can be estimated. In conclusion, the hybrid adjustment allows the on-the-job calibration of an entire multi-sensor platform by solving a single optimization problem.

The aircraft's flight trajectory plays a central role in the hybrid adjustment. The exterior orientation of the lidar strips *and* the images is derived from the trajectory in consideration of the corresponding mounting calibration parameters. Four different models have been proposed in section 3.1.4 to individually correct each of the six elements (x, y, z, roll, pitch, yaw) of the trajectory in time domain: (a) the *Bias Trajectory Correction Model*, (b) the *Linear Trajectory Correction Model*, (c) the *Quadratic Trajectory Correction Model*, and (d) the *Spline Trajectory Correction Model*. With the latter, being the most flexible model, time-dependent trajectory errors are modelled by natural cubic splines (section 3.1.4.1). Due to the high flexibility of this model, discrepancies between overlapping point clouds can be strongly mitigated. However, if only lidar data is used these correction functions tend to oscillate in some challenging situations (e.g. in absence of ground truth data, or in case of corridor mapping). As a consequence, the lidar block gets locally deformed in these areas, typically with magnitudes of up to 10 cm. It was demonstrated that such deformations can strongly be mitigated by the simultaneous orientation of lidar and image data. This is mainly due to the fact that the images cover a large area on the ground at a single point in time.

Five types of correspondences are established between the various types of point clouds (section 3.2). A distinction can be made between correspondences in object space and image space. In object space three types of correspondences exist: (a) correspondences between overlapping lidar strips (STR-to-STR, section 3.2.5.1), (b) correspondences between control point clouds and lidar strips (CPC-to-STR, section 3.2.5.2), and (c) correspondences between image tie points and lidar strips (IMG-to-STR, section 3.2.5.3). A single correspondence in object space is given by two

points and their normal vectors, i.e. two corresponding planes. In the adjustment, the point-to-plane distance of all correspondences is minimized simultaneously, i.e. the distance between the two corresponding planes (section 3.2.4). It was shown that for lidar and image data this error metric is better suited than the often used point-to-point error metric; there are two reasons for this: (a) the point-to-plane error metric has a higher convergence rate and (b) generally no point-to-point correspondences exist due to the random ground sampling of the laser scanner. Special emphasis was placed on the selection of correspondences between lidar strips and image tie points, as the specific characteristics of both measurement techniques must be considered in this case. A rather simple, but in practice well working approach is to limit this type of correspondences to smooth and textured areas (e.g. roofs, streets, or facades) and weight each correspondence according to its plane's smoothness. However, this approach may not work in every situation, e.g. over forest. Thus, further investigations should be conducted on this subject. In image space two types of correspondences exist: (a) correspondences between homologous points and (b) correspondences between image points and ground control points (IMG-to-IMG, IMG-to-GCP, section 3.2.5.4). These correspondences are typically used in an aerial triangulation.

In the ICP algorithm *each* point is used as correspondence. This is simply not feasible for large flight campaigns with potentially hundreds of lidar strips and thousands of aerial images. Thus, four different strategies have been presented for the selection of correspondences in object space: (a) *Random Sampling*, (b) *Uniform Sampling*, (c) *Normal Space Sampling*, and (d) *Maximum Leverage Sampling*. The main differences among these strategies are their computational complexity and their suitability for different terrain types. The *Maximum Leverage Sampling* strategy is newly introduced in this thesis (section 3.2.1.1). It is based on theory of least squares adjustment and selects automatically correspondences in areas that are best suited for the estimation of transformation parameters. It was demonstrated that in situations rated as difficult on the subject of orientation (e.g. flat terrain with few geometric features), MLS shows a higher convergence rate, improves the determinability of parameters, and leads to smaller residuals.

It was already stated at the beginning of this thesis, that the separation of the lidar strip adjustment and the aerial triangulation is not considered as a problem per se. The main advantage of such a separation is that a rather complex problem is split into two smaller, easier manageable problems. One of the reasons for this separation is that in the past predominately either laser scanners *or* cameras have been used on airborne platforms. However, due to the miniaturization of the sensors and decreasing prices, a trend towards multi-sensor systems is observed. This applies not only to manned aerial platforms, but also to the fast increasing number of UAVs. Although these multi-sensor systems simultaneously record lidar and image data, their orientation is carried out independently. A wide range of proven commercial software exists to solve each of these two problems on its own, e.g. Riegl RiProcess, TerraSolid TerraMatch for lidar strip adjustments, and Agisoft Photoscan, Pix4D, Trimble Inpho Match-AT for aerial triangulations. However, large discrepancies between the lidar block and the image block can be the consequence of solving these two optimization problems independently. This is especially the case in challenging situations, e.g. corridor mapping with one lidar/image strip only, if no or very few ground truth data is available, if ground truth data is not well distributed, in case

of mapping of non-textured or dynamic areas, if the flight trajectory is temporarily very inaccurate (e.g. due to unfavorable satellite constellation or flight maneuvers) and many more. Such situations are characterized by a low block stability and low or no (e.g. in case of a single lidar strip) redundancy. Depending on the application, the resulting discrepancies between the lidar and image block may be acceptable. However, if this is not the case, these discrepancies can be inherently minimized by the hybrid adjustment presented in this thesis.

It should also be mentioned that there is still a lot of room for improvements. By combining the orientation of lidar and image data, not only the complexity increases, but also the data amounts. A commercial version[1] of the hybrid adjustment exists in the software package OPALS (Pfeifer et al., 2014). This software has been developed on the basis of lidar strips with a mean density of approximately 10 points/m^2 and with a maximum number of a few hundreds of aerial images. However, point densities, the number of images and their resolutions increased dramatically in recent time, especially if *UAV*s are used as sensor carriers. Therefore, one of the main challenges is to reduce the amount of data used in the adjustment without impairing the final orientation. This is especially challenging if time dependent trajectory errors should be modelled, as the estimation of the correction functions need a dense and uniform set of correspondences in time domain. Thus, a trade-off between accuracy, processing speed, and memory consumption must be found when choosing the computation parameters for the hybrid adjustment. Up to now, no automatic solution has been found to this problem. As a consequence, the processing time or the accuracy may become unacceptable for the user. Another related issue is the choice of the parameters to be estimated by adjustment. For this, a very comprehensive parameter model was presented in section 3.1. It offers an extensive set of weapons to fight any systematic errors. However, these extensive possibilities also increase the risk of overfitting by estimating unnecessary parameters. The main drawback thereby is that each parameter potentially weakens the overall block stability and may contribute to a global block deformation (e.g. bending). It was demonstrated that this problem can be strongly mitigated by (a) the joint orientation of lidar and image data and (b) by using fictional observations for some parameters. However, in some cases, these two measures can not completely avoid a block deformation, e.g. if the *Spline Trajectory Correction Model* with a very short segment length is used. Unfortunately, our experiments on using statistical tests like the Akaike Information Criterion (AIC) or Minimum Description Length (MDL) for the automatic selection of the parameter model were not conclusive. For the above reasons, the practical usage of the hybrid adjustment in its current form needs expertise in the field of photogrammetry/lidar and sufficient time (and patience) to gain experience with the manifold options that are offered.

Over the last few years, the method introduced in this thesis has been applied to the data of many flight missions. Its usefulness can be considered as practically proven. The adjusted lidar and image data made a contribution to many interesting applications, e.g. the quantification of geomorphic processes observed over a period of approximately 10 years (Hilger et al. (2019), Figures 4.7, 4.8, 4.9), the estimation of soil surface roughness (Milenković et al., 2015), the estimation of tree stem diameters (Wieser et al., 2017), the usage of lidar data to calibrate and correct data from satellite altimetry (Zlinszky et al., 2017), the modeling of complex terrain

[1] http://www.geo.tuwien.ac.at/opals/html/ModuleStripAdjust.html

and vegetation structures on the basis of high-resolution data captured from a UAV (Mandlburger et al., 2015a), and the fusion of point clouds from lidar and dense image matching (Mandlburger et al., 2017). However, the complexity of the hybrid adjustment opened also the door to a wide range of new investigations. Above all, a more detailed analysis of the differences between the camera's and laser's view on the Earth's surface would be of interest. Other investigations could cover such aspects as the automatic choice of computation parameters, the scalability of the problem, the refinement of the measurement process, the application on mobile data, and the improvement of the efficiency of the method. It is hoped that the hybrid adjustment presented in this thesis provides a solid basis for such studies.

Acknowledgments

This research was partly funded by the project:

PROSA (High-resolution measurements of morphodynamics in rapidly changing PROglacial Systems of the Alps) which is a joined project of the German research community (DFG, project number BE 1118/27-1) and the Austrian science foundation (FWF, project number I893).

The UAV LiDAR and image data of Hessigheim (section 4.4) were used with kind permission of the Federal Institute of Hydrology (BfG), Koblenz, Germany.

Acronyms

AIC Akaike Information Criterion

ALS Airborne Laser Scanning

CPC Control Point Cloud

DEM Digital Elevation Model

DIM Dense Image Matching

DSM Digital Surface Model

DTM Digital Terrain Model

ECEF Earth-Centered, Earth-Fixed

GCP Ground Control Point

GNSS Global Navigation Satellite System

ICP Iterative Closest Point

INS Inertial Navigation System

LSA Least Squares Adjustment

LSM Least Squares Matching

MDL Minimum Description Length

RANSAC Random Sample Consensus

TIN Triangular Irregular Network

TLS Terrestrial Laser Scanning

UAV Unmanned Aerial Vehicle

UTM Universal Transverse Mercator

Bibliography

Abayowa, B.O., Yilmaz, A., Hardie, R.C., 2015. Automatic registration of optical aerial imagery to a lidar point cloud for generation of city models. ISPRS Journal of Photogrammetry and Remote Sensing 106, 68–81.

Baltsavias, E.P., 1999. A comparison between photogrammetry and laser scanning. ISPRS Journal of photogrammetry and Remote Sensing 54, 83–94.

Bäumker, M., Heimes, F., 2001. New calibration and computing method for direct georeferencing of image and scanner data using the position and angular data of an hybrid inertial navigation system, in: OEEPE Workshop, "Integrated Sensor Orientation", Hannover, Germany.

Beger, R., Gedrange, C., Hecht, R., Neubert, M., 2011. Data fusion of extremely high resolution aerial imagery and lidar data for automated railroad centre line reconstruction. ISPRS Journal of Photogrammetry and Remote Sensing 66, S40–S51.

Belsley, D.A., Kuh, E., Welsch, R.E., 2005. Regression diagnostics: Identifying influential data and sources of collinearity. volume 571. John Wiley & Sons.

Besl, P.J., McKay, N.D., 1992. Method for registration of 3-d shapes, in: Robotics-DL tentative, International Society for Optics and Photonics. pp. 586–606.

Blais, G., Levine, M.D., 1995. Registering multiview range data to create 3d computer objects. IEEE Transactions on Pattern Analysis and Machine Intelligence 17, 820–824.

Blázquez, M., Colomina, I., 2010. On the role of self-calibration functions in integrated sensor orientation, in: Proc. of the International Calibration and Orientation Workshop (EuroCOW).

Bork, E.W., Su, J.G., 2007. Integrating lidar data and multispectral imagery for enhanced classification of rangeland vegetation: A meta analysis. Remote Sensing of Environment 111, 11–24.

Brenner, C., 2005. Building reconstruction from images and laser scanning. International Journal of Applied Earth Observation and Geoinformation 6, 187–198.

Briese, C., Glira, P., Pfeifer, N., 2013. Integration of multi-temporal airborne and terrestrial laser scanning data for the analysis and modelling of proglacial geomorphodynamic processes, in: EGU General Assembly Conference Abstracts.

Brown, D.C., 1971. Close-range camera calibration. Photogrammetric Engineering 37, 855–866.

Burnham, K.P., Anderson, D.R., 2002. Model selection and multimodel inference: a practical information-theoretic approach. Springer Science & Business Media.

Chatterjee, S., Hadi, A.S., 1986. Influential observations, high leverage points, and outliers in linear regression. Statistical Science , 379–393.

Chen, Y., Medioni, G., 1992. Object modelling by registration of multiple range images. Image and Vision Computing 10, 145 – 155. URL: http://www.sciencedirect.com/science/article/pii/026288569290066C, doi:http://dx.doi.org/10.1016/0262-8856(92)90066-C. range Image Understanding.

Colomina, I., 2015. On trajectory determination for photogrammetry and remote sensing: Sensors, models and exploitation, in: Fritsch, D. (Ed.), Proceedings Photogrammetric Week 2015, Stuttgart, Germany. pp. 131–142.

Cramer, M., Haala, N., Laupheimer, D., Mandlburger, G., Havel, P., 2018. Ultra-high precision uav-based lidar and dense image matching. ISPRS - International Archives of the Photogrammetry, Remote Sensing and Spatial Information Sciences XLII-1, 115–120. URL: https://www.int-arch-photogramm-remote-sens-spatial-inf-sci.net/XLII-1/115/2018/, doi:10.5194/isprs-archives-XLII-1-115-2018.

Cucci, D.A., Rehak, M., Skaloud, J., 2017. Bundle adjustment with raw inertial observations in uav applications. ISPRS Journal of Photogrammetry and Remote Sensing 130, 1–12.

Ebner, H., 1976. Self calibrating block adjustment. Bildmessung und Luftbildwessen 44, 128–139.

Förstner, W., Wrobel, B., 2016. Photogrammetric Computer Vision – Statistics, Geometry, Orientation and Reconstruction. Springer. doi:10.1007/978-3-319-11550-4.

Friess, P., 2006. Toward a rigorous methodology for airborne laser mapping, in: Proceedings EuroCOW, Castelldefels, Spain. pp. 25–27.

Glennie, C., 2007. Rigorous 3d error analysis of kinematic scanning lidar systems. Journal of Applied Geodesy 1, 147–157.

Glira, P., Briese, C., Kamp, N., Pfeifer, N., 2013. Simultaneous relative and absolute orientation of point clouds with TLS radomes, in: EGU General Assembly Conference Abstracts, p. 13116.

Glira, P., Briese, C., Pfeifer, N., Dusik, J., Hilger, L., Neugirg, F., Baewert, H., 2014. Accuracy analysis of height difference models derived from terrestrial laser scanning point clouds, in: EGU General Assembly Conference Abstracts.

Glira, P., Pfeifer, N., Briese, C., Ressl, C., 2015a. A correspondence framework for ALS strip adjustments based on variants of the ICP algorithm. PFG Photogrammetrie, Fernerkundung, Geoinformation 2015, 275–289. URL: http://dx.doi.org/10.1127/pfg/2015/0270.

Glira, P., Pfeifer, N., Briese, C., Ressl, C., 2015b. Rigorous strip adjustment of airborne laserscanning data based on the ICP algorithm. ISPRS Annals of Photogrammetry, Remote Sensing and Spatial Information Sciences II-3/W5, 73–80. URL: http://www.isprs-ann-photogramm-remote-sens-spatial-inf-sci.net/II-3-W5/73/2015/, doi:10.5194/isprsannals-II-3-W5-73-2015.

Glira, P., Pfeifer, N., Mandlburger, G., 2016. Rigorous strip adjustment of UAV-based laserscanning data including time-dependent correction of trajectory errors. Photogrammetric Engineering & Remote Sensing 82, 945–954.

Grün, A., 1986. Photogrammetrische punktbestimmung nach der bündelmethode. Institut für Geodäsie und Photogrammetrie, ETH Zürich, Mitteilungen .

Habib, A., 2018. Integration of lidar and photogrammetric data: Triangulation and orthorectification, in: Shan, J., Toth, C.K. (Eds.), Topographic Laser Ranging and Scanning-Principles and Processing (Ed.: Shan, J., Toth, C. K. / CRC Press). CRC Press, pp. 413–441.

Habib, A., Bang, K.I., Kersting, A.P., Chow, J., 2010. Alternative methodologies for lidar system calibration. Remote Sensing 2, 874–907.

Habib, A., Rens, J., 2007. Quality assurance and quality control of lidar systems and derived data, in: Advanced Lidar Workshop, University of Northern Iowa, United States; 7–8 Aug. 2007.

Hampel, F.R., 1974. The influence curve and its role in robust estimation. Journal of the American Statistical Association 69, 383–393.

Hebel, M., Stilla, U., 2012. Simultaneous calibration of ALS systems and alignment of multiview LiDAR scans of urban areas. Geoscience and Remote Sensing, IEEE Transactions on 50, 2364–2379.

Hilger, L., Dusik, J., Heckmann, T., Haas, F., Glira, P., Pfeifer, N., Vehling, L., Rohn, J., Morche, D., Baewert, H., et al., 2019. A Sediment Budget of the Upper Kaunertal. Springer Nature Switzerland. pp. 289–312.

Hirschmuller, H., 2008. Stereo processing by semiglobal matching and mutual information. IEEE Transactions on Pattern Analysis and Machine Intelligence 30, 328–341. doi:10.1109/TPAMI.2007.1166.

Hoaglin, D.C., Welsch, R.E., 1978. The hat matrix in regression and anova. The American Statistician 32, 17–22.

Horn, B.K., 1987. Closed-form solution of absolute orientation using unit quaternions. JOSA A 4, 629–642.

Kager, H., 2004. Discrepancies between overlapping laser scanner strips–simultaneous fitting of aerial laser scanner strips. International Archives of Photogrammetry, Remote Sensing and Spatial Information Sciences 35, 555–560.

Kalman, R.E., 1960. A new approach to linear filtering and prediction problems. Journal of Fluids Engineering 82, 35–45.

Katzenbeisser, R., 2003. About the calibration of lidar sensors, in: ISPRS Workshop "3-D Reconstruction form Airborne Laser-Scanner and InSAR data"; 8—10 Oct. 2003, Dresden, Germany.

Kersting, A.P., Habib, A.F., Bang, K.I., Skaloud, J., 2012. Automated approach for rigorous light detection and ranging system calibration without preprocessing and strict terrain coverage requirements. Optical Engineering 51, 076201–1.

Kraus, K., 1997. Photogrammetry, Vol.2, Advanced Methods and Applications. Duemmler / Bonn.

Kraus, K., Ressl, C., Roncat, A., 2006. Least squares matching for airborne laser scanner data, in: Fifth International Symposium Turkish-German Joint Geodetic Days "Geodesy and Geoinformation in the Service of our Daily Life".

Mandlburger, G., Glira, P., Pfeifer, N., 2015a. UAS-borne lidar for mapping complex terrain and vegetation structure. GIM International - the Worldwide Magazine For Geomatics 29, 30–33.

Mandlburger, G., Hollaus, M., Glira, P., Wieser, M., Milenkovic, M., Riegl, U., Pfennigbauer, M., 2015b. First examples from the RIEGL VUX-SYS for forestry applications, in: Proc. SilviLaser 2015; 28–30 Sep. 2015, La Grande Motte, France.

Mandlburger, G., Pfennigbauer, M., Riegl, U., Haring, A., Wieser, M., Glira, P., Winiwarter, L., 2015c. Complementing airborne laser bathymetry with UAV-based lidar for capturing alluvial landscapes, in: Remote Sensing for Agriculture, Ecosystems, and Hydrology XVII, International Society for Optics and Photonics. p. 96370A.

Mandlburger, G., Wenzel, K., Spitzer, A., Haala, N., Glira, P., Pfeifer, N., 2017. Improved topographic models via concurrent airborne lidar and dense image matching. ISPRS Annals of Photogrammetry, Remote Sensing & Spatial Information Sciences 4.

Mikolajczyk, K., Schmid, C., 2005. A performance evaluation of local descriptors. IEEE transactions on pattern analysis and machine intelligence 27, 1615–1630.

Milenković, M., Pfeifer, N., Glira, P., 2015. Applying terrestrial laser scanning for soil surface roughness assessment. Remote Sensing 7, 2007–2045.

Parmehr, E.G., Fraser, C.S., Zhang, C., Leach, J., 2014. Automatic registration of optical imagery with 3d lidar data using statistical similarity. ISPRS Journal of Photogrammetry and Remote Sensing 88, 28–40.

Pfeifer, N., Mandlburger, G., Glira, P., 2016. Laserscanning. Springer Berlin Heidelberg, Berlin, Heidelberg. pp. 1–51. URL: https://doi.org/10.1007/978-3-662-46900-2_44-1, doi:10.1007/978-3-662-46900-2_44-1.

Pfeifer, N., Mandlburger, G., Glira, P., Roncat, A., Mücke, W., Zlinszky, A., 2015. Lidar: Exploiting the versatility of a measurement principle in photogrammetry. 55th photogrammetric week , 105–118.

Pfeifer, N., Mandlburger, G., Otepka, J., Karel, W., 2014. OPALS – A framework for airborne laser scanning data analysis. Computers, Environment and Urban Systems 45, 125 – 136. URL: http://www.sciencedirect.com/science/article/pii/S0198971513001051, doi:http://dx.doi.org/10.1016/j.compenvurbsys.2013.11.002.

Planitz, B.M., Maeder, A.J., Williams, J., 2005. The correspondence framework for 3d surface matching algorithms. Computer Vision and Image Understanding 97, 347–383.

Remondino, F., Spera, M.G., Nocerino, E., Menna, F., Nex, F., 2014. State of the art in high density image matching. The Photogrammetric Record 29, 144–166.

Ressl, C., Brockmann, H., Mandlburger, G., Pfeifer, N., 2016. Dense image matching vs. airborne laser scanning – comparison of two methods for deriving terrain models. Photogrammetrie-Fernerkundung-Geoinformation 2016, 57–73.

Ressl, C., Kager, H., Mandlburger, G., 2008. Quality checking of als projects using statistics of strip differences, in: Proceedings, Vol. XXXVII. Part B3b. pp. 253–260. URL: http://publik.tuwien.ac.at/files/PubDat_165656.pdf. poster presentation: International Society for Photogrammetry and Remote Sensing XXIst Congress, Beijing, China; 2008-07-03 – 2008-07-11.

Rothermel, M., Wenzel, K., Fritsch, D., Haala, N., 2012. Sure: Photogrammetric surface reconstruction from imagery, in: Proceedings LC3D Workshop, Berlin.

Rusinkiewicz, S., Levoy, M., 2001. Efficient variants of the ICP algorithm, in: 3-D Digital Imaging and Modeling, 2001. Proceedings. Third International Conference on, IEEE, Quebec City, Canada. pp. 145–152.

Shakarji, C.M., 1998. Least-squares fitting algorithms of the nist algorithm testing system. Journal of research of the National Institute of Standards and Technology 103, 633.

Sharp, G.C., Lee, S.W., Wehe, D.K., 2002. Icp registration using invariant features. IEEE Transactions on Pattern Analysis and Machine Intelligence 24, 90–102.

Skaloud, J., Lichti, D., 2006. Rigorous approach to bore-sight self-calibration in airborne laser scanning. ISPRS Journal of Photogrammetry and Remote Sensing 61, 47–59.

Skaloud, J., Schaer, P., Stebler, Y., Tomé, P., 2010. Real-time registration of airborne laser data with sub-decimeter accuracy. ISPRS Journal of Photogrammetry and Remote Sensing 65, 208–217.

Toth, C.K., 2002. Calibrating airborne lidar systems, in: ISPRS Commission II, Symposium 2002, Xian, China, ISPRS Archives of Photogrammetry, Remote Sensing and Spatial Information Sciences. pp. 475–480.

Toth, C.K., 2009. Strip adjustment and registration, in: Shan, J., Toth, C.K. (Eds.), Topographic Laser Ranging and Scanning-Principles and Processing (Ed.: Shan, J., Toth, C. K. / CRC Press). CRC Press, pp. 235–268.

Toth, C.K., Koppanyi, Z., 2018. Strip adjustment and registration, in: Shan, J., Toth, C.K. (Eds.), Topographic Laser Ranging and Scanning-Principles and Processing (Ed.: Shan, J., Toth, C. K. / CRC Press). CRC Press, pp. 259–290.

Vehling, L., Baewert, H., Glira, P., Moser, M., Rohn, J., Morche, D., 2017. Quantification of sediment transport by rockfall and rockslide processes on a proglacial rock slope (Kaunertal, Austria). Geomorphology 287, 46–57.

Wieser, M., Hollaus, M., Mandlburger, G., Glira, P., Pfeifer, N., 2016. ULS lidar supported analyses of laser beam penetration from different ALS systems into vegetation. ISPRS Annals of Photogrammetry, Remote Sensing & Spatial Information Sciences 3.

Wieser, M., Mandlburger, G., Hollaus, M., Otepka, J., Glira, P., Pfeifer, N., 2017. A case study of UAS-borne laser scanning for measurement of tree stem diameter. Remote Sensing 9, 1154.

Yang, B., Chen, C., 2015. Automatic registration of uav-borne sequent images and lidar data. ISPRS Journal of Photogrammetry and Remote Sensing 101, 262–274.

Zhang, Y., Shen, X., 2013. Direct georeferencing of airborne lidar data in national coordinates. ISPRS journal of photogrammetry and remote sensing 84, 43–51.

Zlinszky, A., Boergens, E., Glira, P., Pfeifer, N., 2017. Airborne laser scanning for calibration and validation of inshore satellite altimetry: A proof of concept. Remote Sensing of Environment 197, 35–42.

Zlinszky, A., Glira, P., Boergens, E., Pfeifer, N., 2015. Comparing airborne lidar water surface heights with synchronous envisat altimetry over lake Balaton, Hungary, in: EGU General Assembly Conference Abstracts.